IS-1730

Physics (UC-34)
TID-4500, March 1, 1967

UNITED STATES ATOMIC ENERGY COMMISSION

Research and Development Report

MEASUREMENTS OF SOME GAMMA-RAY RELATIVE INTENSITIES AND INTERNAL CONVERSION COEFFICIENTS USING A BENT-CRYSTAL MONOCHROMATOR

by

Gerald C. Nelson and E. N. Hatch

November 1967

Ames Laboratory

at

Iowa State University of Science and Technology
F. H. Spedding, Director

Contract W-7405 eng-82

DISCLAIMER

IS-1730

This report is distributed according to the category Physics (UC-34) as listed in TID-4500, March 1, 1967.

Printed in the United States of America
Available from
Clearinghouse for Federal Scientific and Technical Information
National Bureau of Standards, U. S. Department of Commerce
Springfield, Virginia 22151
Price: Printed Copy $3.00; Microfiche $0.65

TABLE OF CONTENTS

IS-1730

MEASUREMENTS OF SOME GAMMA-RAY RELATIVE INTENSITIES AND INTERNAL CONVERSION COEFFICIENTS USING A BENT-CRYSTAL MONOCHROMATOR*

Gerald C. Nelson and E. N. Hatch

ABSTRACT

The X-ray and gamma-ray relative intensities were measured from the decay of Tm^{170}, Ho^{166}, Hf^{180m}, Eu^{155} and Sm^{155} with a bent-crystal monochromator and a linear least-squares computer program. The K-shell internal conversion coefficients were determined for the E2 transitions in Yb^{170} and Er^{166}. The K-shell conversion coefficient, α_K, for the 84.3-keV transition in Yb^{170} was determined to be 1.43±0.04 while the K-shell internal conversion coefficient for the 80.6-keV transition in Er^{166} was determined to be 1.72±0.06. The results for these $2^+ \rightarrow 0^+$ transitions are five percent higher than the theoretical values for these transitions. From the relative intensities of the transitions in Hf^{180} it was possible to deduce a value for the total internal conversion coefficient for the 93.3-keV transition of $\alpha_T^{93} = 4.91 \pm 0.23$. Using the previous measurements of conversion electron intensities of Edwards and Boehm and the present measured gamma-ray relative intensities, internal conversion coefficients for all the other transitions were obtained. The present

*This report is based on a Ph.D. Thesis submitted by Gerald C. Nelson, November, 1967 to Iowa State University, Ames, Iowa.

measurements of α_K for the 215.3-, 332.5- and 443.8- keV E2 transitions are 11 percent lower than the theoretical values, while α_K for the 93.3-keV E2 transition agrees closely with the theoretical value. These results are in close agreement with the previous measurements of Edwards and Boehm. The present value for α_K for the 501-keV transition agrees closely with the theoretical α_K for an E3 multipolarity. From the X-ray and gamma-ray relative intensities of the transitions in Gd^{155} and the previous measurement of the ratio of K conversion electrons for the 86- and 105-keV transitions of Subba Rao, it was possible to determine the K conversion coefficients for the 86- and 105-keV transitions of $\alpha_K = 0.43 \pm 0.06$ and $\alpha_K = 0.23 \pm 0.03$. These results are in agreement with the theoretical values for pure E1 transitions. The relative intensities of the 246-, 142- and 104-keV gamma rays following the decay of 22 minute Sm^{155} were determined with improved precision in order that they might be used to determine accurately the conversion coefficients for these transitions.

I. INTRODUCTION

A. Definition of the Internal Conversion Process

Below 1-MeV the principal processes by which an excited nucleus can make a transition to a lower energy level are gamma-ray emission and internal conversion. In the first process the nucleus emits a gamma ray with energy equal to the transition energy,

$$N^* \rightarrow N + \gamma$$

where N* is the nucleus in the excited state, N is the nucleus in the lower energy state and γ is the emitted gamma ray which has an energy equal to the transition energy. In internal conversion the nuclear transition energy is transferred to one of the orbital electrons by a direct interaction between the electron and the charged nucleons. The electron is then ejected from the atom with an energy equal to the nuclear transition energy minus the binding energy of the electron.

$$N^* + Ze \rightarrow N + (Z-1)e + e_{\text{continuum}}$$

$$E_e = E_{N^*-N} - E_{\text{binding}}$$

where N* +Ze is the excited nucleus with Z electrons, N + (Z-1)e is the nucleus in the lower energy state with Z-1 electrons, $e_{\text{continuum}}$ is the ejected electron in the continuum, E_e is the energy of the ejected electron, E_{N^*-N} is the transition energy and E_{binding} is the binding energy of the ejected electron.

Following the ejection of an internal conversion electron, the atomic electrons will readjust, and an outer electron will fill the vacancy. The energy difference is carried off by one of two processes. The first and predominant process is the emission of an X-ray which will have an energy equal to the difference between the binding energy of the shell in which the vacancy occurred and the binding energy of the shell from which the outer electron came. The other process by which energy is carried off following internal conversion is the emission of a second electron called an Auger electron. The resulting atom is ionized in two shells. The energy of the emitted electron is approximately given by

$$E\,(KXY) = E\,(K) - E\,(X) - E^{X}\,(Y) = E\,(K) - E^{Y}\,(X) - E\,(Y),$$

where K, X, and Y are respectively the shell from which the internal conversion electron is ejected, the shell from which the K shell is filled, and the shell from which the Auger electron is emitted. $E^{X}\,(Y)$ is the electron binding energy of the Y shell in an atom with charge Z ionized in the X shell.

For a given transition the internal conversion coefficient, α, is defined as the ratio of N_e, the number of internal conversion electrons emitted per unit time, to N_γ, the number of gamma rays emitted per unit time,

$$\alpha = \frac{N_e}{N_\gamma} \quad .$$

The internal conversion coefficient for a particular shell or subshell is defined similarly. For the K shell

$$\alpha_K = \frac{N_e^K}{N_\gamma} \quad ,$$

where N_e^K is the number of internal conversion electrons emitted from the K shell per unit time. The total internal conversion coefficient is the sum of the internal conversion coefficients of the individual shells.

$$\alpha_T = \alpha_K + \alpha_L + \alpha_M + \ldots$$

B. Remarks About Internal Conversion Coefficients

The internal conversion coefficients depend strongly on five parameters; the shell in which the conversion occurs, the transition energy, the atomic number, the angular momentum change and the parity change between the initial and final nuclear states. Internal conversion coefficients always increase as the transition energy decreases. They normally increase with Z, and always increase as the angular momentum, L, increases. To a large extent, internal conversion coefficients are independent of detailed nuclear structure. This makes it possible to obtain information about the spin and parity of the nuclear transition by comparing the experimentally determined conversion coefficients with those theoretically predicted.

When the nuclear angular momenta for initial and final states are J_i and J_f, the emitted gamma ray can have any angular momentum L for which

$$\Delta J = |J_i - J_f| \leq L \leq J_i + J_f \ .$$

The electromagnetic transitions are classified as electric 2^L, EL, or magnetic 2^L, ML, if the parity change between the initial and final nuclear states is $(-1)^L$ or $(-1)^{L+1}$, respectively.

The internal conversion coefficient is in general a mixture of

conversion coefficients of pure angular momentum L

$$\alpha = \sum_L a_L \alpha_L \quad ,$$

where $\sum_L a_L = 1.$

The a_L represent the fraction of total gamma rays emitted with angular momentum L. For a given type of multipole, the relative intensity for multipoles with L and L+2 is given by (1)

$$\frac{a_{L+2}}{a_L} \approx \left(\frac{R}{\lambda} \right)^4 << 1,$$

where R is the nuclear radius and λ is the wavelength of the radiation. For A = 200 and E_γ = 511-keV, one gets $a_{L+2} / a_L = 3.2 \times 10^{-9}$. Therefore, the mixture can be restricted to two multipoles. Assuming parity conservation in electromagnetic transitions, and from the parity selection rules, if the parity changes in the transition, only electric multipoles of odd order or magnetic multipoles of even order can occur. If the parity remains the same, only electric multipoles of even order or magnetic multipoles of odd order can occur. For example, if $J_i = 1$ and $J_f = 2$, and the parity does not change

$$\alpha_K = a_1 \alpha_K(M1) + a_2 \alpha_K(E2),$$

and

$$a_1 + a_2 = 1 \ .$$

Similarly,

$$\alpha_L = a_1\alpha_L(M1)+a_2\alpha_L(E2) ,$$

where L now denotes the L shell. These two equations can then be solved for the mixing ratio

$$\delta^2 = \frac{a_2}{a_1} = -\frac{\alpha_K(M1) - \alpha_K/\alpha_L\ \alpha_L(M1)}{\alpha_K(E2) - \alpha_K/\alpha_L\ \alpha_L(E2)} ,$$

where α_K/α_L is the measured value, and $\alpha_K(M1)$, $\alpha_L(M1)$, $\alpha_K(E2)$ and $\alpha_L(E2)$ are theoretical values. If either J_i or $J_f = 0$, then $L = \Delta J$, and the transition consists of only one multipole. Therefore, direct comparison can be made in this case between the experimental conversion coefficient and the theoretical conversion coefficient.

Rose (1) and Sliv and Band (2) have tabulated internal conversion coefficients as a function of atomic number and transition energy. These tables have been calculated taking into account screening effects and finite nuclear size. A uniform charge distribution is used inside the nuclear volume and a Thomas-Fermi-Dirac potential is used outside the nuclear volume.

By allowing the nucleus to have a finite nuclear size, the electron wavefunction is modified since the electron moves in the field of an extended charge distribution. This is the so-called static effect because it depends only on the nuclear density. Also, the electron spends a fraction of its time inside the nucleus where it probes the details of the nuclear charges and currents. This is the dynamic effect. If this penetration term is ignored, the conversion coefficient depends only on the electron wavefunction. Rose (1) has calculated conversion coefficients for the K, L_I,

and L_{II} shells including screening and static effects. His L_{III} conversion coefficients include only screening, and his M coefficients are calculated for a point nucleus without screening. Sliv and Band (2) have calculated conversion coefficients for the K and L shells including screening, static effects, and dynamic effects. For the dynamic effects, they assume a uniform surface current density.

The dynamic effect is usually small since the electron spends so little time inside the nucleus. However, Church and Weneser (3) have pointed out that there are transitions for which the gamma-ray matrix element is greatly inhibited, while the nuclear penetration matrix element may have its uninhibited value. In cases where the penetration terms are not important, the errors in the tabulated values are about three percent (1).

Conversion coefficients in isotopes in the highly deformed regions are of particular interest for showing nuclear structure effects. These regions are A = 23, $150 \leq A \leq 190$ and $A > 230$. In these regions the transitions may be highly retarded over single particle estimates, and conversion coefficients for these hindered transitions may deviate considerably from those predicted by theories which do not take into account the detailed nuclear structure.

C. Experimental Methods of Measuring Internal Conversion Coefficients

Subba Rao (4) has recently written an extensive review article on the methods for measuring internal conversion coefficients. All of these methods have areas where they are applicable. It is often necessary to pick the method most suitable for the particular internal conversion coefficients under investigation. Only those methods most widely used for high precision

will be mentioned here.

In the internal-external conversion method a beta-ray spectrometer is used to determine the internal conversion electron relative intensities. The gamma-ray relative intensities from the same source are then determined by the external conversion method, which will be described in Section D of the Introduction. The internal conversion coefficients can then be determined from the ratios of the electron intensities to the gamma-ray intensities. Internal conversion coefficients have been measured to five percent with this method (5, 6).

It is possible, in cases where there is only one gamma-ray transition, to determine the K internal conversion coefficient by measuring the ratio of N_X^K, the number of K X-rays emitted following internal conversion to the N_γ number of gamma rays. The K internal conversion coefficient α_K, can then be calculated from

$$\alpha_K = \frac{N_X^K}{\omega_K N_\gamma}, \qquad \text{Equation 1}$$

where ω_K is the probability that a vacancy in the K shell is filled under emission of K X-rays, and it is called the fluorescent yield of the K shell. The values of ω_K have been determined by fitting the observed data to a semi-empirical formula. These values have been tabulated by Wapstra et al. (7).

In some cases it is more convenient to measure the total transition rate, $N_\gamma+N_e$, by observing the rate of emission of particles which uniquely feed the transition. This can be done by gating the spectrum from the transition of interest by another particle which is in coincidence with that

transition. Then, along with either N_γ or N_e, the total conversion coefficient can be determined.

Relative internal conversion coefficients can be determined from the ratios of relative internal conversion electron intensities and relative gamma-ray intensities. If a normalization constant can be determined, absolute conversion coefficients can be calculated. The internal conversion electron relative intensities can be measured to a few percent with magnetic beta-ray spectrometers. Gamma-ray relative intensities are often known to no better than five or ten percent. Thus, to determine accurately internal conversion coefficients with this method, the gamma-ray relative intensities must be measured to five percent or less.

The present investigation is concerned with the accurate measurement of gamma-ray and X-ray relative intensities and the application of these accurately determined intensities to the determination of internal conversion coefficients.

D. Some Experimental Methods of Measuring Gamma-ray Relative Intensities

Three methods have recently been used to obtain gamma-ray relative intensities with high accuracy. They are photoelectric conversion, crystal diffraction, and least-squares analysis of scintillation spectra.

Hultberg (8) has described in detail the photoelectric conversion method. In this method gamma rays, whose intensities are to be measured, pass into a converter, a substance with a high atomic number, which is mounted in the source position of a magnetic beta-ray spectrometer. The gamma rays eject K, L, and M electrons from the atoms in the converter. The energy of the electrons is given by

$$E_e = E_\gamma - E_{binding}. \qquad \text{Equation 2}$$

If the resolution is good and the converter not too thick, the shape of the distribution of photoelectrons yielded from the K shell will approximate the shape of the transmission curve of the spectrometer. The procedure is to take a series of counts at a sufficient number of settings of the magnetic field to determine the profile of the line. If the number of counts received per unit time at the field B is N, and since the momentum interval accepted by a magnetic spectrometer is proportional to Bρ, it follows that

$$N\ (B\rho)\ d\ (B\rho) = (N/B\rho)\ d\ (B\rho),$$

where n (B) is the number of counts per momentum interval. A plot of N/B vs. Bρ is made. The area under the line is

$$\int_{\text{line}} (N/B\rho)\ d\ (B\rho) = \text{const}\ \tau_K\ (E_\gamma)\ f\ (E_\gamma) = A\ ,$$

where τ_K (E) is the photoelectric cross section from the K shell and f (E_γ) is the fraction of all K photoelectrons at energy E detected by the spectrometer. The f (E_γ) depends on the particular source and the converter geometry and is very difficult to determine.

For this method, intense thin sources are needed. This method takes advantage of the high resolution of the beta-ray spectrometer. Using this method, gamma-ray relative intensities can be measured to about five percent.

The crystal diffraction method has been used by Lind et al. (9), Hatch (10), Bergvall (11), and Edwards and Boehm (12). In this method, a bent-crystal spectrometer is set at a diffraction maximum for a particular gamma ray. The intensity of the gamma ray is then proportional to the

counting rate (13). Corrections must be made for absorption of the gamma rays in the air path between the source and detector, for the absorption of the cover of the detector, the half life of the source, the efficiency of the detector, the absorption of the gamma rays in the source itself, the absorption in the source container, the absorption in the diffraction crystal, and the energy dependence of the reflectivity of the diffraction crystal. The density of the source material is sometimes not known well and can contribute a large error. Also, unless an extensive study is made of the reflectivity of the diffraction crystal, a rather large error could be introduced by assuming an analytical expression for the energy dependence of the crystal reflectivity.

Edwards (13) has carried out an extensive study of the reflectivity of the diffraction from the (310) planes of a 2mm thick quartz crystal and has measured gamma-ray relative intensities with an uncertainty of less than five percent. For very weak gamma rays this method is often the only one available for intensity measurements. Because of the solid angle and the poor efficiency of the diffraction crystal, source strengths from 0.1 curies to several curies are needed. This method takes advantage of the high resolution of the bent-crystal spectrometer.

The least-squares scintillation method has been applied extensively to activation analysis as well as gamma-ray relative intensity measurements. This method has been developed by Reynolds (14), Trombka (15, 16), Heath (17), Ferguson (18), Salmon (19), Parr and Lucas (20) and McWilliams (21). A detailed discussion will be given of the linear least-squares method since it is basically this approach which was used in the present investigation.

The procedure used in this method is to expose a NaI(Tl) crystal to the source under investigation. The resulting light pulses are converted to electrical pulses in a photomultiplier and these electrical pulses are amplified and fed into a multichannel analyzer to obtain a counts vs. pulse-height spectrum. From a library of response functions for monoenergetic gamma rays, an interpolation is made to determine the response of the NaI (Tl) crystal for the particular energies contained in the source under investigation. A computer program is then applied to determine the gamma-ray relative intensities.

The linear least-squares method for determining gamma-ray relative intensities assumes that the complex gamma-ray pulse-height spectrum is a linear combination of response functions due to the presence of gamma rays of various energies.

The response functions depend on the various ways that gamma rays interact with the detector material. Below 1-MeV there are two ways in which gamma rays interact with matter. They are photoelectric absorption and Compton scattering. Photoelectric absorption is most important at low energies (below 500-keV) and Compton scattering is most important at higher energies (above 500-keV). Photoelectric absorption occurs when a gamma ray transfers all of its energy to an electron by ejecting the electron from a K, L, or M shell. The energy of the electron is given by Equation 2. After the electron is ejected from the atom, an outer shell electron will fill the vacancy causing emission of an X-ray or Auger electron as described in Section A of the Introduction.

Compton scattering is the process in which a photon interacts with an essentially free electron by transferring part of its energy to the electron

and scattering in such a way as to conserve energy and momentum. The energy, E_γ', of the scattered gamma ray will be

$$E_{\gamma'} = \frac{E_\gamma}{1 + \frac{E_\gamma}{Mc^2}(1 - \cos\Theta)} ,$$

where Θ is the angle of the scattered gamma ray makes with the original direction of the gamma-ray photon and E_γ is the energy of the incoming gamma ray.

In NaI(Tl), the electrons which have gained energy by photoelectric absorption or Compton scattering give rise to light pulses. The decay time of the light pulse in the crystal is longer than the interaction time of the gamma ray. Therefore, a gamma ray may be scattered several times and photoelectrically absorbed before the light pulse decays. To a first order approximation, the intensity of the light is proportional to the energy which the gamma ray loses in the crystal. A response function of a NaI(Tl) detector to a monoenergetic gamma ray of 444-keV is shown in Figure 1. It consists of a photopeak and the Compton continuum. The photopeak corresponds to the full energy of the incoming gamma ray regardless of the manner in which it transfers energy to the electrons. The maximum energy for the Compton scattering occurs when the gamma ray scatters through 180 degrees, and it is given by

$$E_C = E_\gamma - \frac{E_\gamma}{1 + \frac{2E_\gamma}{Mc^2}} ,$$

where E_C is the maximum energy for Compton scattering, E_γ is the energy of

the incoming gamma ray and Mc^2 is the rest mass of the electron.

Another feature which becomes evident below 100-keV is the iodine escape peak. Figure 2 shows a photopeak and an iodine escape peak for a 57-keV gamma ray. The escape peak is due to iodine X-rays escaping undetected from the NaI(Tl) crystal following photoelectric absorption.

The number of counts in the photopeak of each monoenergetic response function is related to the intensity of the gamma ray by

$$N_i = I_i \, t \, \frac{\omega}{4\pi} \, e^{-\mu_i d_i} \varepsilon_i P_i \quad (22),$$

where N_i is the number of counts in the photopeak of gamma ray i with energy E_i, I_i is the number of gamma rays of energy E_i emitted per unit time, t is the time the detector is exposed to the radioactive source, ω is the solid angle subtended by the crystal, $e^{-\mu_i d_i}$ is the fraction of gamma rays not absorbed before reaching the crystal, ε_i is the efficiency of the crystal, and P_i is the ratio of the number of counts in the photopeak to the total number of counts in the response function. Thus,

$$\frac{I_i}{I_j} = \frac{N_i}{N_j} \, \frac{e^{-\mu_j d_j} \, \varepsilon_j P_j}{e^{-\mu_i d_i} \, \varepsilon_i P_i} \quad . \qquad \text{Equation 3}$$

The efficiency as a function of energy has been tabulated (23) for certain geometries or it can be calculated. The absorption coefficients, μ, for the various materials between the source and detector are also tabulated (24, 25). The photopeak to total ratios must be experimentally determined in a scatter free geometry for the given source to crystal distance. The photopeak area is used in the method of Trombka (15, 16) to determine the gamma-ray intensity because it is least affected by scattering. The problem has

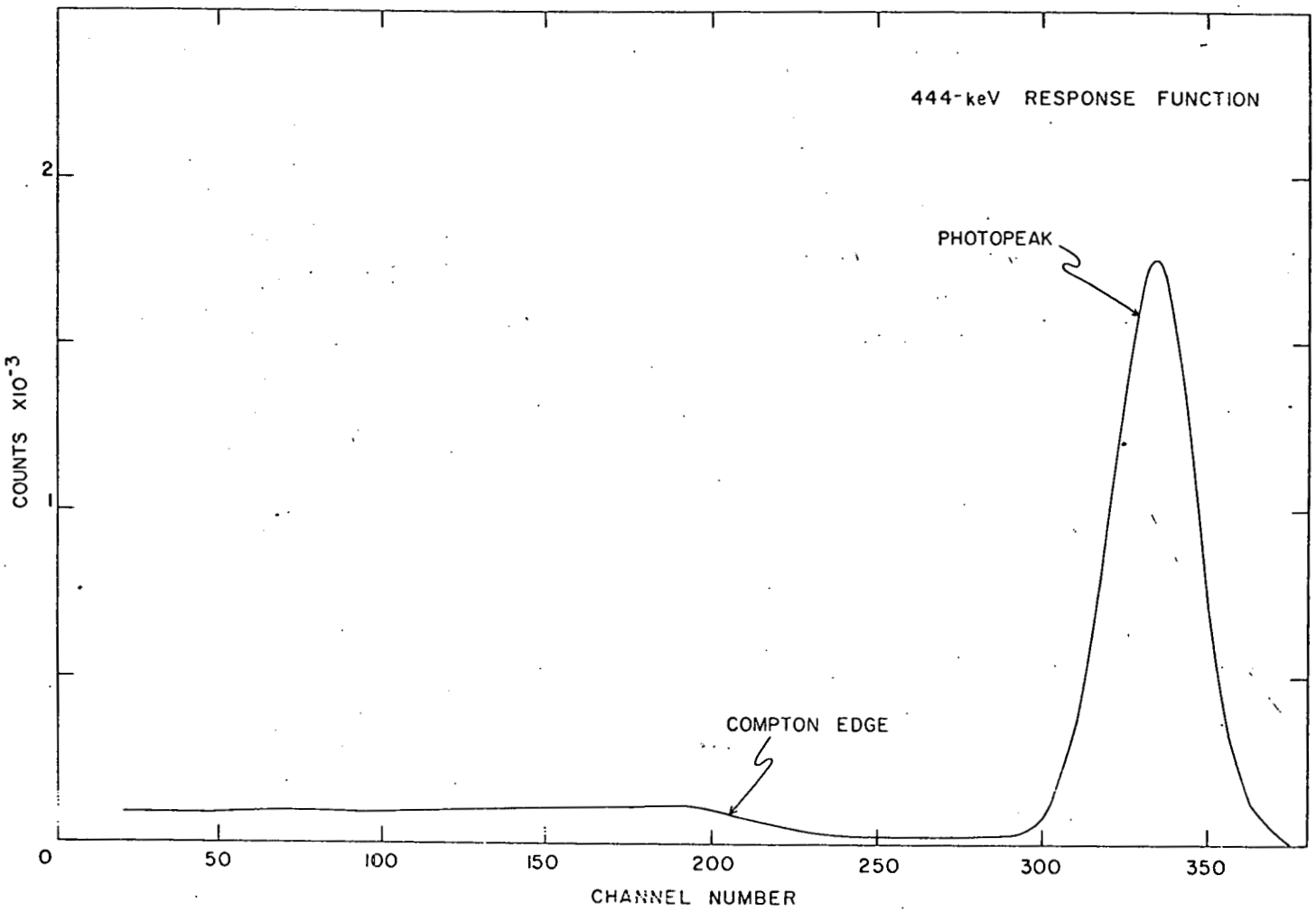

Figure 1. NaI(Tl) response function for a 444-keV gamma ray

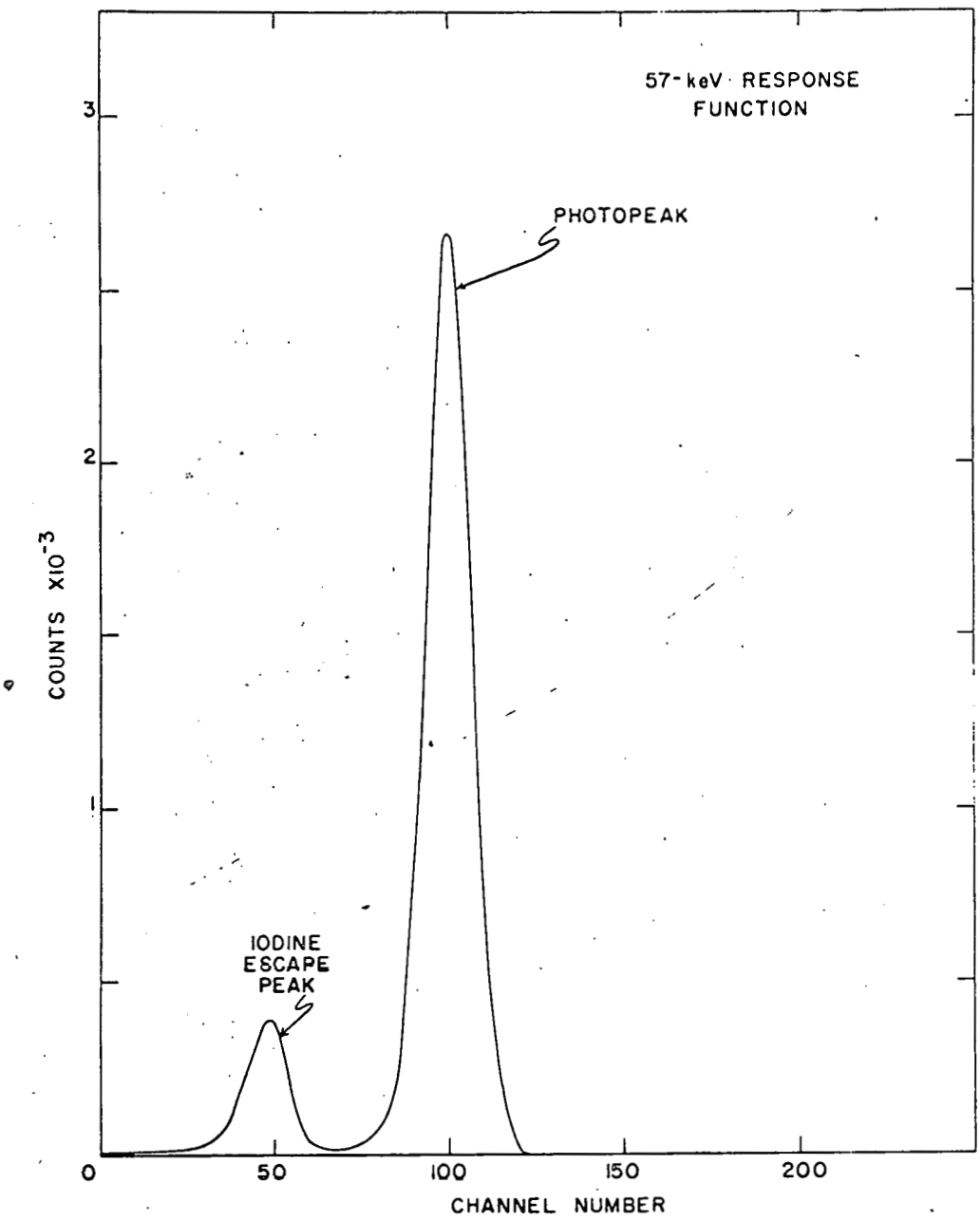

Figure 2. NaI(Tl) response function for a 57-keV gamma ray

been thus reduced to determining N_i/N_j.

It will be shown in Section II that the sum of the squares of the difference between the experimental gamma-ray pulse-height spectrum and a linear combination of the normalized gamma-ray response functions will be a minimum when the N_i's are the coefficients of the linear combination. Thus, a computer program to determine the best least-squares fit can be applied to determine the N_i's.

To obtain the needed monoenergetic response functions, the photopeaks of the measured monoenergetic emitters are fit with Gaussians. The full width at half maximum is then determined as a function of energy. The shape of the Compton continuum is also determined as a function of energy. From this an interpolation is made to determine the count rate for each channel for the particular energy desired. A computer program is then used to determine N_i/N_j. The only corrections which are necessary are the energy dependence of the efficiency of the detector and the absorption of the material between the source and the detector.

This method eliminates many of the corrections involved in the crystal diffraction method and the external conversion method. Using this method, gamma-ray relative intensities have been measured with errors of three to fifteen percent. One serious disadvantage of this method is the limited number of monoenergetic emitters. This often necessitates interpolation over a large energy range.

The method used in the present investigation was developed by Brown and Hatch (22, 26). It uses the better features of the least-squares scintillation method and of the crystal-diffraction method. Basically it consists of measuring the monoenergetic response functions of the gamma rays

of the source under investigation with a bent-crystal monochromator. A very thin line source is then placed on the focal circle of the bent-crystal spectrometer, and the diffraction crystal is removed. The collimator and detector of the spectrometer are rotated until a maximum in counting rate is observed. The composite pulse-height spectrum is then recorded in a multichannel analyzer. A linear least-squares computer program is applied to determine the relative intensities of the gamma rays. Brown and Hatch (26) found that the total response function could be used to determine the gamma-ray intensity rather than the photopeak area. This was due to the effectiveness of the collimator in reducing background. Thus, it was not necessary to know the photopeak to total ratio. They redefined the P_i's in Equation 3 to be the curve to total ratio. The curve to total ratios correct for the counts between zero energy and the energy at which the fitting procedure began. The P_i's were experimentally determined.

In summary, the present method experimentally measures the monoenergetic response functions for the gamma rays contained in the source under investigation. A linear least-squares analysis is then carried out to determine the relative intensities of the gamma rays contained in the observed pulse-height spectrum. Corrections are then applied for the efficiency of the detector, the absorption between the radioactive source and the detector and the curve to total ratio.

II. THEORY OF THE LINEAR LEAST-SQUARES SCINTILLATION METHOD

In this section the equations for the least-squares procedure will be derived following the method of Trombka (15). Let the composite gamma-ray pulse-height spectrum be represented by R_i ($i = 1, \ldots, C$) where R_i is the total number of counts in channel i due to all Q gamma rays, and C is the number of channels used to record the composite spectrum. Let a_{in} ($n = 1, \ldots, Q$) be the number of counts in channel i of a normalized monoenergetic gamma-ray response function of energy E, normalized so the area under the response function is unity, i.e. $\sum_i a_{in} = 1$. Let B_n be the area in the complex spectrum due to a gamma ray of energy E_n. Let x_i be the independent random error in channel i due to statistical fluctuations in R_i. Then, if the a_{in} are assumed to be known without error,

$$R_i = \sum_{n=1}^{Q} a_{in} B_n + x_i$$

or

$$x_i = R_i - \sum_{n=1}^{Q} a_{in} B_n \,. \qquad \text{Equation 4}$$

Now, assuming that the error x_i is random, it can be shown (27, pp. 16-20) that the probability p_i that there will be an error x_i which lies between x_i and $x_i + dx_i$ is given by

$$P_i = \frac{1}{\sqrt{2\pi\, \sigma_i^2 (R_i)}} e^{-1/2 \left(\frac{x_i}{\sigma_i (R_i)}\right)^2} dx_i \,, \qquad \text{Equation 5}$$

where $\sigma_i(R_i)$ is the standard deviation of R_i. The probability P that C errors will be observed such that x_1 is between x_1 and $x_1 + dx_1$ and x_2 is between x_2 and $x_2 + dx_2$ ... and x_C is between x_C and $x_C + dx_C$ will be a product of C terms like Equation 5, since the measurement in a given channel is independent of the measurements in the other channels.

$$P = \prod_{i=1}^{C} p_i = e^{-\sum_{i=1}^{C} \frac{1}{2} \left(\frac{x_i}{\sigma_i(R_i)}\right)^2} \prod_{i=1}^{C} \frac{dx_i}{\sqrt{2\pi\, \sigma_i^2(R_i)}} \qquad \text{Equation 6}$$

The principle of maximum probability states that the most probable values of the B_n are those values which maximize P. P is a maximum when

$$\sum_{i=1}^{C} \frac{x_i^2}{2\sigma_i^2(R_i)}$$

is a minimum. Substituting Equation 4 into this expression we are led to minimize

$$U = \sum_{i=1}^{C} \frac{\left(R_i - \sum_{n=1}^{Q} a_{in} B_n\right)^2}{2\sigma_i^2 (R_i)} \qquad \text{Equation 7}$$

with respect to B_k. Taking partial derivatives with respect to the B_k and setting them equal to zero we are led to

$$\frac{\partial U}{\partial B_K} = 0 = \sum_{i=1}^{C} \frac{(-2)\left(R_i - \sum_{n=1}^{Q} a_{in} B_n\right)(a_{iK})}{2\, \sigma_i^2(R_i)}$$

$$= \sum_{i=1}^{C} \frac{(R_i - \sum_{n=1}^{Q} a_{in}B_n)(a_{iK})}{\sigma_i^2 (R_i)} \quad . \qquad \text{Equation 8}$$

These are the normal equations. Letting $\omega_i = \frac{1}{\sigma_i^2 (R_i)}$ and $a_{ki}^T = a_{ik}$, the normal equations become

$$\sum_{i=1}^{C} a_{ki}^T \omega_i R_i - \sum_{i=1}^{C} a_{ki}^T \omega_i \sum_{n=1}^{Q} a_{in}B_n = 0. \qquad \text{Equation 9}$$

Rewriting Equation 9 in matrix notation we have

$$(A^T W A)B = A^T W R$$

or

$$B = (A^T W A)^{-1} A^T W R \qquad \text{Equation 10}$$

for $A^T WA$ nonsingular. In this equation A is a C X Q matrix, W is a Q X Q diagonal matrix with the weights on the diagonal, R is a C X 1 column matrix and B is a Q X 1 column matrix. The relative intensities can then be calculated by substituting $B_i = N_i$ in Equation 3.

One of the major advantages of the linear least-squares method is that it enables one to obtain the standard deviation in the gamma-ray relative intensities. The derivation of the standard deviations of the B_i's will be found in Appendix C along with the derivation of the equation used as a figure of merit. Only the results of these derivations will be quoted here.

The expected value of the matrix R is given by

$$E(R) = \begin{pmatrix} E(R_i) \\ \cdot \\ \cdot \\ \cdot \\ E(R_C) \end{pmatrix} .$$

From the definition of covariance, the ij element of the covariance matrix is given by

$$\text{cov}(R_i, R_j) = E\left[(R_i - E(R_i))(R_j - E(R_j))\right] .$$

The covariance matrix, cov (R), has the variance of the R_i on the diagonal and zero for the off diagonal elements because the fluctuations in each channel are assumed to be independent of those in any other channel. Thus

$$\text{cov}(R) = E\left[(R - E(R))(R - E(R))^T\right] .$$

It is assumed that A and W are known without error and thus $(A^TWA)^{-1}A^TW$ is known without error. Then, it will be shown in Appendix C that when B = CR, where C is known without error,

$$\text{cov}(B) = \sigma^2 (A^TWA)^{-1} .$$

cov (B) is a Q X Q matrix with the variances of the B_i on the diagonal. It is also shown in Appendix C that an unbiased estimate of σ^2 is S^2 where

$$S^2 = \frac{\sum_{j=1}^{C} \omega_j^2 \left(R_j - \sum_{k=1}^{Q} a_{jk} B_k\right)^2}{C - Q} \quad .$$

S^2 has a χ^2 distribution and can be used as a figure of merit. The expected value of S^2 is 1.

The gamma-ray relative intensities can be then determined from

$$I_i/I_j = \frac{N_i}{N_j} \frac{e^{-\mu_j d_j} \varepsilon_j P_j}{e^{-\mu_i d_i} \varepsilon_i P_i}$$

by looking up the ε's, P's and μ's in tables and obtaining the N's from the elements of $B = (A^T W A)^{-1} A^T W R$. The standard deviations in the N's are given by

$$\sigma(N) = \sqrt{S^2 \left[(A^T W A)^{-1}\right]} \quad .$$

The standard deviations in the gamma-ray relative intensities are obtained from the fractional deviations of the gamma-ray relative intensities which are in turn determined from the square root of the sum of the squares of the fractional deviations of N, ε, P and $e^{-\mu d}$.

III. EXPERIMENTAL EQUIPMENT AND METHODS

The two meter bent-crystal spectrometer used in the present experiment is patterned after one described by Seppi et al. (28). Figure 3 is a schematic drawing and Figure 4 is a line drawing of the bent crystal spectrometer. It consists of five basic elements. These are a radioactive source, a bent diffraction crystal, a device for measuring the rotation of the diffraction crystal, a collimator to separate the direct beam from the diffracted beam, and a detector.

In the present experimental arrangement, the radioactive source consists of a quartz capillary approximately one inch long with an inside diameter varying between 0.002 and 0.020 inches. This capillary is filled with the material to be studied. The capillary is then irradiated with neutrons. Because of the solid angle involved and the poor efficiency of the diffraction crystal, sources from 0.1 curies to several curies, depending on the particular isotope under study, are needed. This is one of the limiting factors in determining which nuclei can be studied with a bent-crystal spectrometer.

After the source material has been irradiated, it is placed in a source holder which precisely positions it on the focal circle of the bent-crystal spectrometer. During the present investigation, two source holders were used. Figures 5 and 6 are line drawings of these source holders. The first source holder consists of two cylindrical lead pigs. The outer one is permanently fixed on the focal circle of the spectrometer and has a rotating shutter to allow the beam of gamma rays to reach the diffraction crystal or

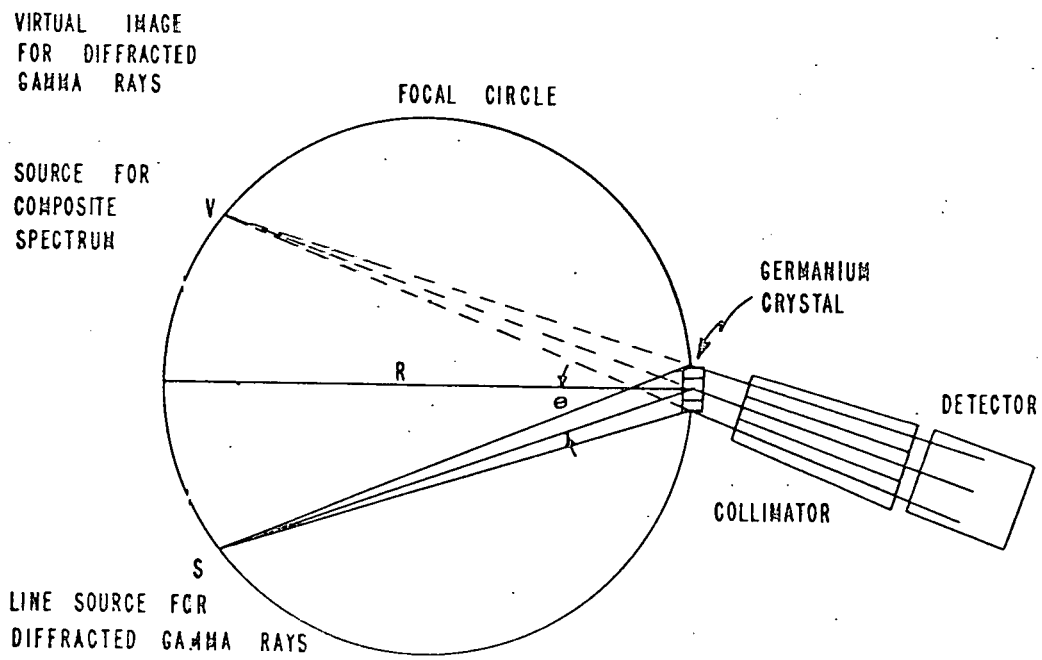

Figure 3. Schematic drawing of the bent-crystal spectrometer

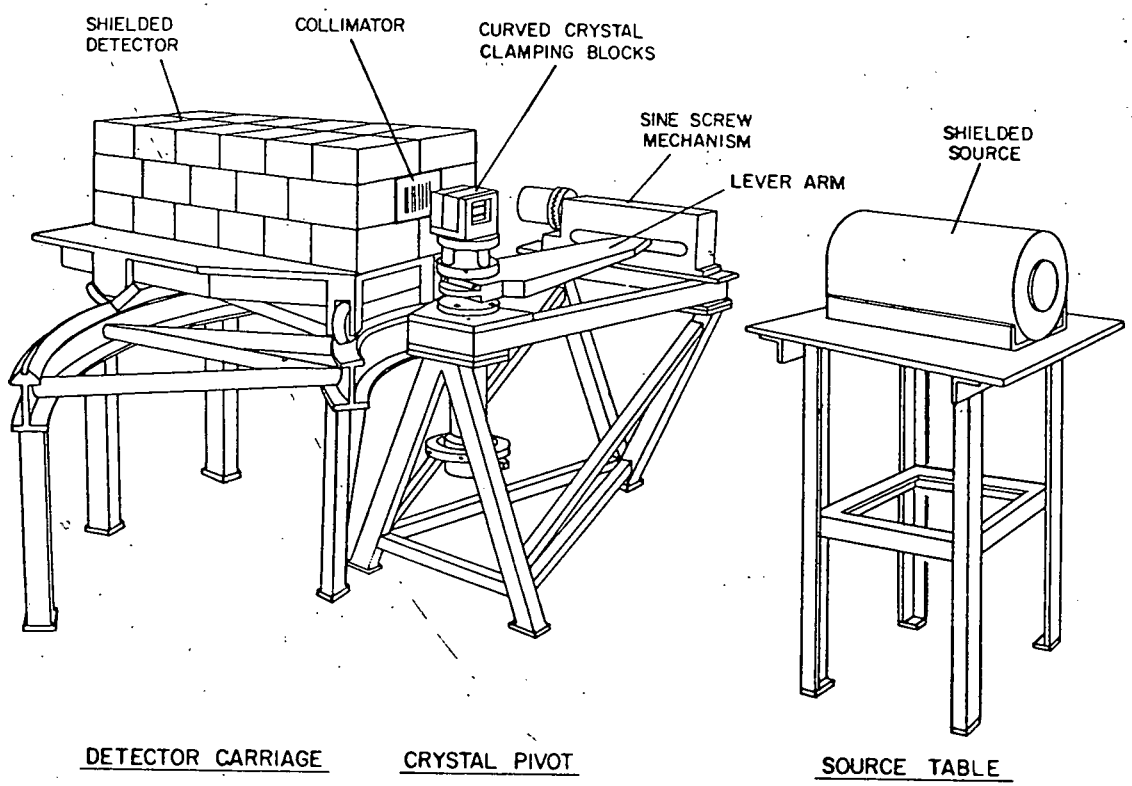

Figure 4. Line drawing of the bent-crystal spectrometer

to shield the source completely so personnel can move freely between the source and the diffraction crystal. The inner lead pig served as the source holder and a container for transporting the source. The quartz capillary containing the source material is held in a V groove by two spring clips. The bottom half of the inner pig can be raised or lowered to shield or expose the source. The inner pig is positioned in the stationary pig by three positioning screws. This source holder was very effective in working with long-lived sources.

The second source holder was designed to be used with short-lived materials. Boasso (29) has described this system in detail. Basically it consists of a rabbit made from beryllium metal and lexan plastic and a receiver to position accurately the rabbit on the focal circle of the spectrometer. Beryllium was chosen because of its small cross section for neutron capture (0.009 barns) and the long half life of the resulting activity (2.7×10^6 years). Thus, for the irradiation times of interest, very little contaminating activity would be produced from the beryllium. Lexan was chosen for its high impact strength and for its ability to retain its strength after irradiation with neutrons. The receiver can be rotated in all directions for alignment of the source, as can be seen in Figure 6. Figure 7 shows a detailed drawing of the rabbit. It has a tapered nose cone and a key slot which match a similar taper and key in the receiver. This enables the source, which is contained in a V groove in the nose cone of the rabbit, to be repositioned to less than 25×10^{-6} inches (29). The rabbit can then be placed in a closed loop with the reactor for fast transport via a pneumatic tube to and from the reactor. Since the rabbit may come out of the reactor with any orientation of the source, a means is necessary to

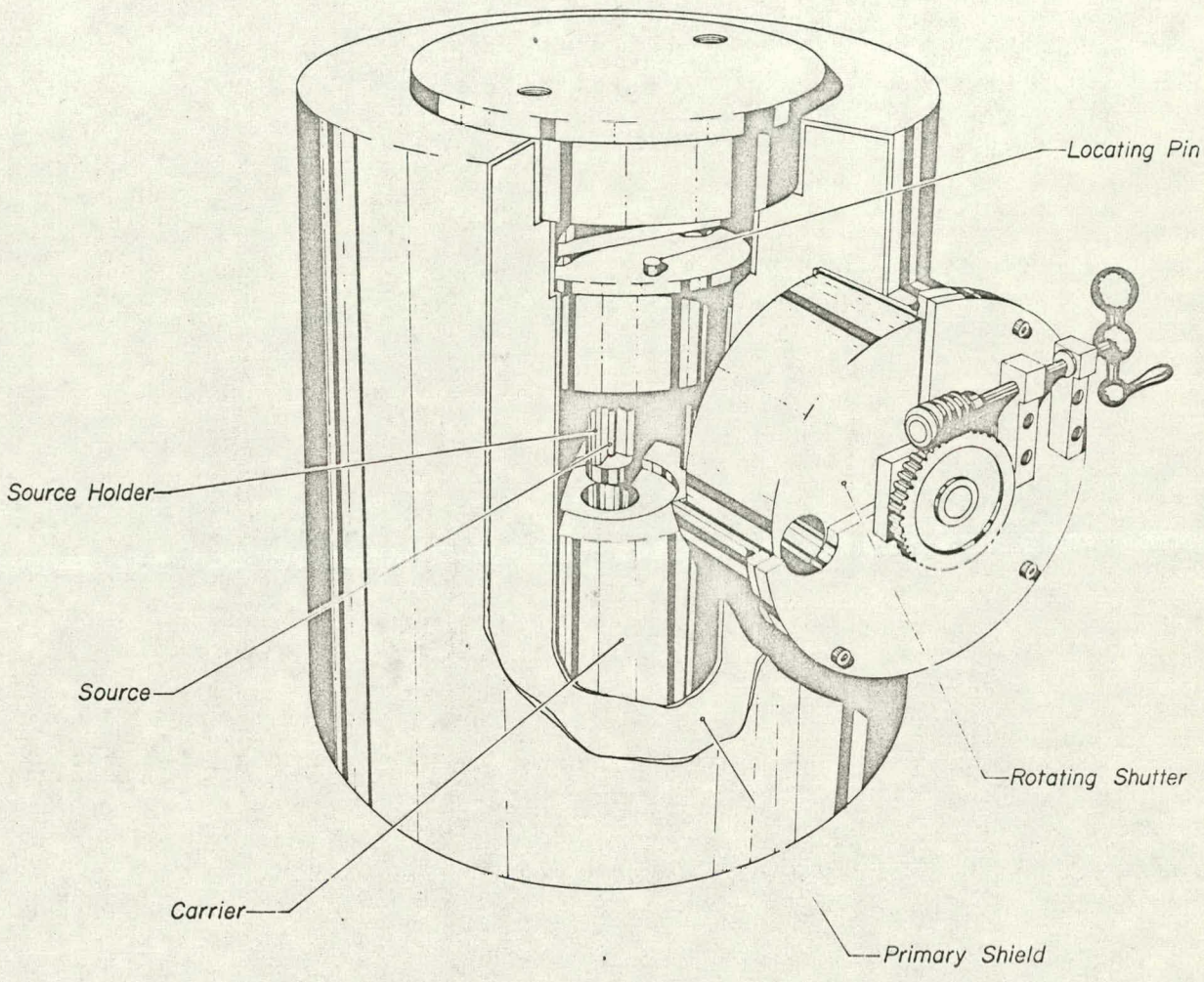

Figure 5. Original source holder used with the bent-crystal spectrometer

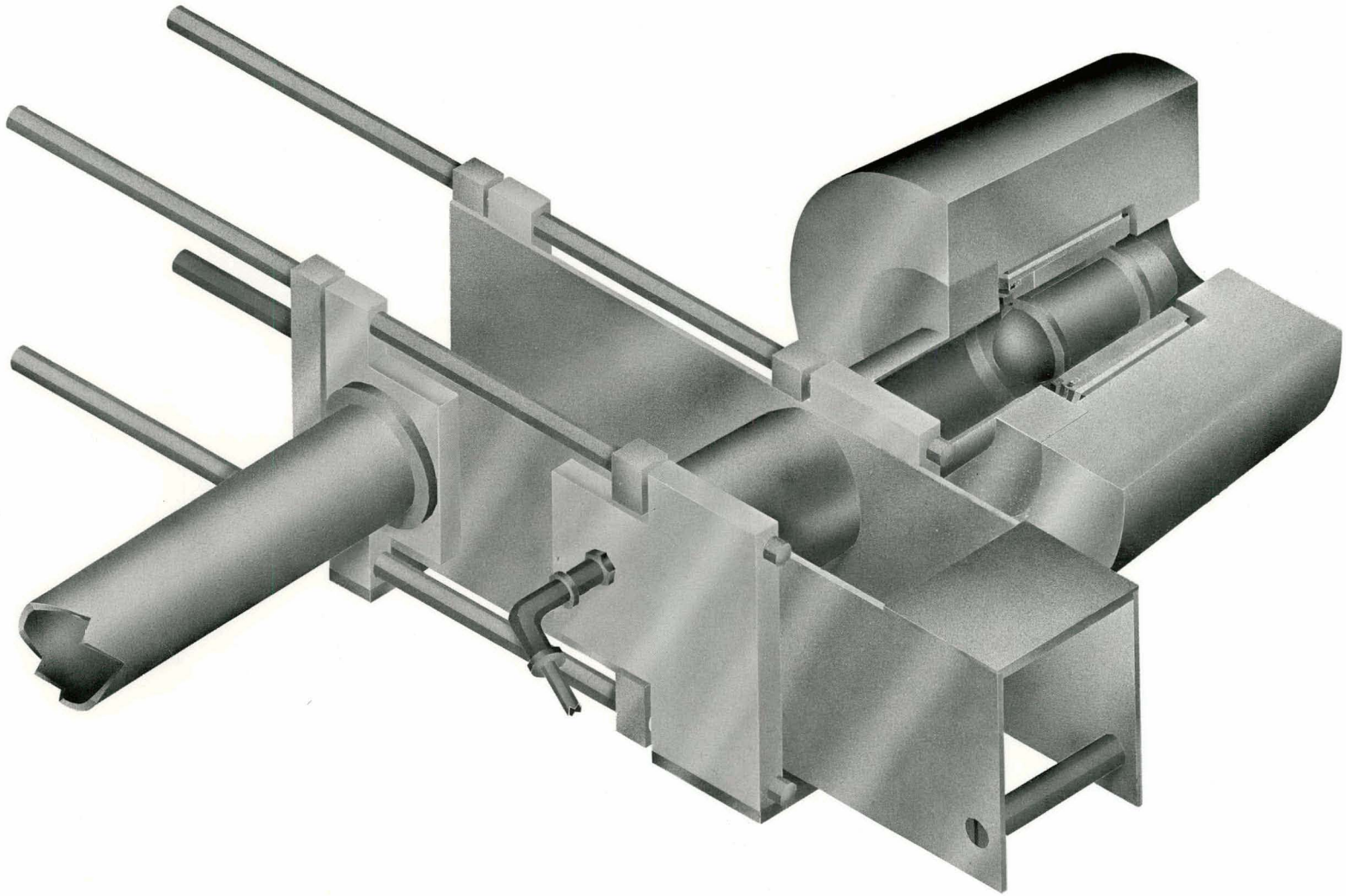

Fig 6 - Nelson IS-1230

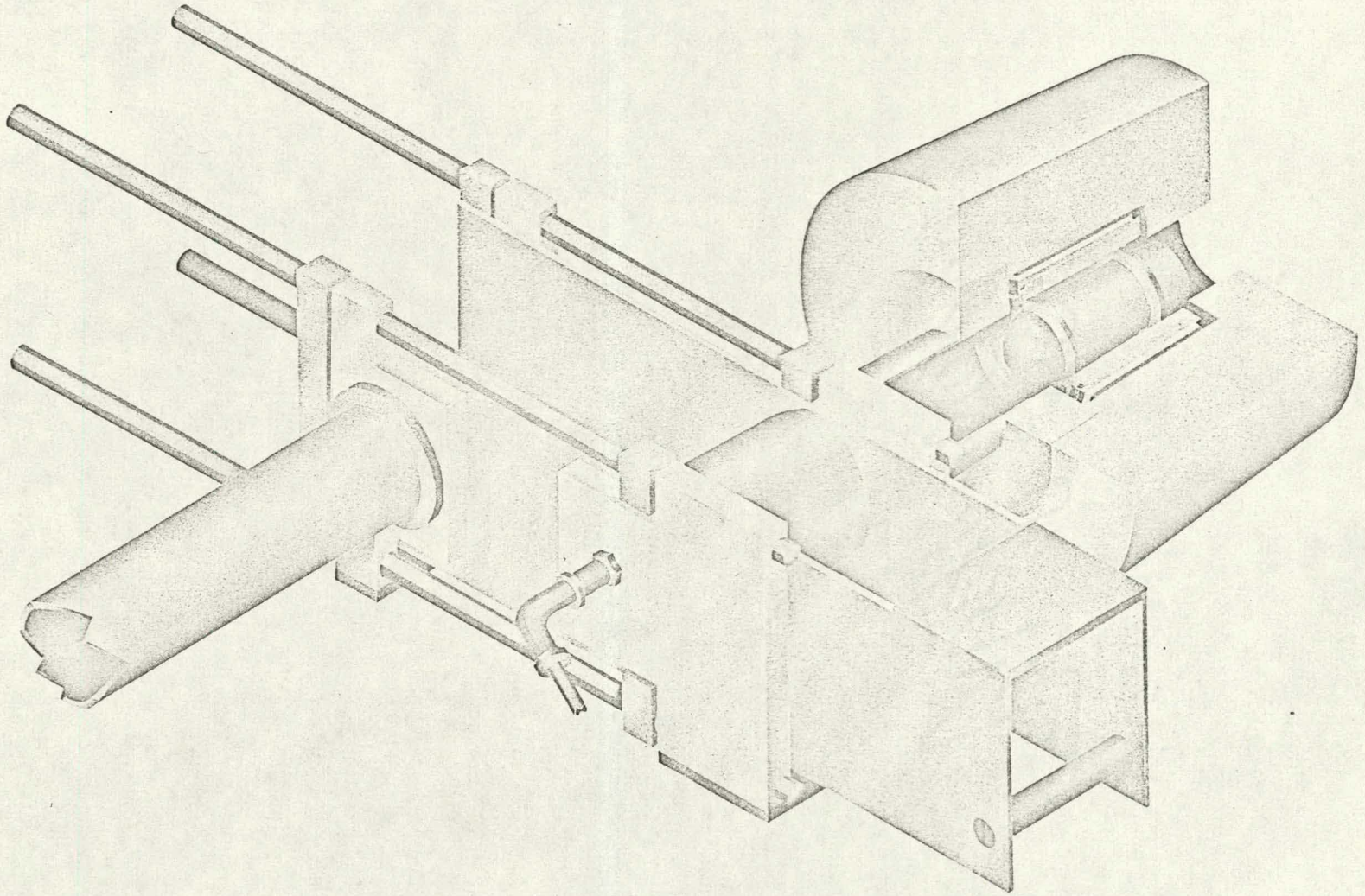

Figure 6. Line drawing of the source holder and transfer system used with the beryllium rabbit

rotate the rabbit until the source is vertical. This transfer system is shown in Figure 6. As the rabbit returns from the reactor it is slowed down and stopped by a plunger. This action trips a micro switch which starts a motor that rotates the rabbit until a pin falls into the key in the rabbit. At this time the source is vertical. An air cylinder then moves the rabbit over to the rear of the receiver and a vacuum system pulls the rabbit into the receiver. The whole process, from withdrawal from the reactor to the seating of the rabbit in the receiver, takes about 12 seconds. To irradiate the rabbit, a button is pushed which begins a sequence of withdrawing the rabbit from the receiver and moving it to the pneumatic tube to be sent into the reactor. Figure 8 is a photograph of the transfer system and the pneumatic tubes which are connected to the reactor.

If it is desired to study a nuclide which has a half-life of more than a few hours, it is necessary to irradiate the quartz capillary in one of the vertical thimbles of the reactor and then manually place the capillary in the nose cone of the rabbit. The rabbit is then placed in the transfer system which is moved behind the receiver where the vacuum system pulls the rabbit into the receiver.

In the present spectrometer, the diffraction crystal is bent to a radius of two meters as described by DuMond (30). The crystal is held between two clamping blocks which are machined to a radius of two meters. Two crystals were used in the present investigation. One was the (400) planes of a single crystal of germanium 2.75 inches wide and 3 inches long and 1.4 mm thick. The other crystal was a single crystal of quartz 2.75 inches wide, 3 inches long, and 2 mm thick cut such that the (310) planes were used for the diffraction. The quartz crystal was mainly used for X-ray measurements

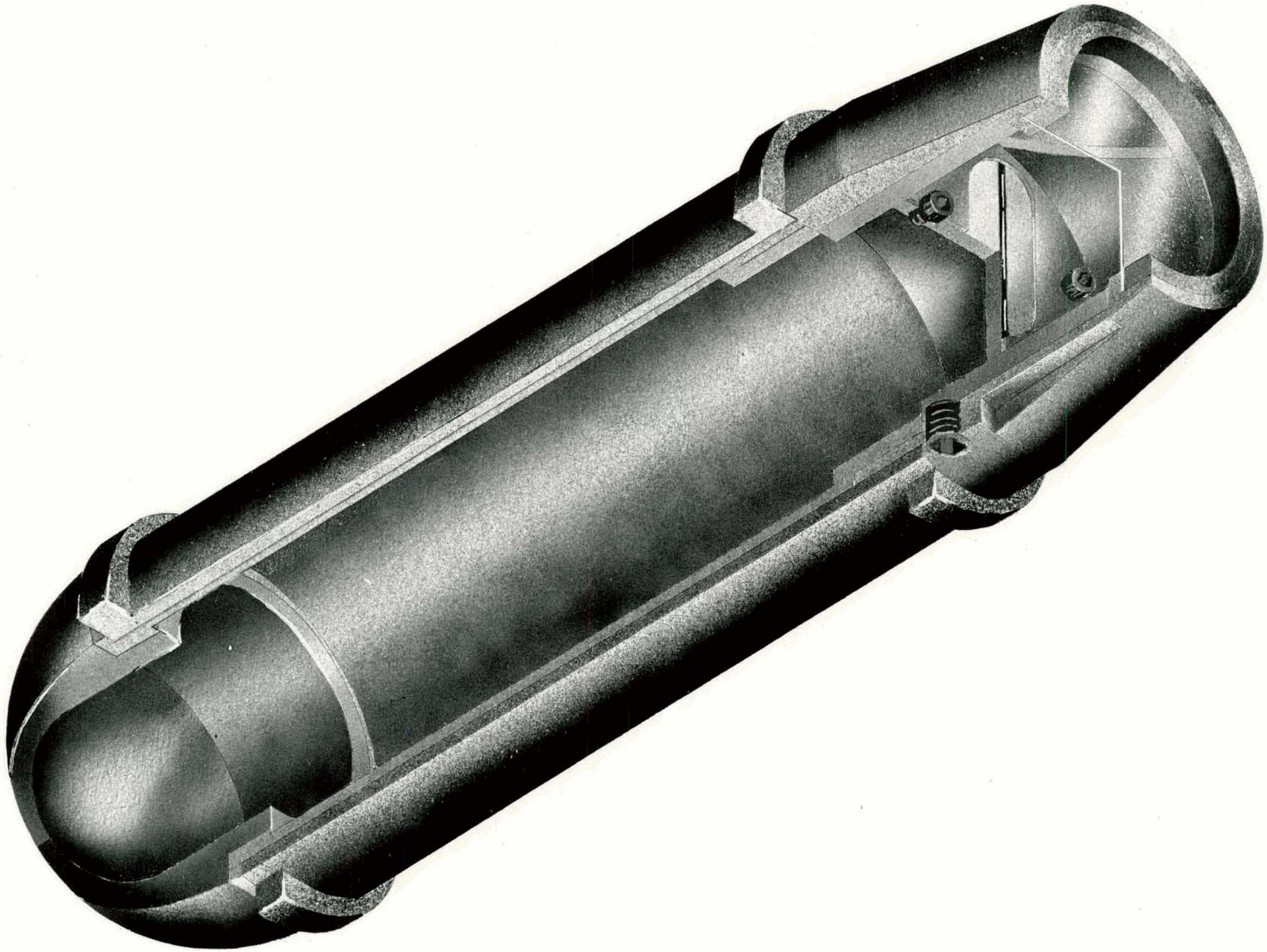

Fig 7 - Nelson . IS-1730

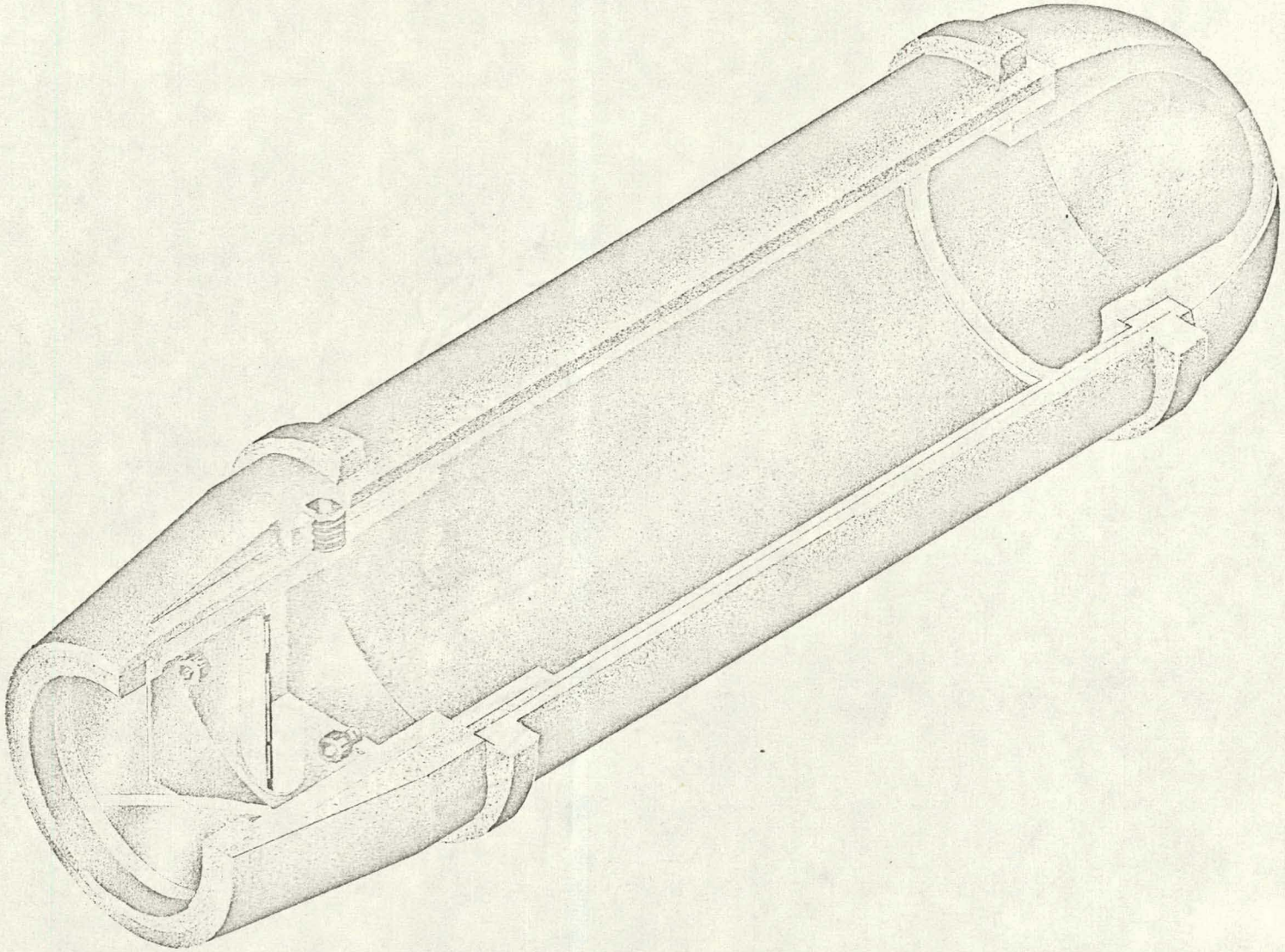

Figure 7. Line drawing of the beryllium rabbit

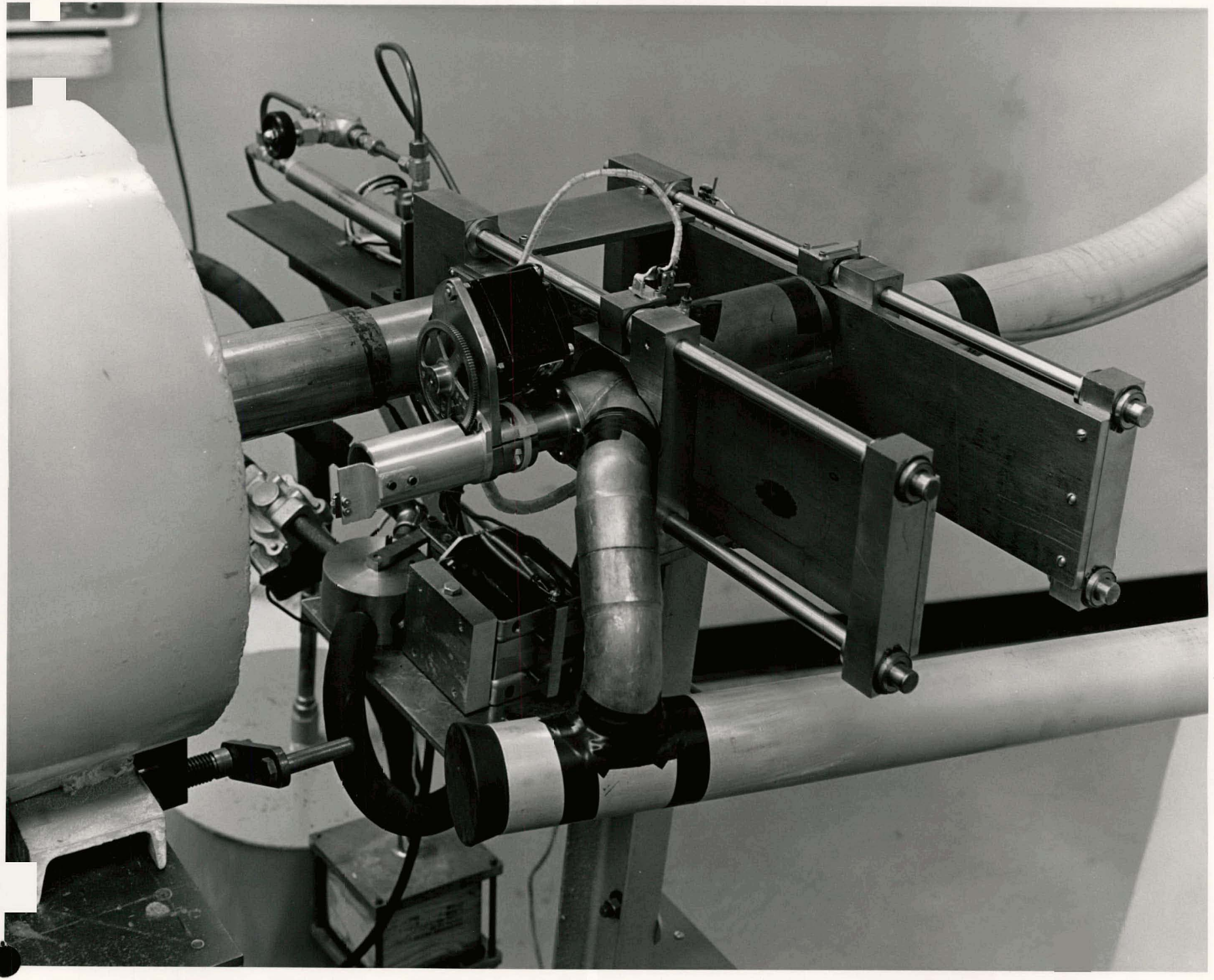

Fig 8 - IS-1730 Nelson 67-074

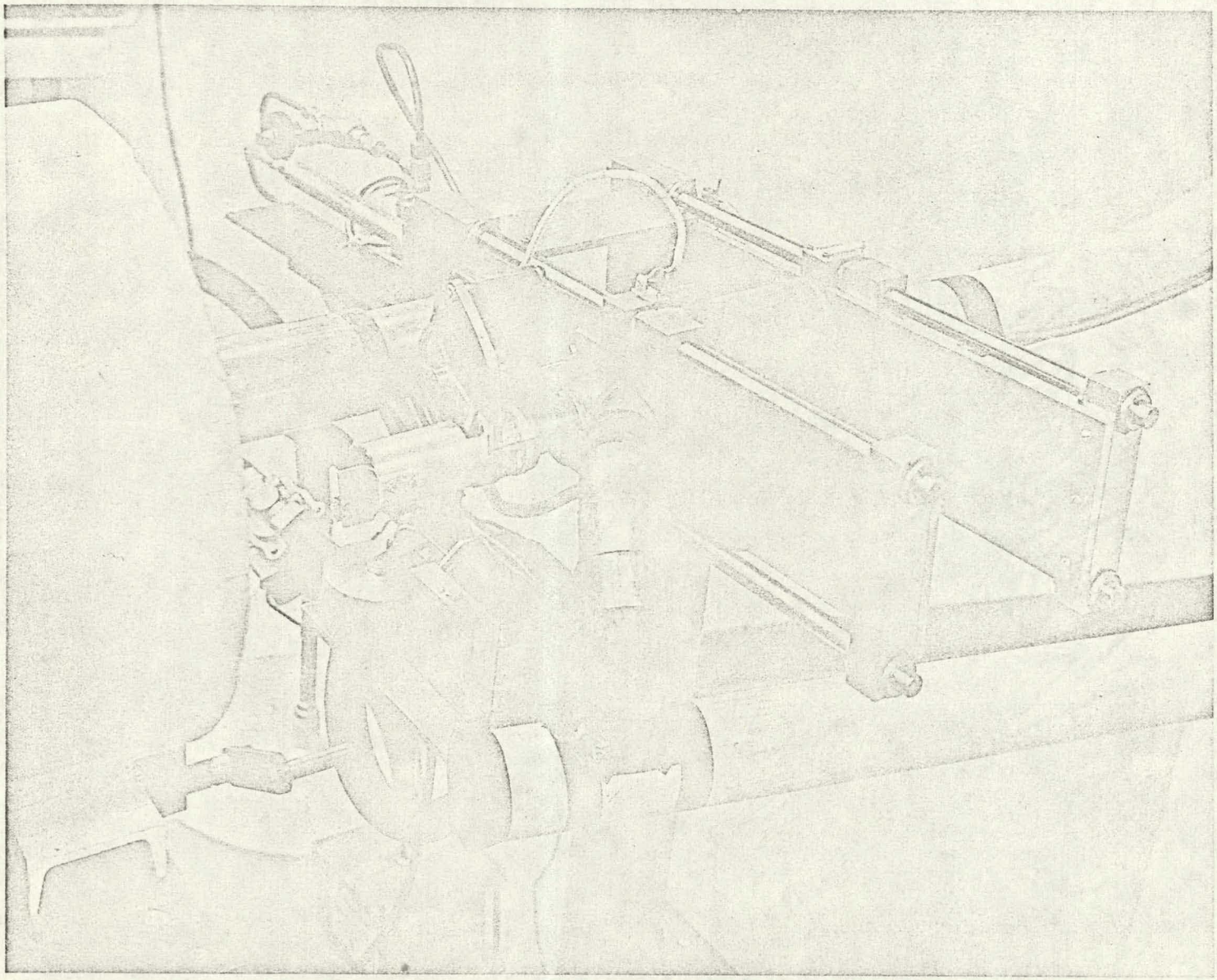

Figure 8. Photograph of the rabbit transfer system.

while the germanium crystal was used for gamma-ray measurements.

The rotation of the diffraction crystal is controlled by a precision lead screw which is connected by an arm to the diffraction crystal. The screw is 15 inches long and has 40 threads per inch. The rotation of the screw is controlled by a Datex encoderdyne and control unit. The position of the screw is read out on a set of lights on the control unit to the nearest 0.001 revolution. The screw can be controlled in two ways. In the slewing mode, the encoder runs the screw at a continuous speed until a preset position is reached. This mode is useful in going quickly from one region to another. In the second mode, the encoder steps the screw in increments of 0.002, 0.005, or 0.010 revolutions until a preset position is reached. The 0.002 revolutions corresponds to a rotation of the diffraction crystal of approximately 0.4 seconds of arc. This mode is used when searching for diffraction peaks.

The collimator consists of 30 lead plates three inches high, 18 inches long, and 0.040 inches thick. The spaces between the plates are 0.040 of an inch near the diffraction crystal and are tapered such that if the center lines of the plates were extended, they would intersect at the source position. The collimator shields the detector from the intense undiffracted beam and is very effective in reducing scattering.

The detector consists of a Harshaw Integral Line Assembly Type 12S with a 3 inch x 3 inch NaI(Tl) crystal. The NaI(Tl) crystal has a resolution of 7.5 percent for 662-keV gamma rays. The detector is placed immediately behind the collimator and is shielded by two inches of lead.

The collimator and detector rest on a table which is constrained to rotate through an angle 2θ as the diffraction crystal rotates through θ in

accordance with the mirror law. This rotation is accomplished by a gear reduction by a factor of two and a selsyn generator and receiver. This permits the diffraction crystal and source to be mechanically isolated from the detector. The diffraction crystal and source are isolated from vibrations in the floor by a concrete block one foot thick. This block rests on springs and rubber stoppers. The rubber stoppers damp out any oscillations of the concrete block. The collimator also is on a concrete block one foot thick but this block is rigidly attached to the floor since small oscillations do not effect the performance of the collimator. Figure 9 is a photograph of the bent-crystal spectrometer.

The electronic components consist of a RIDL Model 10-17 transistorized preamplifier, a RIDL Model 30-19 linear amplifier, and a RIDL Model 34-12B 400 channel multichannel analyzer. A RIDL Model 54-6 time base generator selected the counting interval for each screw setting while stepping over the diffraction peaks. A RIDL Model 33-10 single channel analyzer was used to select out the region of interest for the multichannel analyzer. The output of the multichannel analyzer was either an IBM typewriter or a Tally punch paper tape. The paper tape was converted to IBM cards on an SDS 910-IBM 1401 computer system. The power for the photomultiplier was supplied by a Fluke Model 405B high voltage power supply. All of the electronic components were connected to a Stabiline regulated power supply. Figure 10 is a block diagram of the experimental equipment.

To measure the monoenergetic response functions it was necessary to determine what settings of the lead screw corresponded to the diffraction maxima for the gamma rays contained in the source material. This was done in the following way. From a rough energy calibration for the particular

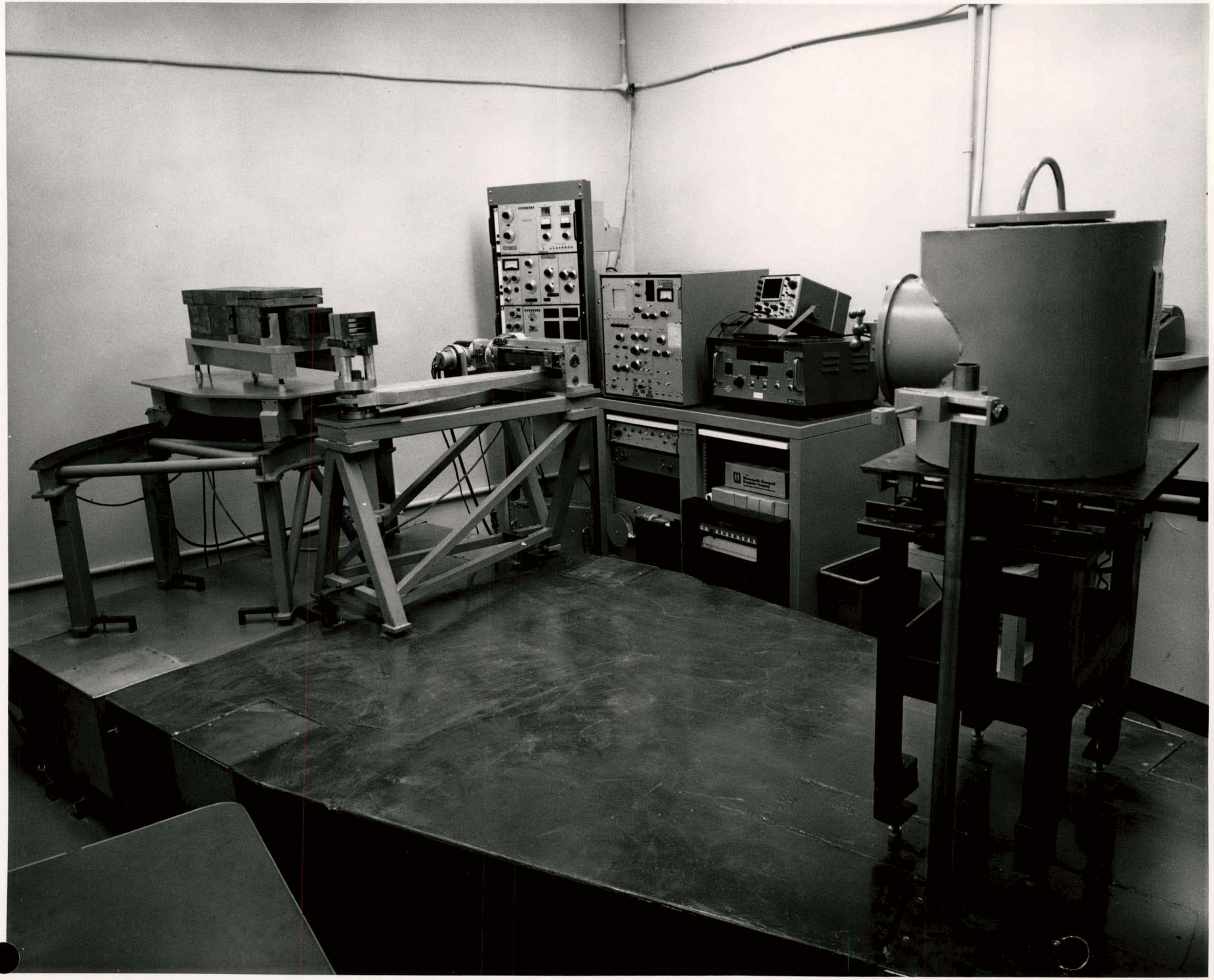

Fig 9 Nelson IS-1730

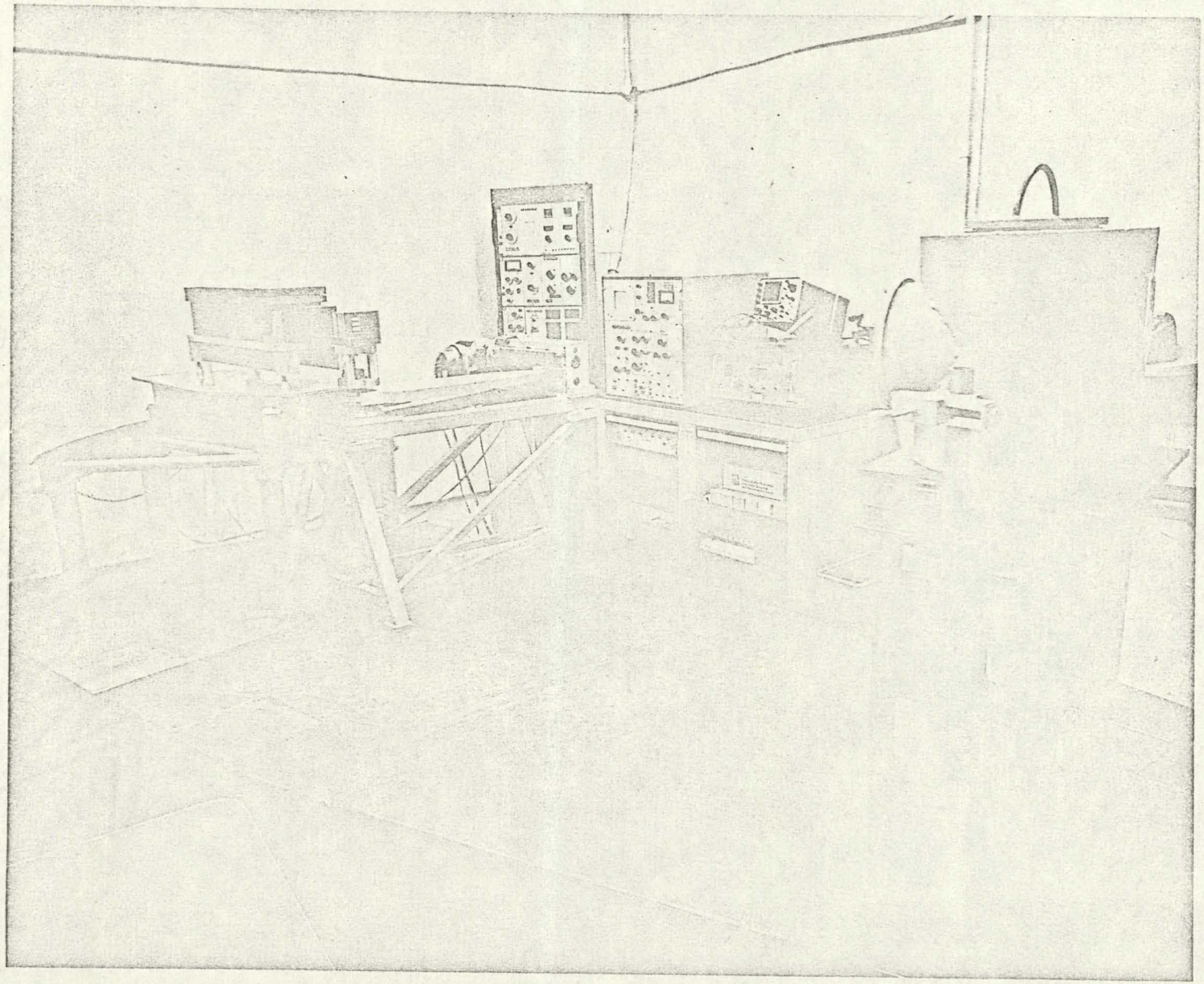

Figure 9. Photograph of the bent-crystal spectrometer and associated equipment.

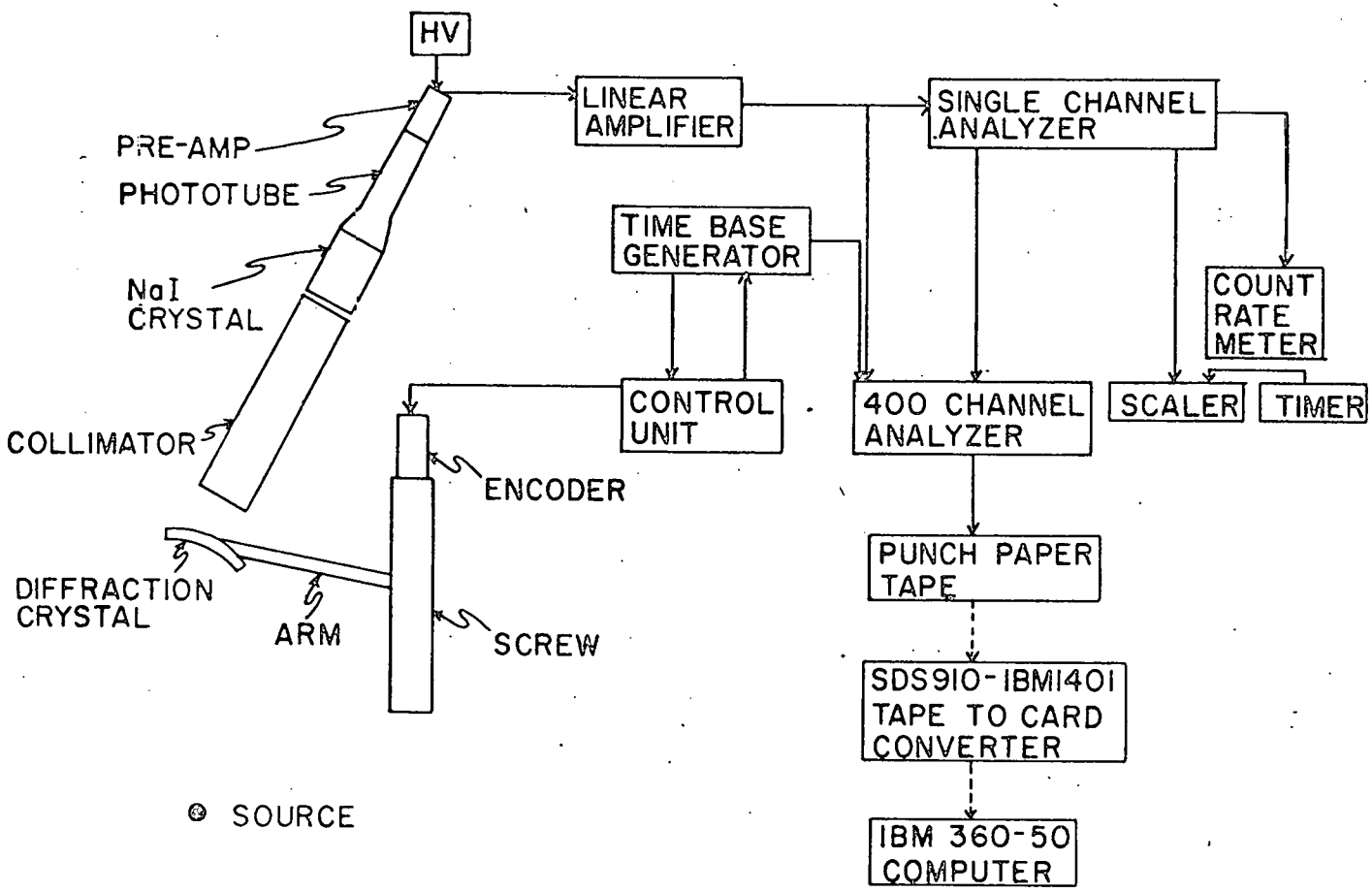

Figure 10. Block diagram of the bent-crystal spectrometer and associated equipment

diffraction crystal being used, the approximate location of the gamma rays could be determined. Searches were made in these energy regions to determine the exact location of the diffraction peaks. This was done by gating the multi-channel analyzer in the time mode with the single channel analyzer whose window was set over the desired energy region. The control unit was operated in the stepping mode and the time base generator was set at the desired time interval. All of the counts reaching the detector which fell within the window of the single channel analyzer were recorded in the first channel of the multichannel analyzer. At the end of the time interval determined by the time base generator, the screw was stepped through the chosen increment and the counts were recorded at this new setting in the second channel of the multichannel analyzer. This process was repeated until a preset position was reached on the control unit. Thus, the number of counts vs. screw setting was displayed on the oscilloscope screen of the multichannel analyzer. From this display it was possible to determine the screw setting for the diffraction peak. This procedure was repeated until the settings for all of the gamma rays had been determined. The response functions were then recorded by setting the screw at the diffraction maxima and recording the resulting pulse-height spectrum. Background was accounted for by recording the pulse-height spectrum on both sides of the diffraction peak and averaging. This was a very effective way of subtracting background since only a very small rotation of the diffraction crystal is necessary to obtain the background position. Thus, the geometry is almost identical with that of the diffraction peak position.

After the response functions had been measured, a very thin source of the same source material was placed on the focal circle of the bent-crystal

spectrometer at point V in Figure 3. The diffraction crystal was removed and the collimator and detector were rotated until a counting rate maximum was observed. The gamma-ray pulse-height spectrum from this source was then recorded. Background was determined by going off the transmission maximum and recording the pulse-height spectrum. In this way the composite gamma-ray spectrum was recorded in essentially the same geometry as the monoenergetic response functions.

The only corrections that had to be applied were the absorption in the air path between the source and detector and the absorption due to the aluminum covering of the NaI(Tl) crystal. The thickness of the material covering the NaI(Tl) crystal was obtained from the Harshaw Chemical Company at the time of purchase of the detector. The efficiency as a function of energy for the present geometry was calculated by a numerical integration computer program which is described in Appendix B.

One of the major difficulties with the least-squares method which is also true of the present method is the necessity for stability of the electronic components while the data is being taken. Various analytical schemes (19, 20, 31) have been devised for correcting for gain shifts which might occur between the recording of response functions, but no analytical method has been devised to correct for gain shifts during the recording of a response function. Several companies manufacture pulse-height stabilizers which electronically correct for gain shifts both during and between the recording of the response functions. However, all of these depend on a peak which is always present in the gamma-ray spectrum. In the present case it is not practical to place a weak gamma-ray source near the crystal to supply this peak because of the large amount of Compton distribution which would be

present. One method which has been devised is to put an Am^{241} alpha emitter in the NaI(Tl) crystal. There are very few counts below the alpha peak. However, this peak occurs at approximately 2.5-MeV in the gamma-ray spectrum and is much too high in energy for measurements where the maximum energy being studied is 500-keV as in the present case. Since in the present investigation data were recorded over a period of 5 to 10 hours, only short term stability was needed. Thus, it was practical to rely on the stability of the system during the recording of the data.

The effect of assuming that the monoenergetic response functions are known without error has been investigated by Parr and Lucas (20). In their test cases the response functions and the complex spectra had equal statistical errors. They found that the intensities of the components changed very little by including the statistical fluctuations in the response functions, but the goodness of fit did tend to decrease. They point out that this effect is normally even less important than it was in the test cases since in most practical applications, the response functions have smaller statistical errors than the complex spectra.

IV. MEASUREMENTS AND RESULTS

A. Internal Conversion Coefficients of the E2 Transitions in Yb^{170} and Er^{166}

The K internal conversion coefficients of the E2 transitions in Yb^{170} and Er^{166} were measured by determining the ratio of the K X-rays to gamma rays.

The predominant mode of decay from Tm^{170} and Ho^{166} is by beta decay to a low-lying 2^+ level in the daughter nucleus as is shown in Figure 11 (32, pp. 6-4-87, 6-4-36, 1964). Nuclear structure effects are expected to be negligible in these transitions. Church and Weneser (33) have shown that for enhanced E2 transitions the static and dynamic nuclear structure effects are very small. The K conversion coefficients for these transitions have been reported to be from 5 to 20 percent higher than the theoretical values (34-46). This investigation was undertaken to determine accurately these conversion coefficients.

1. Internal conversion coefficient of the 84.3-keV transition in Yb^{170}

The Tm^{170} sources were obtained by irradiating pure Tm^{169} in the Materials Testing Reactor at Arco, Idaho, in a neutron flux of 5×10^{14} neutrons/cm^2/sec for 28 days. The line source consisted of 5 mg $TmCl_3$ in a quartz capillary 1 inch long and 0.008 inches inside diameter. The material for the composite source consisted of 3 mg of $TmCl_3$ in a quartz capsule. By the time the sources were used the line source had a strength of approximately one curie. Because of the cross section for neutron capture of Tm^{170} (125 barns), considerable Tm^{171} will be contained in the source material

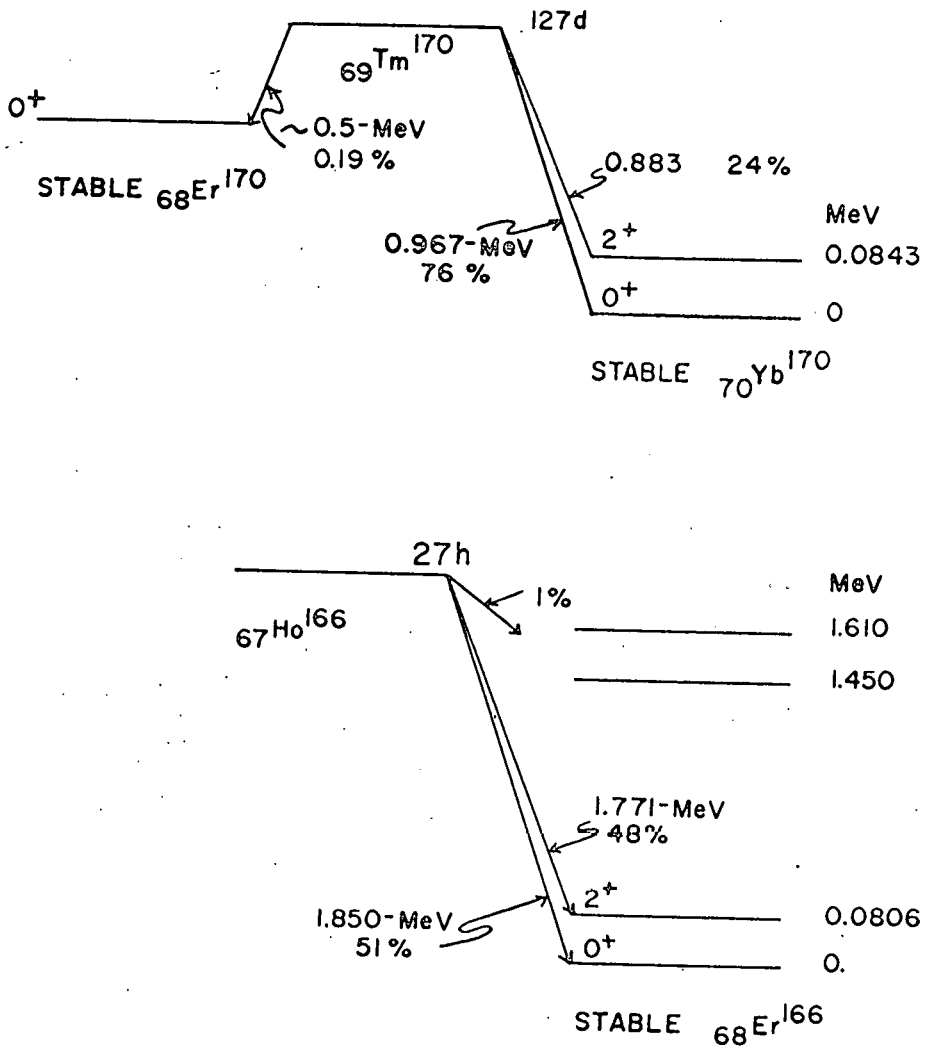

Figure 11. Decay schemes of Tm^{170} and Ho^{166} (32, pp. 6-4-87, 6-4-36, 1964)

along with the Tm^{170}. Since Tm^{171} has a half-life of 1.9 years as compared to 127 days for Tm^{170}, the percentage of Tm^{171} will increase with time. Tm^{171} beta decays to a 67-keV level in Yb^{171}. Following internal conversion of this 67-keV level, Yb X-rays will be emitted. These X-rays will have the same energy as the X-rays following internal conversion in Yb^{170} and will give erroneous results for the conversion coefficient. To eliminate the Tm^{171} from the Tm^{170} source material, the Tm^{170} was isotopically separated from the Tm^{171} in the Ames Laboratory Isotope separator. This separated source was 0.2 cm x 1.5 cm and was deposited on an aluminum foil which had a thickness of 1.75 mg/cm^2. The estimated strength of this source was 6 millicuries. Figure 12 displays a NaI(Tl) pulse-height spectrum taken with this separated source. This pulse-height spectrum consists of the 84.3-keV photopeak, X-ray photopeak, iodine escape peak due to the Yb X-rays, and a continuous gamma-ray spectrum called the bremsstrahlung spectrum. The bremsstrahlung spectrum results from absorption of the high energy beta particles. Also present in the source but not evident in Figure 12 are Er X-rays due to the K capture branch of Tm^{170} to Er^{170}. The energy of the Er X-rays is very close to the energy of the Yb X-rays and falls under the same photopeak as the Yb X-rays.

One gamma ray and six X-ray monochromatic response functions were measured with the quartz diffraction crystal. They were the 84.3-keV gamma ray, Yb $K_{\alpha 1}$, Yb $K_{\alpha 2}$, Yb $K_{\beta 1,3}$, and Yb $K_{\beta 2}$ X-ray response functions. In addition to these, response functions for the Er $K_{\alpha 1}$ and Er $K_{\alpha 2}$ X-rays were measured. The six X-ray response functions could not be fit to the X-ray photopeak in the composite spectrum because of the large amount of overlap. The procedure used instead was to fix the ratio of the Yb $K_{\alpha 1}$

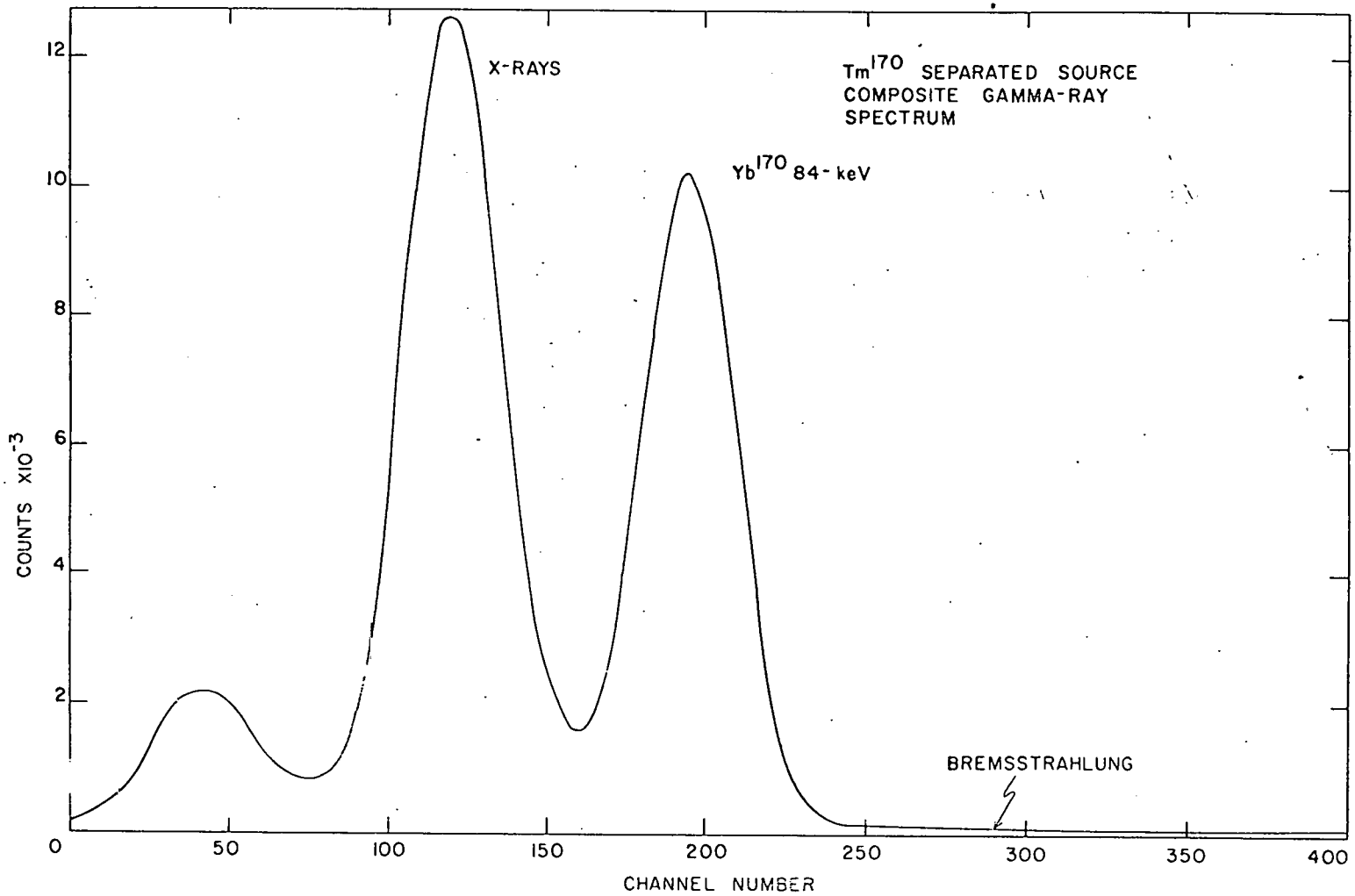

Figure 12. Yb^{170} gamma-ray spectrum taken with an isotopically separated source

X-rays to the Yb K_{α_2} X-rays at the values from the tables of Wapstra et al. (7). These tables were derived by reading the values from a graph drawn smoothly through the experimental values. Thus, a response function was obtained for the Yb K_{α} X-rays. Response functions for the Yb K_{β} and Er K_{α} X-rays were obtained in the same manner. The Er $K_{\beta 1,3}$ and $K_{\beta 2}$ X-rays were too weak in intensity for the recording of response functions. A response function for the Er K_{β} X-rays was needed, however, to obtain an accurate measurement of the Er X-ray intensity. A response function for the Er K_{β} X-rays was obtained by interpolating from the Yb K_{β} response function. The ratio of Er K_{α} to Er K_{β} X-rays was then fixed at the value from the tables of Wapstra et al. (7). Figure 13 shows four of the response functions fit by the linear least-squares computer program.

To account for the bremsstrahlung, a thin source was made from P^{32}, a pure beta emitter, which had the same dimensions as the thin source. The pulse-height spectrum from this source was then recorded in the same manner as that of the Tm^{170} thin source. This pulse-height spectrum was fit to the composite spectrum along with the X-ray and gamma-ray response functions.

Four sets of data were analyzed by the linear least-squares computer program described in Appendix D. The weighted averages for the four sets of data are

$$I(84):I(YbK_{\alpha}):I(YbK_{\beta}):I(ErK_{\alpha+\beta}) = 944\pm18:1000\pm20:263\pm10:58\pm11 \quad (47).$$

The weights used in computing the average values were the reciprocals of the squares of the estimated errors in the relative intensities for each measurement.

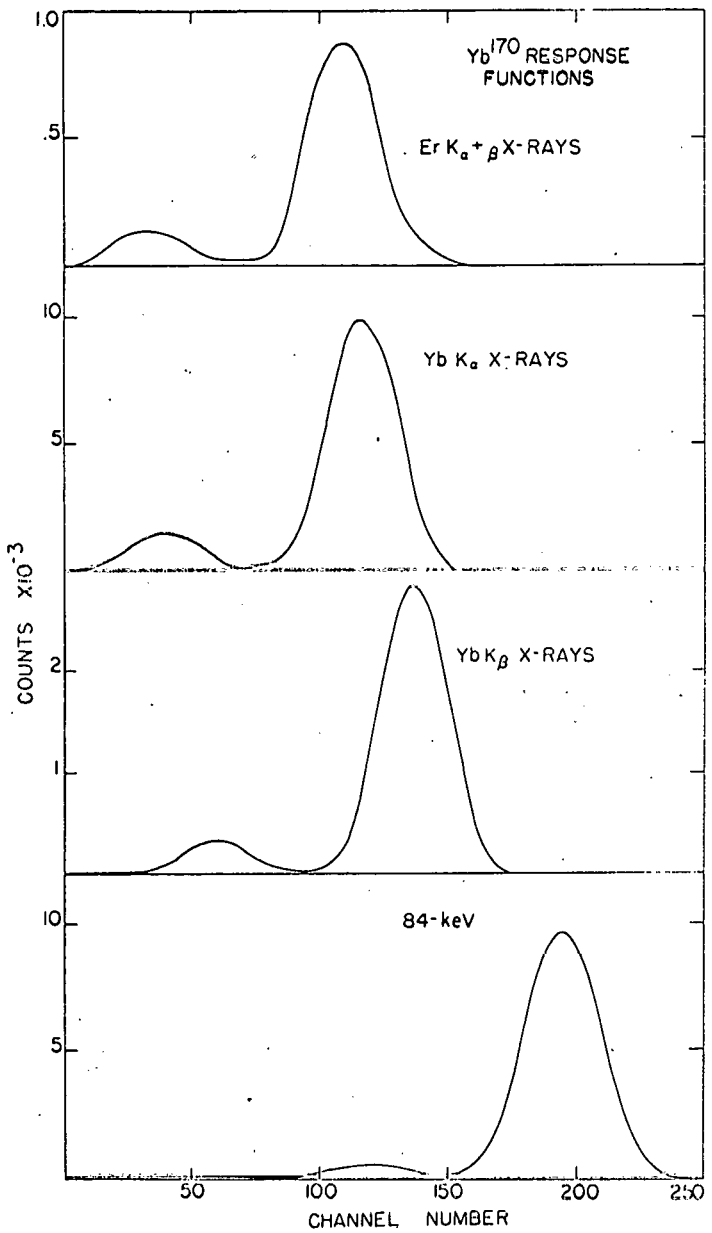

Figure 13. Yb^{170} response functions used in the least-squares fitting procedure

Figure 14 shows the fit obtained. The smooth curve is the computed composite spectrum, and the points are the experimental spectrum. The dashed curves are the response functions, which add up to the composite spectrum. The lower curve is the deviation of the experimental spectrum from the computed spectrum divided by the square root of the counts in the experimental spectrum. As an added check on the fit in the X-ray region, the ratio of K_β X-rays to K_α X-rays was determined. The experimental value was 0.263±0.011 while the expected value (7) is 0.258±0.007. The fluorescent yield from Wapstra et al. (7) for Yb is 0.937±0.005. The K conversion coefficient can then be determined from

$$\alpha_K = \frac{N_X}{\omega_K N_\gamma} \quad ,$$

where ω_K is the fluorescent yield for the K shell. The value obtained from the four sets of data was 1.43±0.04.

The total, the L, and the M+N... conversion coefficients can be determined using I(K):I(L):I(M+N+...) conversion electron intensities of Hatch et al. (34),

$$I(K):I(L):I(M+N+...) = 35.7\pm0.5:100:33.5\pm0.5.$$

The total, the L, and the M+N+... conversion coefficients can then be calculated from

$$\alpha_L = \alpha_K \cdot \frac{I(L)}{I(K)} \quad ,$$

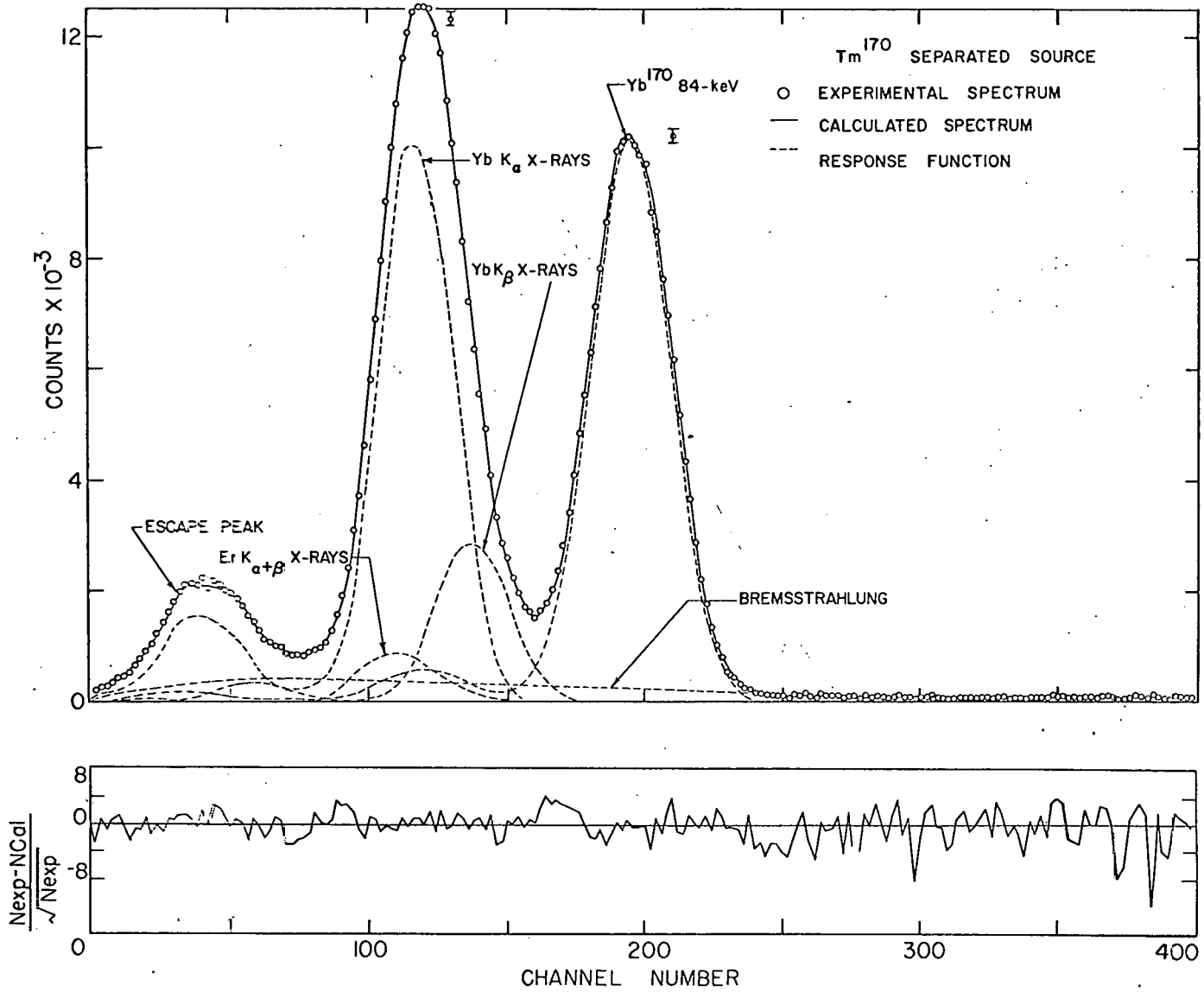

Figure 14. Yb^{170} composite spectrum with computed composite spectrum and monoenergetic components.

$$\alpha_{M+N+\ldots} = \alpha_K \cdot \frac{I(M+N+\ldots)}{I(K)}$$

$$\alpha_T = \alpha_K + \alpha_L + \alpha_{M+N+\ldots} \quad ,$$

and were determined to be

$$\alpha_L = 4.01 \pm 0.12, \ \alpha_{M+N+\ldots} = 1.34 \pm 0.05 \text{ and } \alpha_T = 6.78 \pm 0.14.$$

It was also possible to determine the K-capture branching ratio to Er^{170} from the Er K X-ray intensity relative to the Yb K X-ray intensity. The total number of decays to the 84.3-keV level can be determined from

$$\beta^-_{84} = \alpha_T^{84} \, I_\gamma^{84} + I_\gamma^{84} \quad .$$

The relative disintegration rate can then be determined from the branching ratio to the 84.3-keV level

$$\beta^- = \frac{\beta^-_{84}}{B_{84}}$$

where B_{84} is the branching ratio to the 84.3-keV level and β^- is the relative disintegration rate. If the K X-rays from conversion on the K-capture side are ignored, the K capture branching ratio can be determined from

$$B_{Er} = \frac{N_X^{Er} \, B_{84}}{\omega_K^{Er} \, I_\gamma^{84} (1+\gamma_T^{84})} \quad ,$$

where ω_K^{Er} is the K-fluorescent yield for Er and N_X^{Er} is the relative intensity of the Er X-rays with respect to the 84-keV gamma ray. The value obtained for the K-capture branch to Er^{170} from this equation is 0.19%±0.04%. This value is in agreement with the value of Day (48) of 0.15%±0.05% and of Graham et al. (35) of less than 0.3%.

In Table 1 are given the measurements of the K conversion coefficient for the 84.3-keV transition in Yb^{170} along with the methods used to determine these values. The theoretical values of Bhalla (49), Rose (1) and Sliv and Band (2) are given for comparison. The theoretical value of Bhalla was calculated for this transition while the values of Rose and Sliv and Band were interpolated from their tables. The present result is in agreement with most of the previous measurements but is five percent higher than the theoretical value of Bhalla and of Sliv and Band. The present result is in good agreement with the previous measurements of Hatch et al. (34) and Dingus et al. (36) which were obtained by two completely different methods. The value of Hatch et al. (34) was obtained by mixing the Tm^{170} source material with Te^{123m}. A magnetic beta-ray spectrometer was used to measure the conversion electron relative intensities, and a bent-crystal spectrometer was used to measure the gamma-ray relative intensities. The absolute conversion coefficient for the 84.3-keV transition was then obtained by using the 159-keV transition in Te^{123} for normalization. The value of Dingus et al. (36) was obtained by fitting analytical expressions with a non-linear least-squares computer program to experimental singles and coincidence spectra which were obtained with a well-type NaI(Tl) crystal. It should be noted that the value of Dingus et al. (36) was obtained with both $TmCl_3$ and pure Tm sources and that no difference in the value of the

Table 1. K conversion coefficient of the 84-keV transition in Yb^{170}

Reference		Method	α_K	α_{Total}
Present Result		$KX/_\gamma$ (singles)	1.43±0.04	6.78±0.14
Hatch et al.	(34)	Mag Spect/Bent-xtal Spect	1.47±0.09	6.96±0.24
Dingus et al.	(36)	$KX/_\gamma$ (singles & β-γ coin)	1.47±0.05	
Hooton	(37)	$KX/_\gamma$ (singles)	$1.46\pm^{0.05}_{0.03}$	
Jansen et al.	(52)	IEC	1.36±0.10[a]	
Jansen and Wapstra	(50)	$KX/_\gamma$ (singles & β-γ coin)	1.32±0.05	
Erman and Hultberg	(53)	IEC	1.37±0.07	
Houtermans	(51)	$KX/_\gamma$ (singles)	1.34±0.08	
Thosar et al.	(54)	$KX/_\gamma$ (β-γ coin)	1.31±0.08	
Graham et al.	(35)	$KX/_\gamma$ (singles)	1.60±0.15	
Liden and Starfelt	(38)	$KX/_\gamma$ (singles)	1.56±0.15	
Croft et al.	(39)	$KX/_\gamma$ (singles)	1.66±0.11	
		$KX/_\gamma$ (singles with E_γ-KX coin)	1.52±0.07	
Bisi et al.	(40)	$KX/_\gamma$ (singles)	1.69±0.02	
		(KX)/β(γ)(β-γ coin)	1.61±0.10	
McGowan and Stelson	(41)	$KX/_\gamma$ (singles)	1.65±0.12	
Bernstein	(42)	coul excit-half life	1.41±0.11	6.7±0.4
Fossan and Herskind	(43)	coul excit-half life	1.52±0.11	7.2±0.4
Theoretical				
Bhalla	(49)		1.36	
Sliv and Band	(2)		1.36	
Rose	(1)		1.33	

[a]Originally published as $1.57^{+0.10}_{-0.15}$, but corrected value is given in Ref. 50.

conversion coefficient was detected. Thus any effects of chemical bonding on the electron wave functions are very small. It has been suggested (50) that the higher values for the conversion coefficient were obtained with flat NaI(Tl) crystals and the lower values with well type NaI(Tl) crystals. However, the value of Dingus et al. (36), which is 10 percent higher than the theoretical value, was obtained with a well-type crystal. Several of the early singles measurements were not done with an isotopically separated source and thus the reported values for the K conversion coefficient is higher than it should be. Also the reported values of Graham et al. (35), Liden and Starfelt (38), Bisi et al. (40), McGowan and Stelson (41), Houtermans (51) and Hooton (37) have not been corrected for the presence of Er X-rays. This correction would lower these K conversion coefficients. A weighted average of the values of Dingus et al. (36), Hatch et al. (34) and the present result which were obtained by three different methods and which are in good agreement is presented here as an average experimental value for the conversion coefficient of the 84.3-keV transition in Yb^{170}. This value is

$$\alpha_K = 1.45 \pm 0.04.$$

2. Internal conversion coefficient of the 80.6-keV transition in Er^{166}

The Ho^{166} sources were made by irradiating pure Ho^{166} in a neutron flux of 3×10^{13} neutrons/cm^2/sec for 24 hours in the Ames Laboratory Research Reactor. The line sources consisted of 19 mg of HoO_2 in a quartz capillary 1 inch long and 0.015 inches inside diameter. The material for the thin source consisted of 0.3 mg of HoO_2 in a quartz capsule. The thin source for the composite spectrum was made by depositing approximately 0.1 mg Ho^{166} on

a strip of aluminized mylar 0.00025 inches thick and 0.2 cm wide and 3 cm long. Figure 15 is a NaI(Tl) pulse-height spectrum of the low energy region taken with a Ho^{166} source.

As can be seen from Figure 11 (32, p. 6-4-36, 1964) there is a weak beta decay to high energy states in Er^{166} which lead to high energy gamma-ray transitions. However, the K conversion coefficients of the 80.6-keV level in Er^{166} can still be measured from the ratio of K X-rays to 80.6-keV gamma rays since the high energy gamma-ray transitions are very weak in intensity and conversion coefficients for high energy transitions are small and thus produce few X-rays. However, a correction should be made under the low energy portion of the spectrum for the Compton distribution due to the high energy gamma rays.

The thermal neutron cross section of Ho^{165} is much larger than that of Ho^{166} so very little Ho^{167} should be produced. Any Ho^{167} that is produced can be allowed to decay out since its half-life is 3.7 hours compared to 27 hours for Ho^{166}.

As can be seen in Figure 15 the pulse-height spectrum from Ho^{166} is very similar to the pulse-height spectrum from Tm^{170}. However, there has been no observed K-capture branch to Dy^{166} (54). Thus, the X-ray photopeak only consists of Er X-rays.

Monochromatic response functions for the 80.6-keV gamma ray, Er $K_{\alpha 1}$, Er $K_{\alpha 2}$, Er $K_{\beta 1,3}$ and Er $K_{\beta 2}$ X-rays were measured with the quartz diffraction crystal. As in the Tm^{170} case, the ratios of the Er $K_{\alpha 1}$ to Er $K_{\alpha 2}$ and Er $K_{\beta 1,3}$ to Er $K_{\beta 2}$ were fixed at the values from the tables of Wapstra et al. (7). Three of the response functions used in the fitting procedure are displayed in Figure 16.

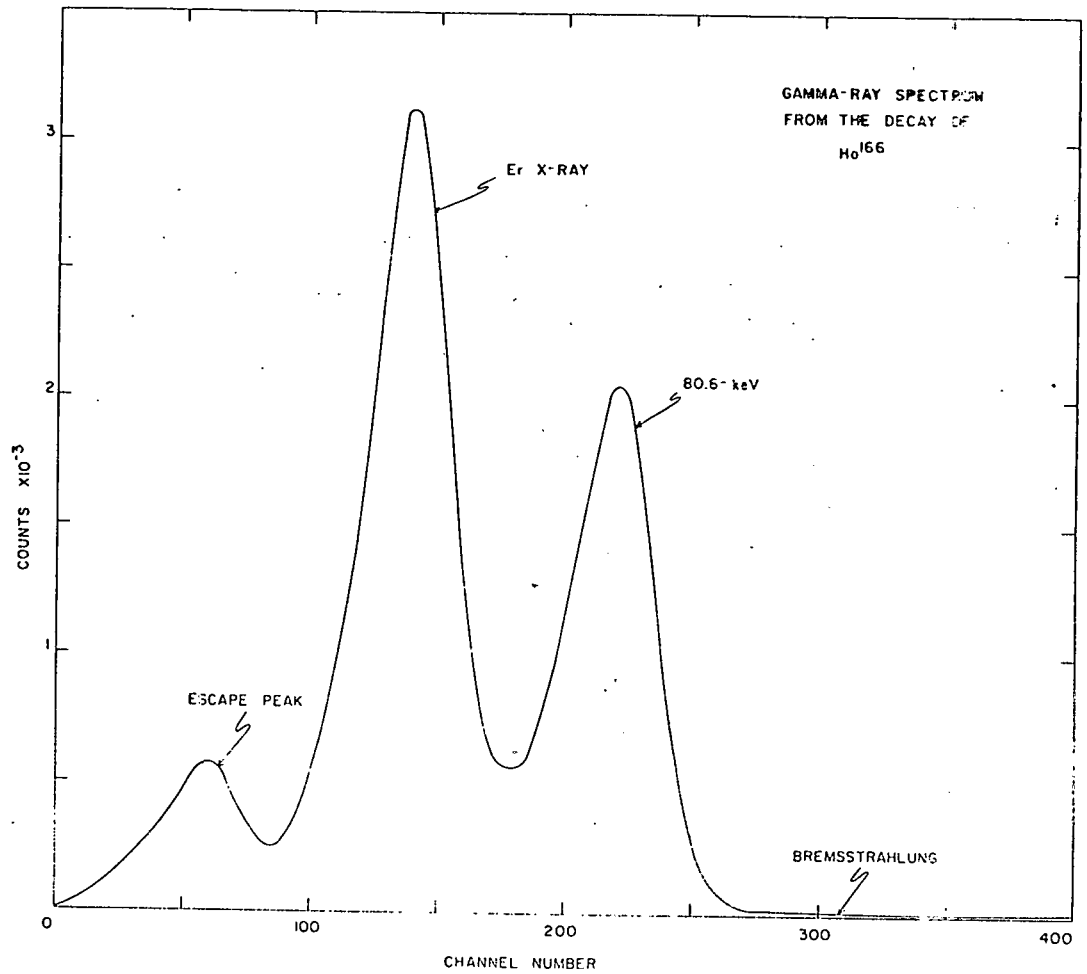

Figure 15. Er^{166} gamma-ray spectrum

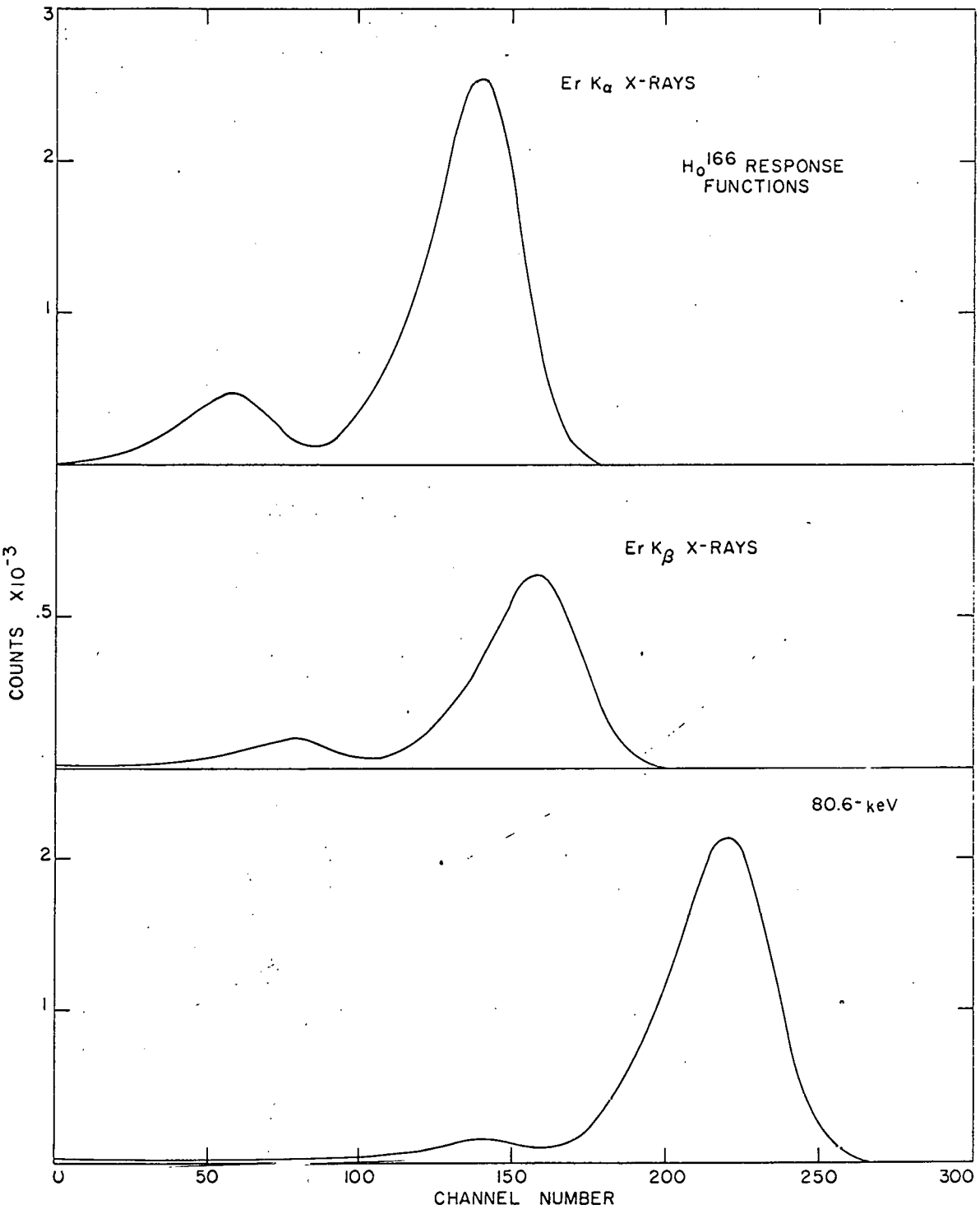

Figure 16. Er^{166} response functions used in the least-squares fitting procedure

The Compton distribution from the high energy gamma rays could not be determined directly because of their weak intensity and high energy. Instead, the Compton distribution from a Co^{60} source was recorded with the diffraction crystal removed and the collimator set at the transmission maximum. Because this Compton distribution was small, it was subtracted out before the fitting procedure was applied. The amount to be subtracted was determined from the photopeak to total ratio for the Co^{60} source and from the intensity of the high energy gamma rays in the Ho^{166} source.

To check on the contribution of Ho^{167} in the source material, data were taken two hours after irradiation and 24 hours after irradiation. No difference in the X-ray to gamma-ray ratio was detected.

Five sets of data were analyzed by the least-squares computer program which is described in Appendix D. The weighted averages for the five sets of data are

$$I(80):I(K_\beta):I(K_\alpha) = 781\pm14:253\pm9:1000\pm17 \quad .$$

Again the weights were the reciprocals of the squares of the estimated errors in the intensities for each measurement. A least-squares fit to the data is shown in Figure 17. The experimental value of the ratio of K_β X-rays to K_α X-rays was 0.253±0.010, and the expected value (7) is 0.253±0.007. The K conversion coefficient obtained from

$$\alpha_K = \frac{N_X}{\omega_K N_\gamma}$$

was determined to be $\alpha_K = 1.72\pm0.06$. The fluorescent yield, ω_K, from Wapstra et al. (7) was 0.932±0.005. In Table 2 is given the present value along

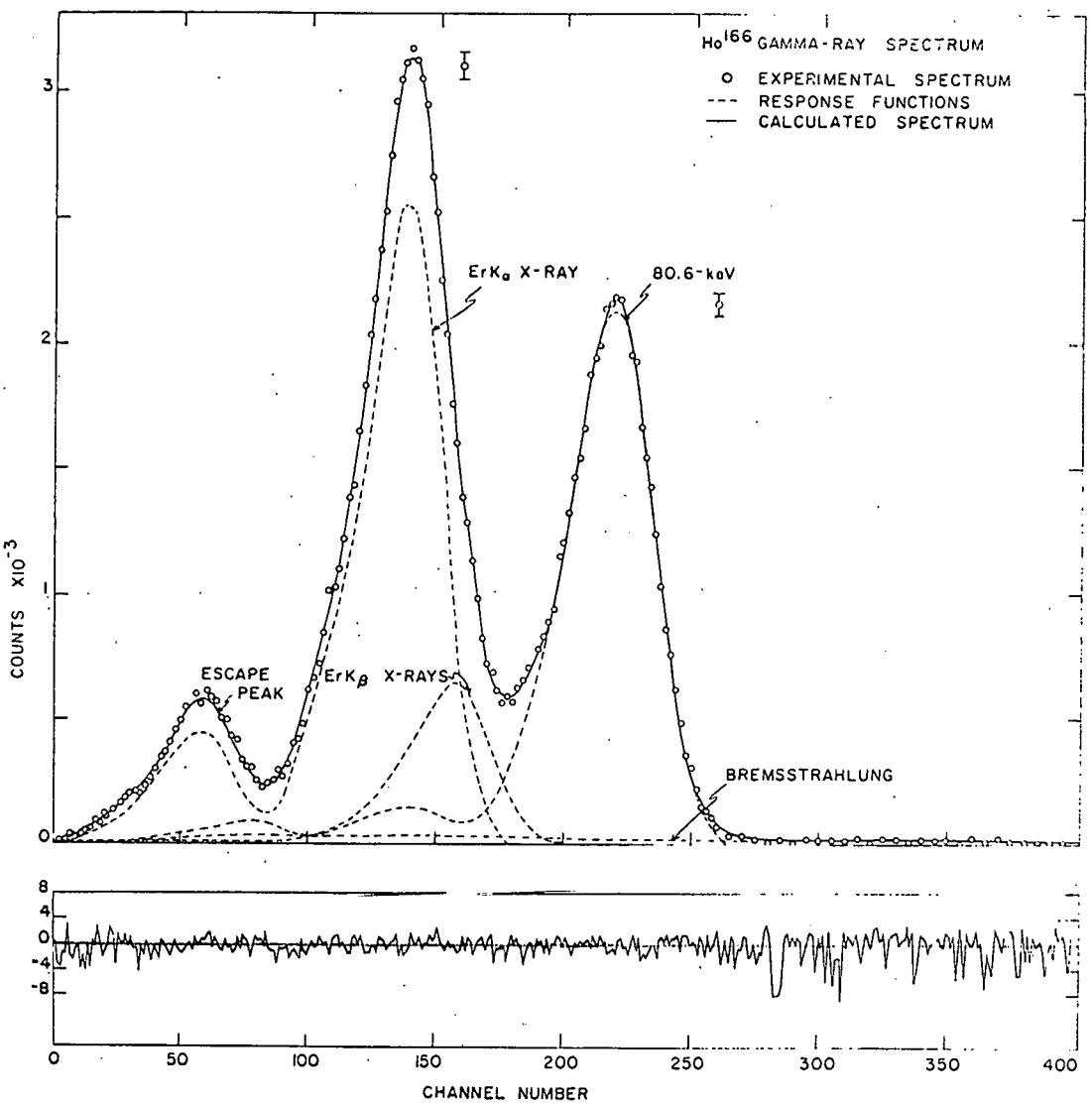

Figure 17. Er^{166} composite spectrum with computed composite spectrum and monoenergetic components

Table 2. K conversion coefficient of the 80-keV transition in Er^{166}

Reference		Method	α_K
Present Result		KX/γ (singles)	
Sunyar	(44)	KX/γ (singles)	1.9±0.2
McGowan and Stelson	(41)	KX/γ (singles)	1.85±0.13
Helmer and Burson	(55)	KX/γ (singles)	1.7±0.3
Marklund et al.	(45)	KX/γ (singles)	1.76±0.15
Foglio and Bettoni	(46)	KX/γ	1.75±0.07
Thosar et al.	(54)	KX/γ (singles and β-γ coin)	1.67±0.07
Erman and Hultberg	(53)	IEC	1.68±0.15
Theoretical			
Bhalla	(49)		1.62
Sliv and Band	(2)		1.66
Rose	(1)		1.60

with the previously determined values of the K conversion coefficient for the 80.6-keV transition in Er^{166}. The theoretical values of Bhalla (49), Rose (1) and Sliv and Band (2) are given for comparison. The value of Bhalla was calculated for this transition, while the values of Rose and Sliv and Band were interpolated from their tables. The present value is in agreement with all of the previous measurements but is six percent higher than the theoretical value of Bhalla (49).

3. Discussion of the E2 internal conversion coefficients in Yb^{170} and Er^{166}

The present results for the K internal conversion coefficients for the 84.3-keV transition in Yb^{170} and the 80.6-keV transition in Er^{166} are about 5 percent higher than the theoretical values. While this is not a significant difference, it is interesting to note that they are of the same magnitude and in the same direction. The 10 to 20 percent deviations which had previously been reported were not observed. The present value for the conversion coefficient of the 84.3-keV transition in Yb^{170} is in good agreement with the values reported by Dingus et al. (36) and Hatch et al. (34) which were determined by completely different methods. The present results for the 80.6-keV transition in Er^{166} agrees, within the experimental error, with all of the values which have previously been reported. It is slightly higher, however, than the value reported by Thosar et al. (54) and Erman and Hultberg (53) which are in agreement with the theoretical value.

Recently Gelletly et al. (56) have reported the L subshell ratios for several E2 transitions including Yb^{170} and Er^{166}. They report the L_{II}/L_{III} subshell ratios agree with the corresponding theoretical values to less than 2 percent while the L_I/L_{II} and L_I/L_{III} ratios are about 5 percent higher than the theoretical values. This deviation is the same magnitude and in the same direction as the deviation of the K conversion coefficients for these transitions. A possible explanation of the difference between the experimentally determined and theoretically calculated L_I/L_{II} and L_I/L_{III} subshell ratios and the difference between the experimental and theoretical K conversion coefficients is that the s electron wave functions are altered

due to the s electrons penetrating the nucleus. The p and d electron wave functions are not altered since these electrons do not penetrate the nucleus.

B. Internal Conversion Coefficients in Hf^{180}

The level structure in the nucleus Hf^{180} following the decay of Hf^{180m} is shown in Figure 18 (32, p. 6-6-121, 1965). An interesting feature of this decay is that the decay of the 641-keV level consists of three E2 transitions in cascade with no observed crossover transitions. This means that the total transition intensities of these three transitions are equal. It is possible to use this fact to determine the total internal conversion coefficient, α, for the 93.3-keV transition from a measurement of the gamma-ray relative intensity of this transition along with that of the 332-keV transition. Measurements of the gamma-ray relative intensities and internal conversion electron relative intensities for all of the other observed transitions enable the determination of the internal conversion coefficients for the transitions using the previously determined coefficient (α_T) for the 93.3-keV transition for normalization.

Edwards and Boehm (57) have carried out precise measurements of the gamma-ray and internal conversion line relative intensities and have obtained accurate values for the Hf^{180} internal conversion coefficients through a least-squares adjustment of their data. They report that the K-shell internal conversion coefficient for the 93.3-keV transition was in agreement with theory and those for the 215.3-, 332.5-, and 443.8-keV transitions were approximately 10 percent lower than the theoretical coefficients of Rose (1). Although such a discrepancy could not be considered very significant, the fact that the deviation is of the same size and in the same

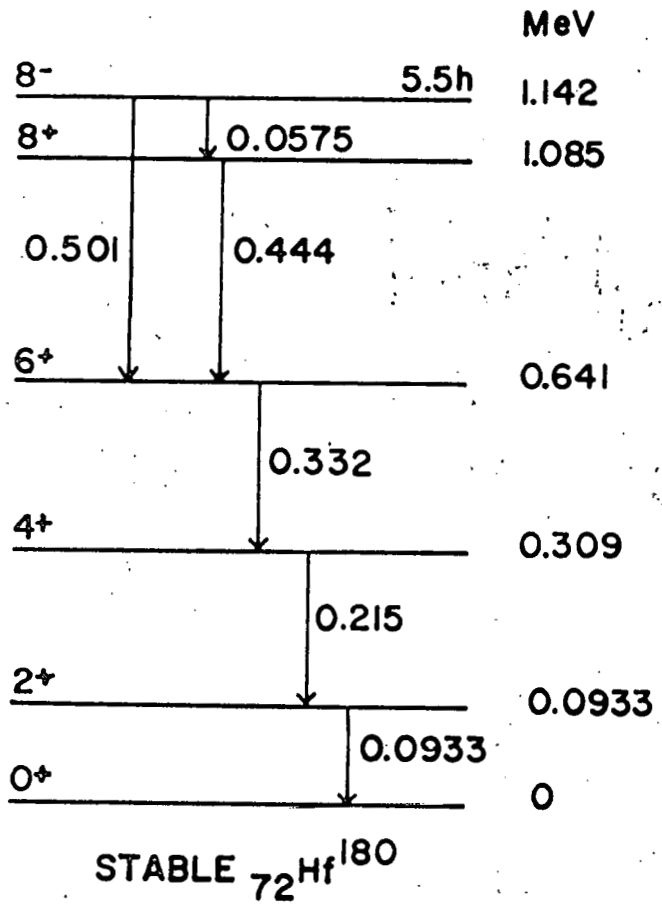

Figure 18. Decay scheme of Hf^{180m} (32, p. 6-6-121, 1965)

direction for each of the latter three E2 transitions is interesting. This deviation is larger than would be expected based on most of the recent results for high precision determinations of α_K for pure E2 transitions.

1. Analysis of the Hf^{180} X-ray and gamma-ray spectrum

Figures 19 and 20 show NaI(Tl) and Ge(Li) pulse-height spectra from the decay of 5.5 hour Hf^{180m}. To obtain the relative intensities of the X-rays and gamma rays, the spectrum was divided into two overlapping sections. The region from 93.3-keV to 501-keV will be called the "gamma-ray" portion of the spectrum, and the region up to 215-keV will be called the "X-ray" portion of the spectrum. In the gamma-ray portion the relative intensities of the gamma rays from 93.3-keV through 501-keV were determined, while in the X-ray portion the relative intensities of the X-rays and 57-keV gamma ray were determined using the 93.3-keV and 215-keV gamma rays for normalization. The line sources for the two sections were made by filling quartz tubes, which were about 1 inch long with an inside diameter of about 0.2 mm, with approximately 12 mg of HfO_2. The material for the gamma-ray portion of the spectrum was enriched to 57 percent in Hf^{179} and contained 30 percent Hf^{180}, while the material for the X-ray portion of the spectrum was enriched to 87 percent in Hf^{179} and contained 8.6 percent Hf^{180}. The materials for the sources were irradiated with neutrons in the Ames Laboratory Research Reactor in a neutron flux of 7×10^{13} neutrons/cm^2/sec for 10 hours. The 5.5 hour Hf^{180m} activity was obtained from single neutron capture by the Hf^{179}. The 45 day Hf^{181} activity was also present in the sources. The time from the reactor shut down until data were taken was approximately two hours. Data could be taken during approximately two half lives for each

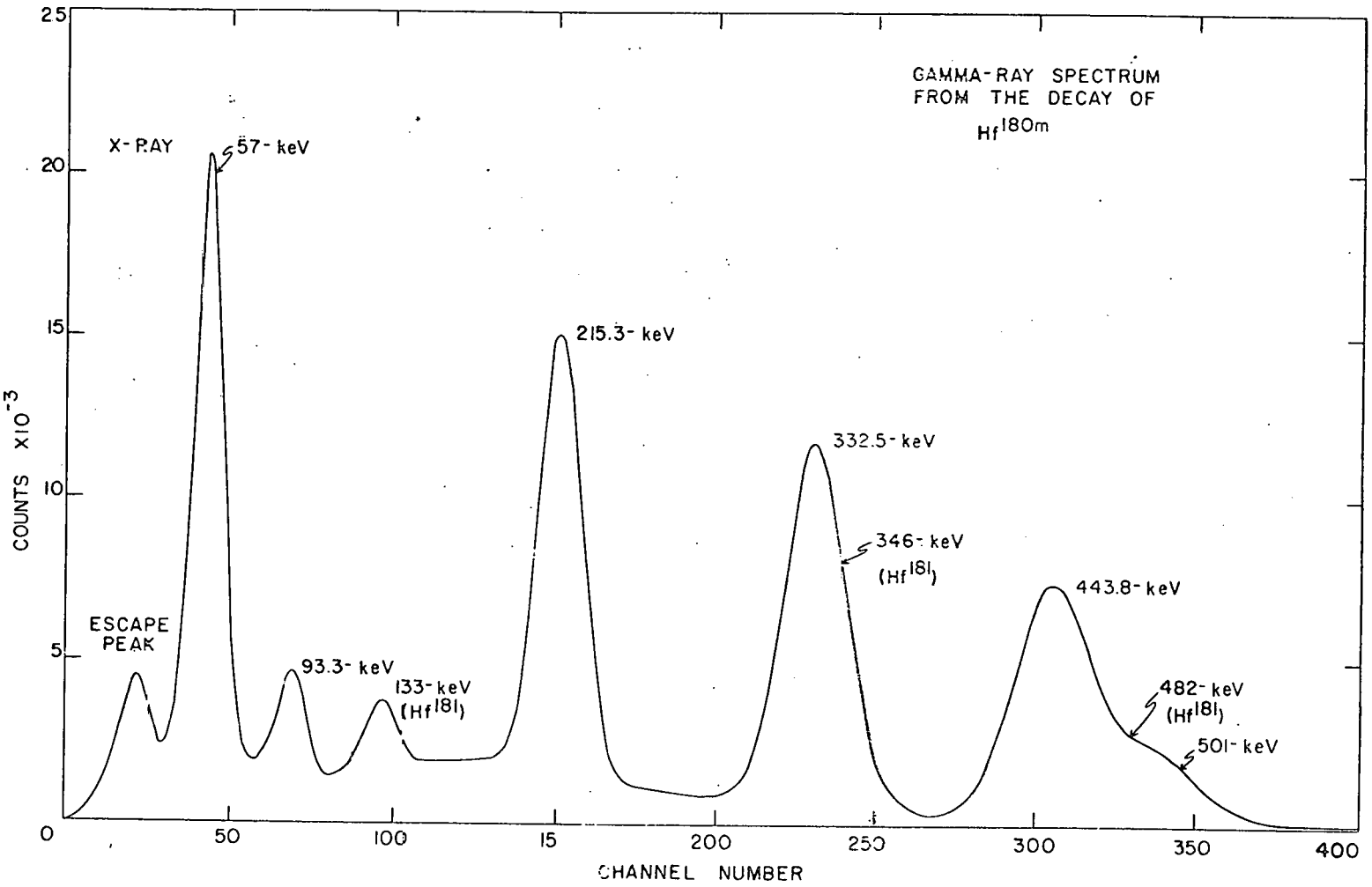

Figure 19. Hf^{180} gamma-ray spectrum taken with a NaI(Tl) detector

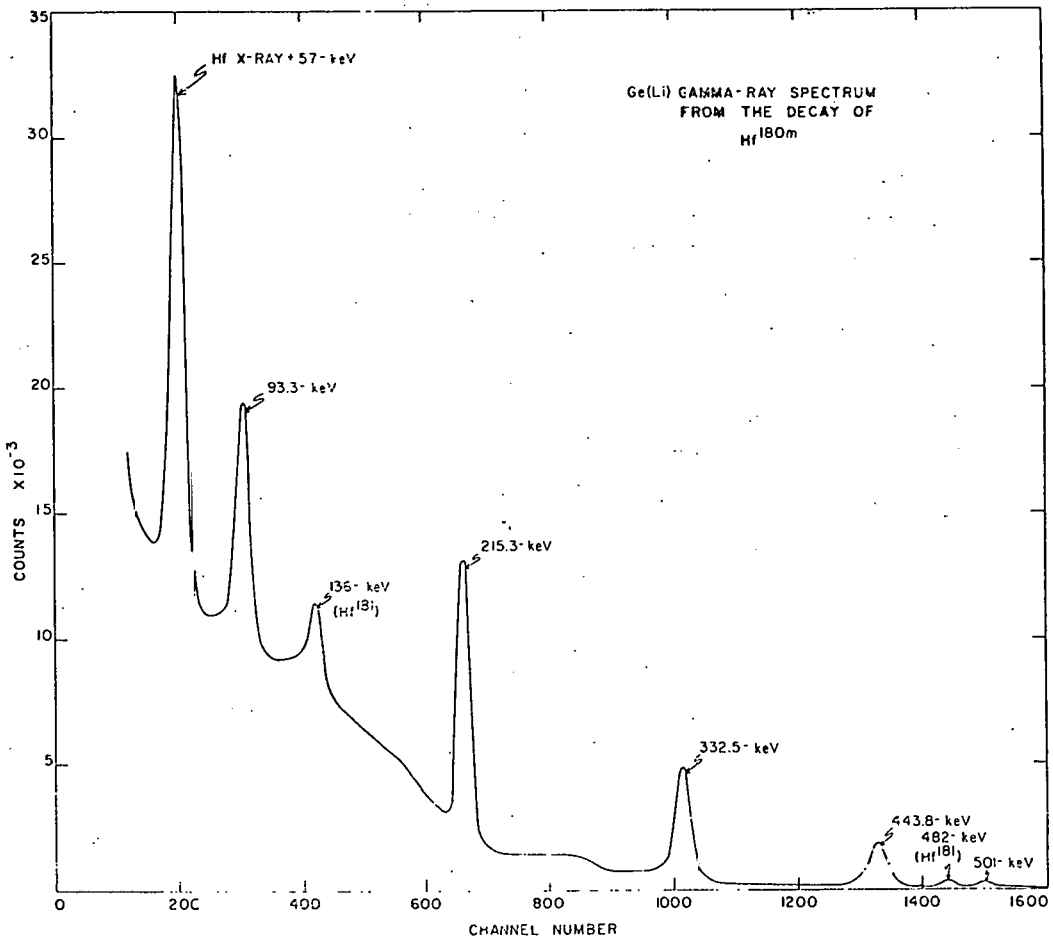

Figure 20. Hf^{180} gamma-ray spectrum taken with a Ge(Li) detector

source. The thin source for the gamma-ray portion was made by depositing approximately 0.6 mg of Hf^{180m} source material on a strip of 0.00025 thick aluminized mylar over an area of 0.2 cm x 3 cm. The thin source for the X-ray portion was made in a similar fashion except 0.3 mg of Hf^{180m} was deposited on the mylar. In order to correct for the presence of Hf^{181} in the source material, a Hf^{181} source was prepared from neutron capture of Hf^{180}. This source was allowed to decay for several days to allow any Hf^{180m} to decay out.

The response functions for the 93.3-keV, 215-keV, 333-keV, 444-keV and 501-keV transitions were obtained with the germanium diffraction crystal and are shown in Figure 21. The pulse-height spectrum from the Hf^{181} source was recorded in the same manner as the composite spectrum. This spectrum was then fit to the observed composite spectrum as a response function in the same manner as the monochromatic response functions. Six sets of data were analyzed with the linear least-squares computer program. Figure 22 displays the composite spectrum along with the response functions and the calculated composite spectrum. The bottom curve again shows the deviation of the experimental composite spectrum from the calculated spectrum. The results of the least-squares fitting yielded the relative intensities which are presented in Table 3.

In the X-ray portion of the spectrum, the $K_{\alpha 1}$, $K_{\alpha 2}$, $K_{\beta 1,3}$, $K_{\beta 2}$ X-ray and the 57-keV gamma-ray response functions were obtained with the quartz diffraction crystal while the response functions for the 93.3-keV and 215-keV gamma rays were obtained with the germanium diffraction crystal. As in the other X-ray intensity measurements, response functions for the K_{α} and K_{β} X-rays were obtained by fixing the ratios of the $K_{\alpha 1}$ to $K_{\alpha 2}$ and

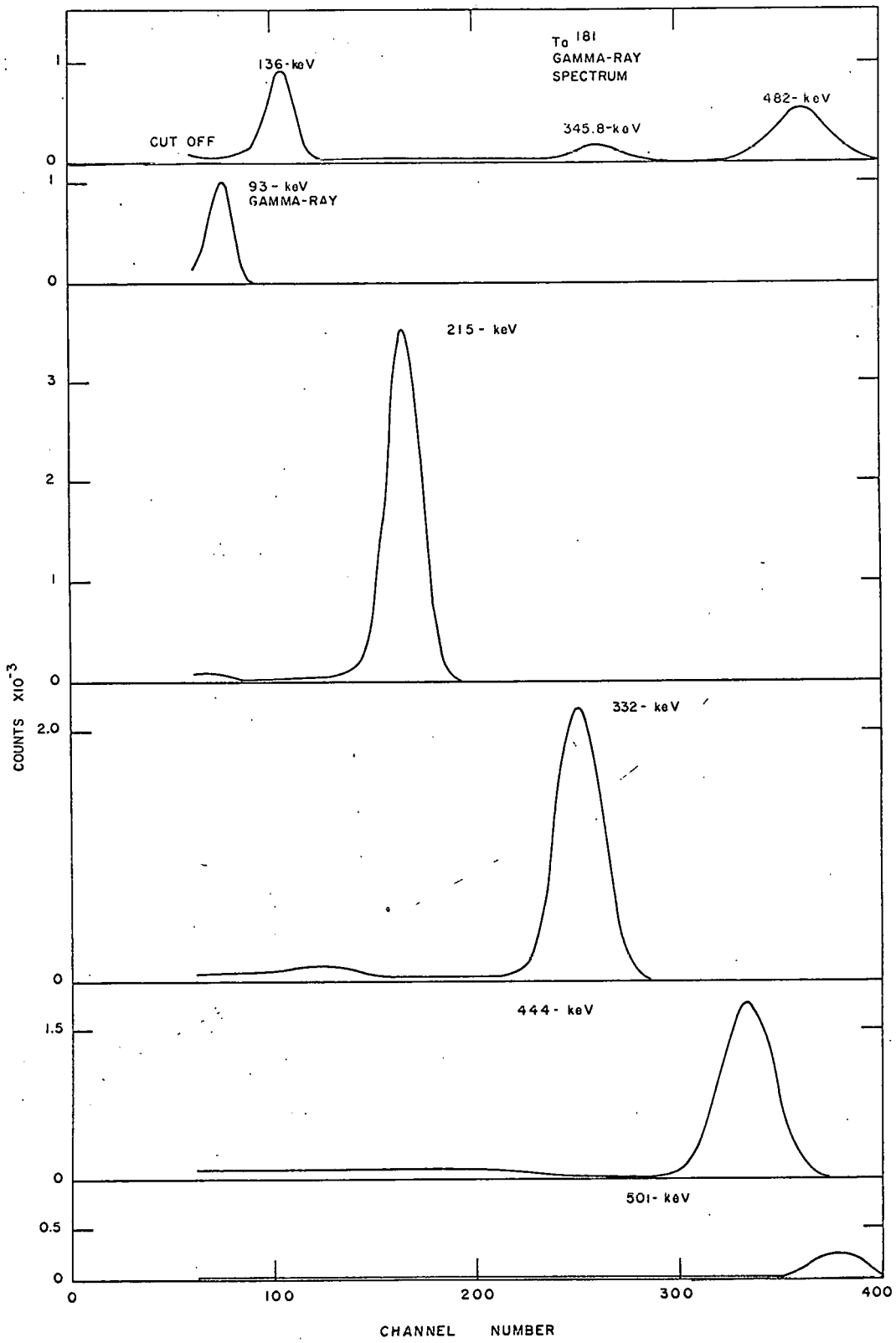

Figure 21. Hf^{180} response functions used in the least-squares fitting procedure from 90-keV to 510-keV.

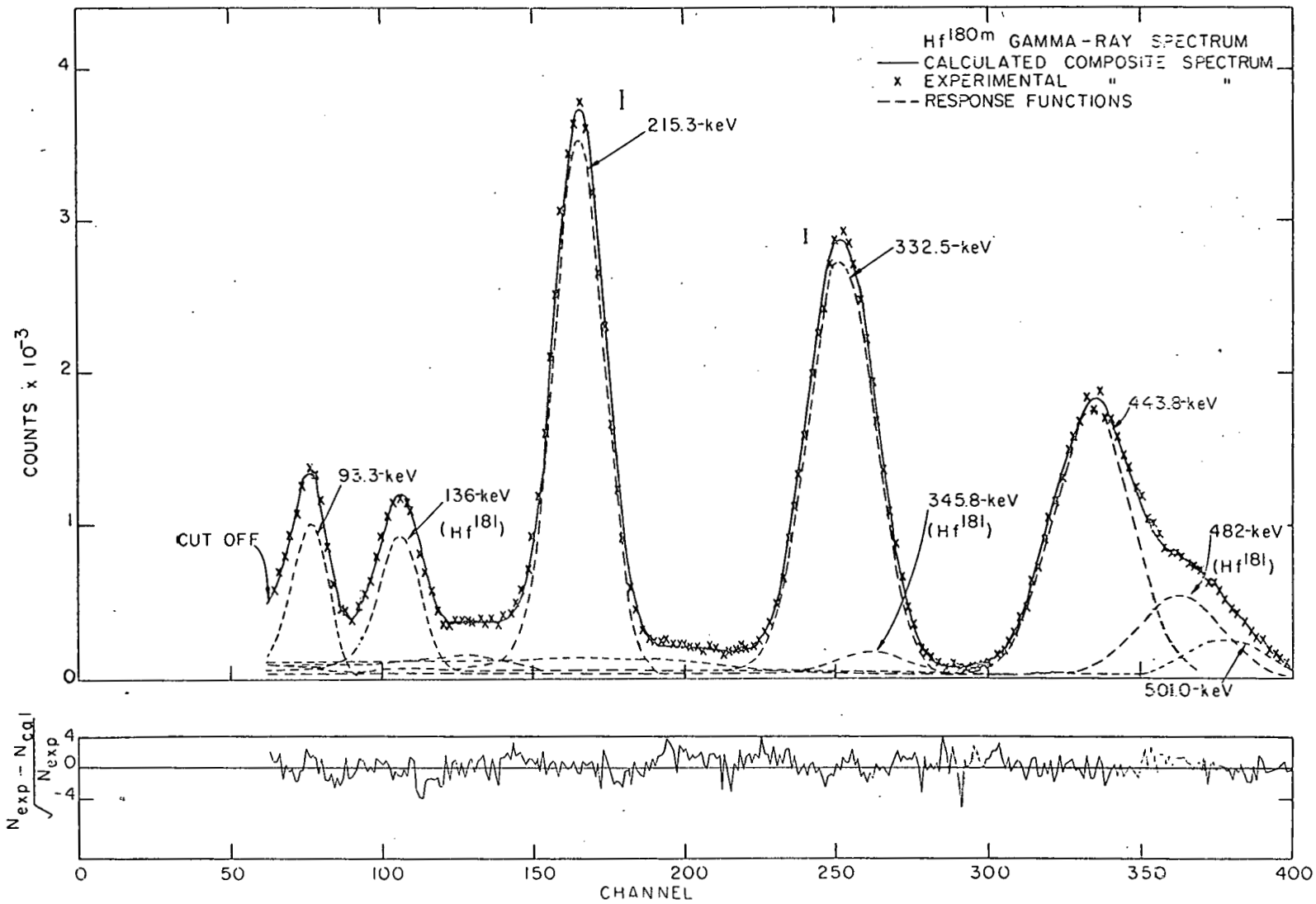

Figure 22. Hf^{180} composite spectrum from 90-keV to 510-keV with computed composite spectrum and monoenergetic components.

Table 3. Relative intensities of the gamma rays above 90-keV from the decay of Hf^{180m}

Energy (keV)	Intensity
501.3	136±12
443.8	904±30
332.5	1000±25
215.3	865±20
93.3	180±5

$K_{\beta 1,3}$ to $K_{\beta 2}$ X-rays at their respective values from the tables of Wapstra et al. (7). These response functions are shown in Figure 23. Figure 24 shows the low energy pulse-height spectrum obtained with the thin source which was enriched to 87 percent in Hf^{179}. It can be seen that the Hf^{181} contribution is considerably reduced over what it was in Figure 19. This enabled the Hf^{180} X-ray and 57-keV gamma-ray intensities to be determined to a higher degree of precision. The contribution from the Compton distribution from the higher energy gamma rays was determined by fixing the ratios of the Compton distributions from the higher energy gamma rays at the values obtained in the previous experiment and by fitting this distribution along with the other response functions. The Hf^{181} spectrum was again used as a response function in the fitting procedure.

Five sets of data were analyzed with the least-squares computer program which is described in Appendix D. Figure 25 shows the composite spectrum

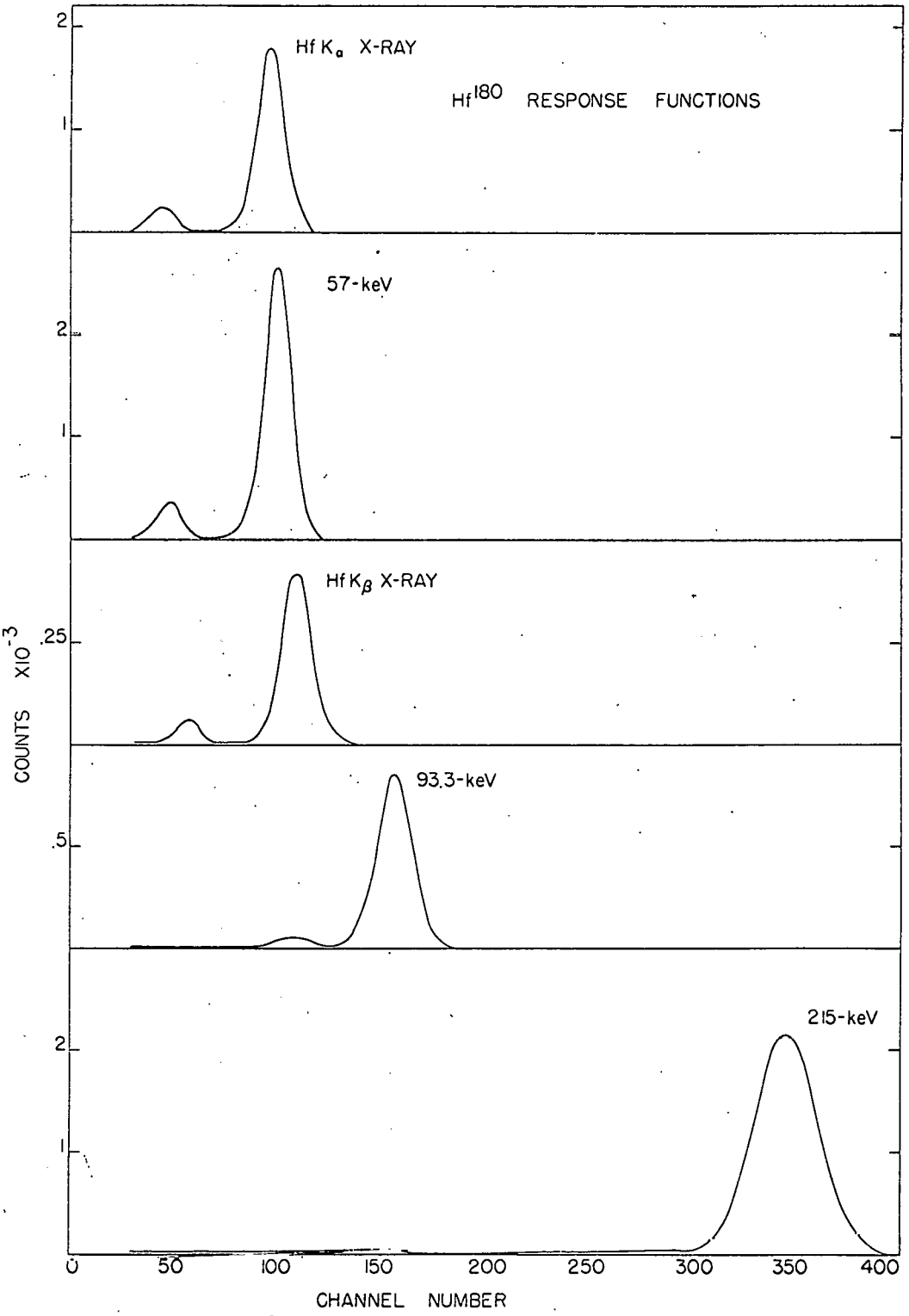

Figure 23. Hf^{180} response functions used in the least-squares fitting procedure below 230-keV.

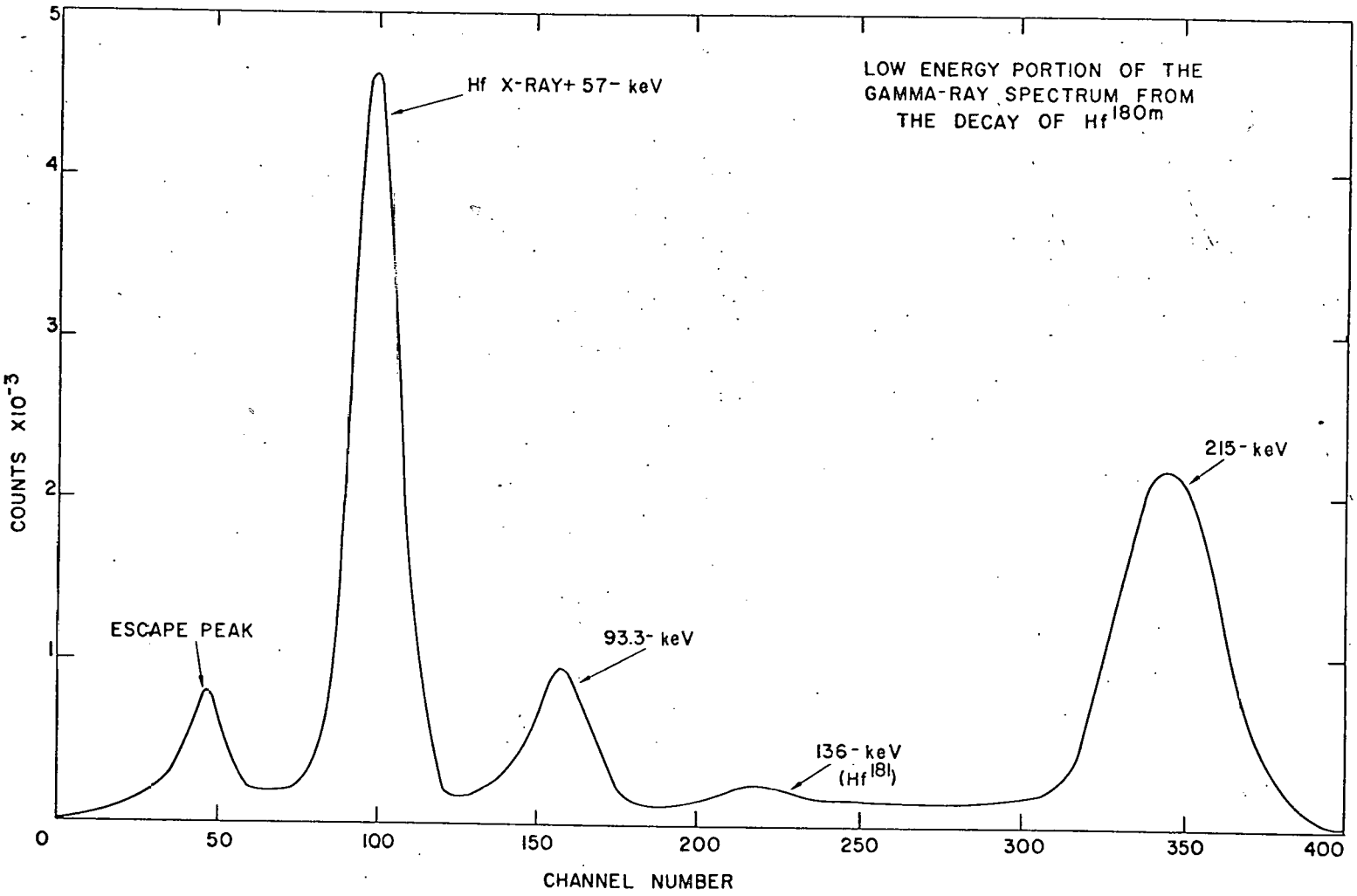

Figure 24. Hf^{180} gamma-ray spectrum below 230-keV

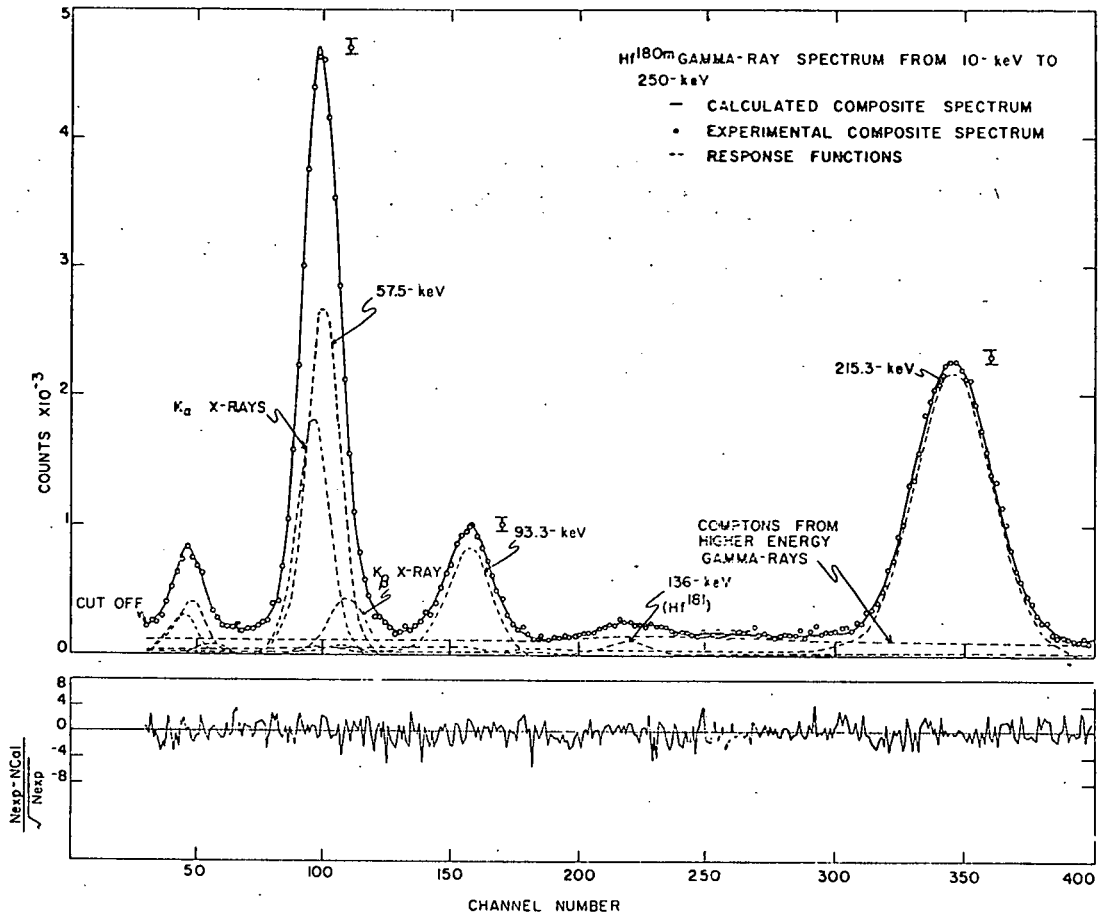

Figure 25. Hf^{180} composite spectrum below 230-keV with computed composite spectrum and monoenergetic components

along with the response functions and the calculated spectrum. The experimental value for the ratio of K_β X-ray to K_α X-rays was 0.254±0.019 and the expected value (7) is 0.263±0.005. The least-squares fitting procedure yielded the values for the intensities which are given in Table 4. The intensities of the 215-keV and 93.3-keV gamma rays were normalized to their values in Table 3, and this normalization constant was used to determine the relative intensities of the K_β and K_α X-rays and the 57-keV gamma ray with respect to the higher energy gamma rays. The X-ray and gamma-ray relative intensities, normalized such that the 215-keV gamma ray has an intensity of 1000, are presented in Table 5 along with the values of Edwards and Boehm (57) which were obtained by the crystal-diffraction method. For comparison, the ratios of the values obtained by Edwards and Boehm (57) to the present values are given in the fourth column of Table 5. The agreement is within five percent except for the 501.3-keV transition. The present determination for this transition was a direct measurement while that of Edwards and Boehm (57) was inferred from the Hf^{180m} decay scheme and from their other intensity measurements. The present value of 1.25±0.08 for the ratio of the 57-keV gamma ray to the K X-rays is in agreement with the value of 1.6±0.5 obtained from critical absorption by Deutsch and Bauer (58).

The power of the present method for determining gamma-ray relative intensities is demonstrated by the unfolding of the 57-keV gamma ray from the K_α and K_β X-rays. This was only possible because the intensity of the 57-keV gamma ray was approximately the same as the X-ray intensity. Added confidence in the resolving of the one photopeak into the three components, K_α X-rays, 57-keV gamma ray and K_β X-rays, is obtained from the agreement between the experimental and expected ratio of K_β to K_α X-rays.

Table 4. Relative intensities of the gamma rays below 250-keV from the decay of Hf^{180m}

Energy (keV)	Intensity
215.3	1000±23
93.3	209±6
K_β	96±6
57	595±23
K_α	379±17

Table 5. Hf^{180} gamma-ray relative intensities following the decay of Hf^{180m}

Energy (keV)	Present results	Edwards and Boehm[a]	Edwards and Boehm[a] / Present results
501.3	136±12	180±55	1.324
443.8	904±30	866±46	0.958
332.5	1000±25	1000±42	1.000
215.3	865±20	882±25	1.020
93.3	180±5	176±4	0.978
K_β	83±5		
57	513±20	513±17	1.000
K_α	327±15		

[a]Source: (57).

2. Results and discussion

Following is a description of how the present values for the Hf^{180} internal conversion coefficients were obtained. Because the final three transitions are in cascade with no crossover transitions, the total transition intensities for these transitions are equal. Thus we can write

$$I_\gamma^{332} (1 + \alpha_T^{332}) = I_\gamma^{93} (1 + \alpha_T^{93}) .$$

Therefore,

$$\alpha_T^{93} = \frac{I_\gamma^{332}}{I_\gamma^{93}} (1 + \alpha_T^{332}) - 1 ,$$

where I_γ^{332} represents the gamma-ray intensity of the 332.5-keV transition and α_T^{332} the total internal conversion coefficient for the same transition. The notation is similar for the corresponding quantities for the 93.3-keV transition. Since α_T^{332} has a value of about 0.060 as discussed later, and $I_\gamma^{332} / I_\gamma^{93}$ is large, any uncertainty in α_T^{332} has only a small effect in determining α_T^{93}. For example, an uncertainty of 10 percent in α_T^{332} would lead to an uncertainty of 0.7 percent in computing α_T^{93}. The latter coefficient is determined mainly by the ratio of I_γ^{332} to I_γ^{93}. Therefore, α_T^{93} can be determined from measurements of the gamma-ray relative intensities compared with I_γ^{332}, along with a correction for α_T^{332}, which is relatively small. The value determined by Edwards and Boehm (57) of 0.060±0.004 was used for α_T^{332}. Since the error in this value is only 6.5 percent, it contributes an uncertainty of 0.5 percent, to the present determination of α_T^{93}. Thus α_T^{93} = 4.91±0.23 was obtained. The same procedure was not used to determine α_T^{215} since $I_\gamma^{332}/I_\gamma^{215}$ is near one, and any uncertainty in the value

of α_T^{332} has a large effect in determining α_T^{215}. Once α_T^{93} has been determined, the corresponding internal conversion coefficients for the atomic shells can be obtained from K:L:M+N... ratios obtained by Edwards and Boehm (57). The remainder of the internal conversion coefficients for the 57-, 215.3-, 332.5-, 443.8- and 501.3-keV transitions were determined by taking the ratios of the internal conversion electron intensities of Edwards and Boehm (57) to the present values of the gamma-ray relative intensities. These ratios were then normalized using the value of α_T^{93} which was obtained from the present gamma-ray relative intensity measurements. Thus, the present conversion coefficients depend on the conversion line relative intensities of Edwards and Boehm (57) but have been computed using new measurements of the gamma-ray relative intensities and an independently obtained normalization constant. The conversion coefficients obtained in this manner (59) are presented in Figure 26 along with the coefficients obtained by Edwards and Boehm (57), Gvozdev et al. (60) and Scharff-Goldhaber and McKeown (61). The theoretical values obtained by interpolating values from the tables of Sliv and Band (2) are presented in the last column of the table. The theoretical values of Rose (1) are in good agreement with those of Sliv and Band (2). The large errors in the values of Gvozdev et al. (60) are probably due to the thick sources which were used due to the fact that they used natural Hf instead of enriched Hf. Since the present gamma-ray relative intensities agree with those of Edwards and Boehm (57), it is not surprising that the present internal conversion coefficients also agree closely.

In Figure 27 are displayed the ratios of the present determinations to the theoretical values of Sliv and Band (2) for the K-shell conversion coefficients of the Hf^{180} E2 transitions. The errors were obtained by

Energy (keV)	Conversion line	Conversion electron intensities (Edwards and Boehm)[a]	Edwards and Boehm[a]	Present results	Conversion coefficients Gvozdev and Rusinov[b]	Scharff-Goldhaber and McKeown[c]	Theoretical[d]	
						L_I 0.303±0.025	E1	M2
57.5	L_I+L_{II}	0.248±0.014	0.458±0.036	0.456±0.040			0.163	69
						L_{II} 0.067±0.010		
	L_{III}	0.045±0.006	0.084±0.012	0.082±0.014		0.055±0.010	0.062	22
	L_{Total}	0.294±0.012	0.543±0.036	0.541±0.040	0.33±0.10		0.225	91
	Total	0.378±0.013	0.698±0.045	0.696±0.048				
								E2
93.3	K	0.205±0.012	1.10±0.09	1.05±0.09	1.3±0.4			1.06
	L_{Total}	0.582±0.017	3.13±0.19	2.99±0.22				2.75
	M+N+...	0.169±0.012	0.909±0.08	0.868±0.08				
	Total	0.956±0.023	5.14±0.24	4.91±0.23[e]				
								E2
215.3	K	0.114±0.005	0.123±0.009	0.122±0.009	0.15±0.05			0.137
	L_{Total}	0.072±0.006	0.077±0.007	0.077±0.008				0.070
	Total	0.221±0.010	0.237±0.017	0.236±0.018				
								E2
332.5	K	0.0400±0.0016	0.038±0.003	0.037±0.003	0.055±0.014			0.042
	L_{Total}	0.0154±0.0012	0.0146±0.0015	0.0142±0.0014				0.0132
	Total	0.0634±0.0025	0.0603±0.004	0.0586±0.0044				
								E2
443.8	K	0.0173±0.0010	0.0189±0.0017	0.0177±0.0016	0.026±0.007			0.020
	L_{Total}	0.0040±0.0005	0.0044±0.0007	0.0041±0.0006	0.0063±0.0016			0.0049
	M+N+...	0.00141±0.00028	0.0015±0.0003	0.0014±0.0003				
	Total	0.0227±0.0012	0.0249±0.0022	0.0232±0.0020				
							M2	E3
501.3	K	0.0070±0.0009	0.0370±0.012	0.048±0.008	0.035±0.014		0.121	0.038
	Total	0.0104±0.0011	0.0549±0.018	0.071±0.011				

[a]Source: (57).
[b]Source: (60).
[c]Source: (61).
[d]Source: (2).
[e]This value was obtained from the present gamma-ray intensities.

Figure 26. Hf^{180} internal conversion coefficients following the decay of Hf^{180m}.

statistically adding the experimental error and a five percent error in the theoretical value. The α_K^{93} agrees closely with the theoretical value, but the previously observed deviation of the experimental from the theoretical values for the 215.3-, 332.5- and 443.8-keV transitions remains. In fact, while this deviation for the coefficients of Edwards and Boehm was 10 percent, the present coefficients are slightly lower and the deviation of the present values from the theoretical values is 11 percent for these three E2 transitions. This deviation is larger than has been recently found in other precise measurements for E2 transitions. Before any statement can be made about the possible theoretical origins of these deviations, such as due to the K electron wave functions overlapping the nucleus, an independent measurement of the conversion electron intensities would be necessary to determine conclusively if these deviations are real. The present experimental α_K for the 501-keV transition agrees closely with the theoretical α_K for an E3 multipolarity and is in agreement with the E3, M2 mixture obtained from an angular correlation experiment by Bodenstedt et al. (62) of 96.5 percent E3 and 3.5 percent M2. Scharff-Goldhaber and McKeown (61) have recently made accurate measurements of the L_I, L_{II} and L_{III} conversion coefficients for the 57-keV transition. They report the L_I and L_{II} coefficients are higher than the theoretical conversion coefficients for an E1 transition while the L_{III} coefficient is in agreement with the theoretical value. They point out that no admixture of M2 can account for this difference. Paul et al. (63) have shown that the difference is not due to parity mixing. Scharff-Goldhaber and McKeown (61) conclude that the anomalously high L_I and L_{II} conversion coefficients are due to penetration effects in this extremely K-forbidden E1 transition.

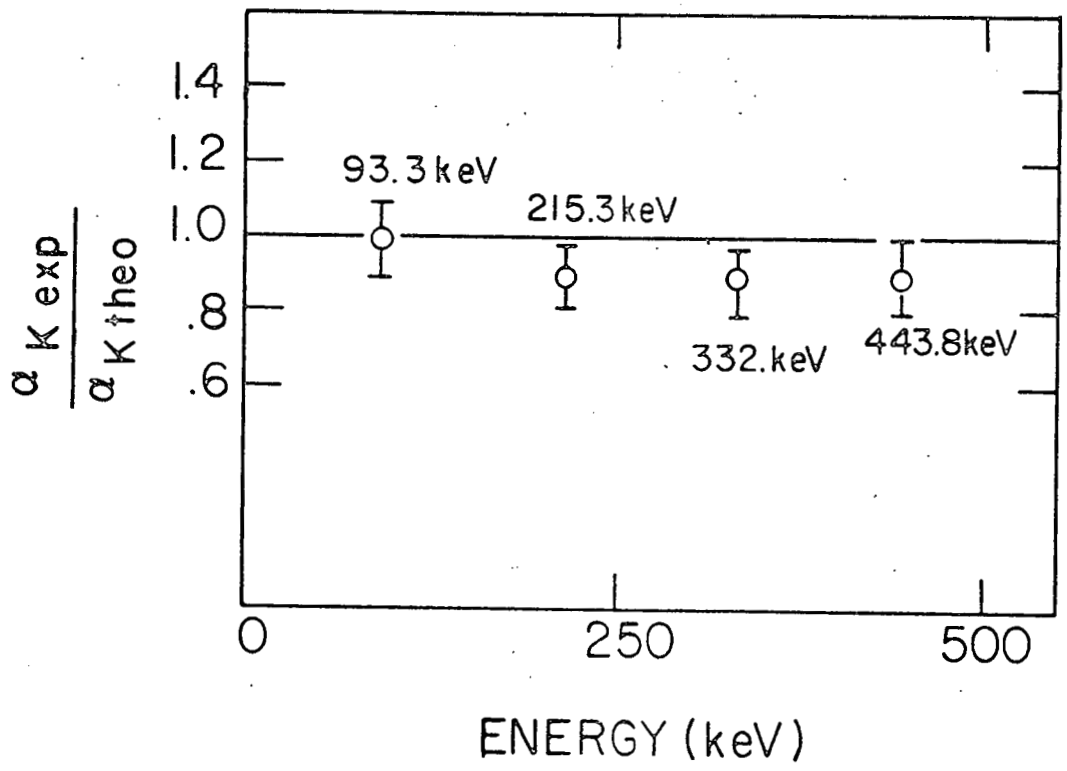

Figure 27. Comparison of the present results for the K conversion coefficients of the E2 transitions in Hf^{180} to the theoretical values of Sliv and Band (2)

C. K Internal Conversion Coefficients in Gd^{155}

The present investigation was carried out to measure accurately the gamma-ray relative intensities of the 105-, 86- and 60-keV gamma rays and the Gd X-rays from the decay of Eu^{155} and to use these accurately determined intensities to determine the K conversion coefficients for the 105- and 86-keV transitions. The level structure exhibited by Gd^{155} following Eu^{155} decay is shown in Figure 28 (32, p. 5-5-52, 1963).

1. Analysis of the Gd^{155} X-ray and gamma-ray spectrum

The line source for the bent-crystal spectrometer was made by double neutron capture of Eu_2O_3 which was enriched to 95 percent in Eu^{153}. A quartz capillary 1 inch long and 0.012 inches inside diameter was filled with 10 mg of enriched Eu_2O_3. The capillary was then irradiated with neutrons in the Materials Testing Reactor at Arco, Idaho, in a neutron flux of 5×10^{14} neutrons/cm^2/sec for 28 days. The thin source for the composite spectrum could not be produced in the same manner because of the large amount of Eu^{154} which would be present in the source material. Instead, Eu^{155} material was purchased from Oak Ridge National Laboratory Isotope Sales Division. This material had been produced by beta decay to Eu^{155} following single neutron capture of Sm^{154}. The source material had been allowed to decay for more than two years to allow the 15.2 day Eu^{156} activity to die out. The Eu^{156} had been produced by beta decay of 9.4 hour Sm^{156} following double neutron capture of Sm^{154} and by single neutron capture of Eu^{155}. The thin source was made by depositing the Eu^{155} material on a strip of aluminized mylar 0.00025 inches thick and 0.2 cm x 3 cm. In Figures 29 and 30 are shown

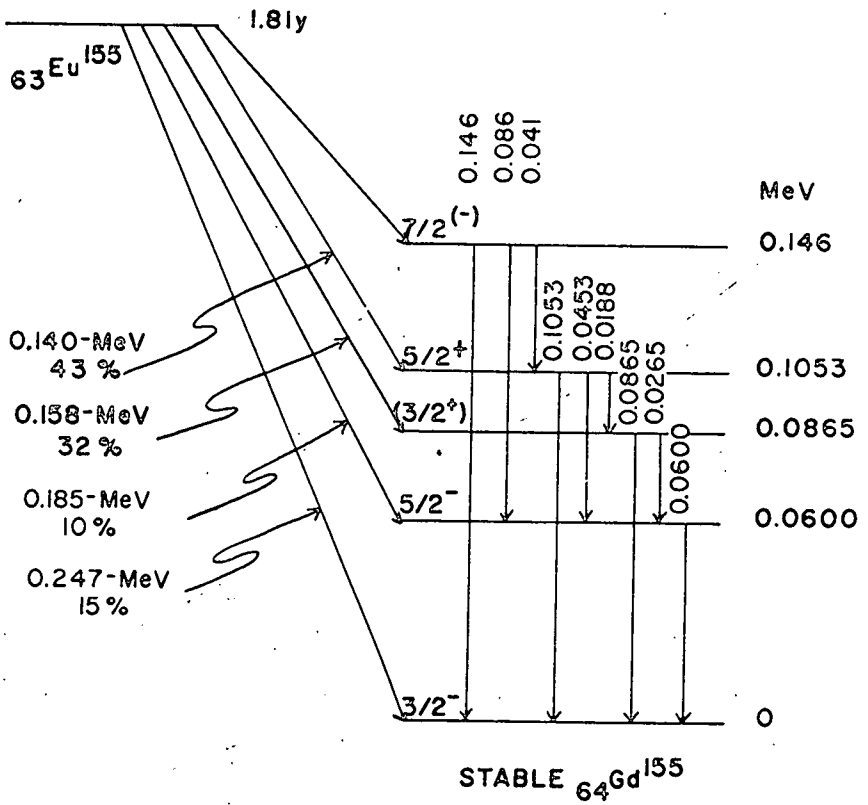

Figure 28. Decay scheme of Eu^{155} (32, p. 5-5-52, 1963)

NaI(Tl) and Ge(Li) spectra from the thin Eu^{155} source. It can be seen in the Ge(Li) spectrum that there is a gamma ray at approximately 123-keV. This gamma ray is due to Eu^{152} and Eu^{154} present in the source material. Since the Eu^{155} source material was purchased in solution from Oak Ridge, it was not possible to determine the amount of material deposited on the strip of mylar. To check the effect of the source thickness, a very thin source was made by evaporating Eu^{155} onto 1.75 mg/cm^2 aluminum. This source was 0.75 inches long and 2 mm wide. The ratios of K X-rays to the 86-keV plus 105-keV gamma rays was determined. The ratio for the evaporated source was 0.52 while that for the drop source was 0.53. From this it was concluded that there was no appreciable effects due to the thickness of the drop source. The evaporated source was not used for the composite spectrum because of the long counting times that would be necessary due to the weak intensity of the source.

It can be seen from Figure 29 that the gamma-ray spectrum mainly consists of the 105-, 86- and 60-keV gamma rays and the Gd X-rays. Weak transitions at 26- and 45-keV are also present. The other transitions which are shown on the decay scheme are extremely weak and can be ignored when the gamma-ray relative intensities are determined. Response functions were measured for the 105-, 86- and 60-keV gamma rays and the $K_{\alpha 1}$, $K_{\alpha 2}$, $K_{\beta 1,3}$ and and $K_{\beta 2}$ X-rays. K_α and K_β response functions were again obtained by fixing the ratios of the $K_{\alpha 1}$ to $K_{\alpha 2}$ and $K_{\beta 1,3}$ to $K_{\beta 2}$ X-rays. Since the 26-keV gamma-ray intensity is small and since the absorption corrections for 26-keV are very large, no attempt was made to determine accurately the relative intensity of the 26-keV gamma rays. However, a response function was included to improve the fit to the experimental data. This response function

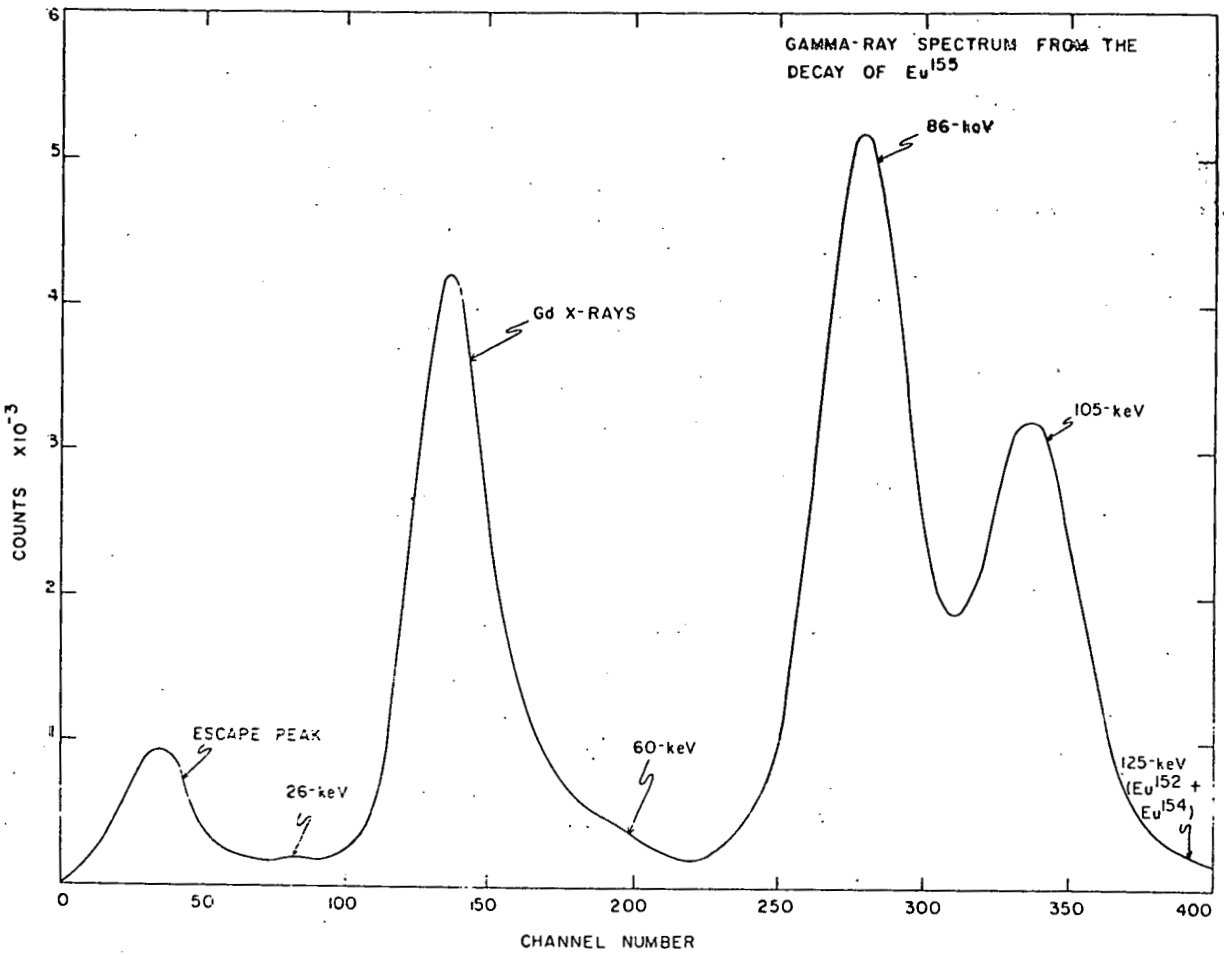

Figure 29. Gd^{155} gamma-ray spectrum taken with a NaI(Tl) detector

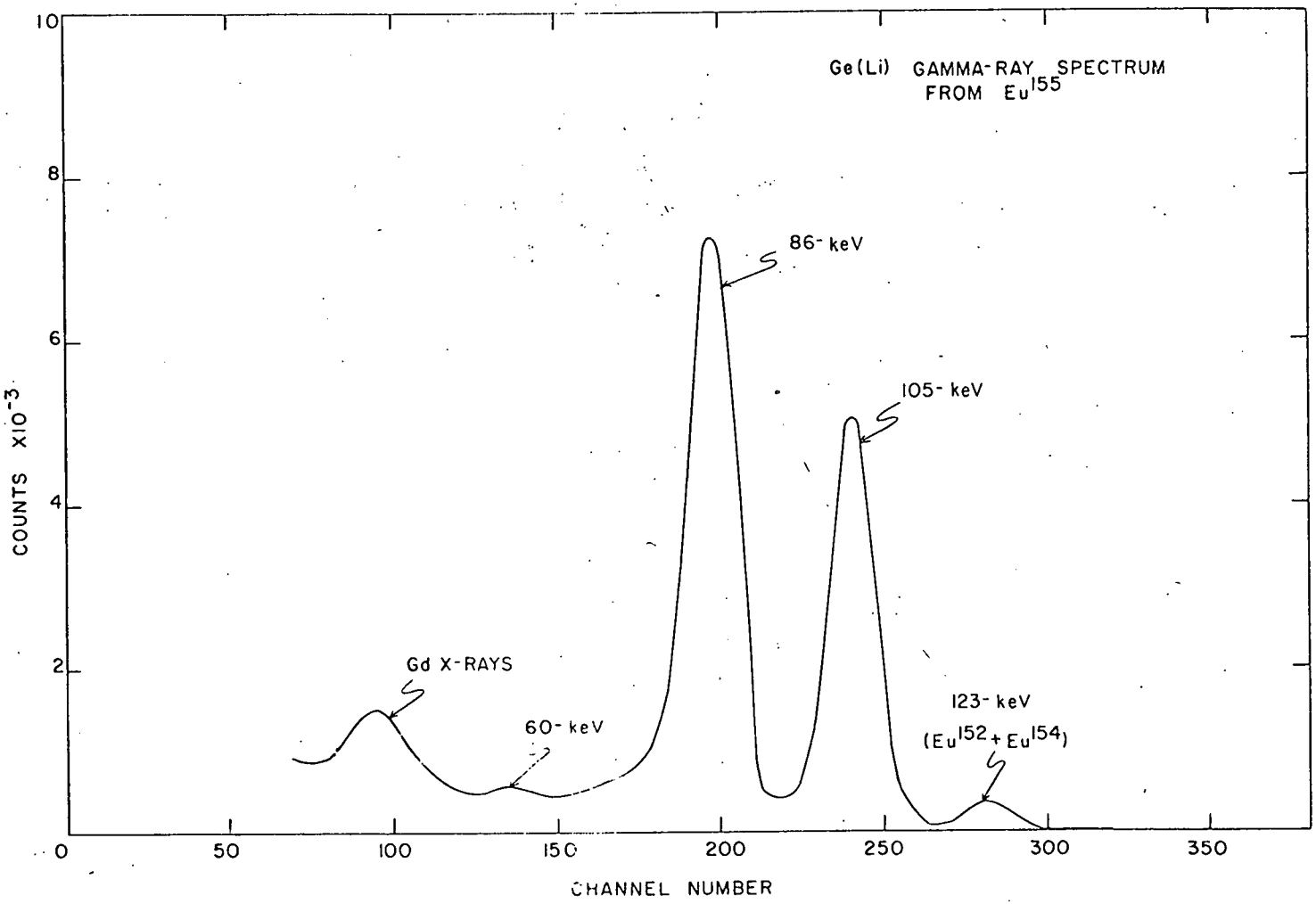

Figure 30. Gd^{155} gamma-ray spectrum taken with a Ge(Li) detector

was obtained from the shape of the photopeak of the $K_{\alpha 1}$ X-ray and from the energy calibration in the X-ray region. The 45-keV gamma ray lies between the K_α and K_β X-rays. No attempt was made to unfold this gamma ray from the X-rays. The X-ray intensity was, however, corrected for the 45-keV gamma rays. Since the gamma rays at 123-keV are the most intense gamma rays in the decay of Eu^{152} and Eu^{154} and since the intensity of the 123-keV gamma rays in the Eu^{155} source was small, no correction was made for the Compton distributions from higher energy gamma rays. A correction was made, however, for the Gd X-rays due to the conversion of the 123-keV transition.

The germanium diffraction crystal was used to obtain the response functions shown in Figure 31. Four sets of data were analyzed with the least-squares computer program. Figure 32 shows one of the fits obtained. The weighted average values are presented in Table 6 along with the previously reported values. The present X-ray intensities have been corrected for the 45-keV gamma rays and the Gd X-rays due to the conversion of the 123-keV transition. The 45-keV intensity was taken from Hatch and Boehm (64). The correction for the Gd X-rays from the conversion of the 123-keV transition was made in the following way. From the relative intensity of the 123-keV gamma ray which was obtained from the least-squares fitting procedure and from the K conversion coefficient for this transition, the number of K X-rays was calculated from $N_X^{123} = \omega_K \alpha_K^{123} I_\gamma^{123}$, where ω_K is the K flourescent yield. The corrections for the Eu^{152} and Eu^{154} X-rays and the 45-keV gamma rays were small and about equal. The ratio of K_β to K_α X-rays was determined to be 0.234±0.012, while the expected value from Wapstra et al. (7) is 0.244±0.007.

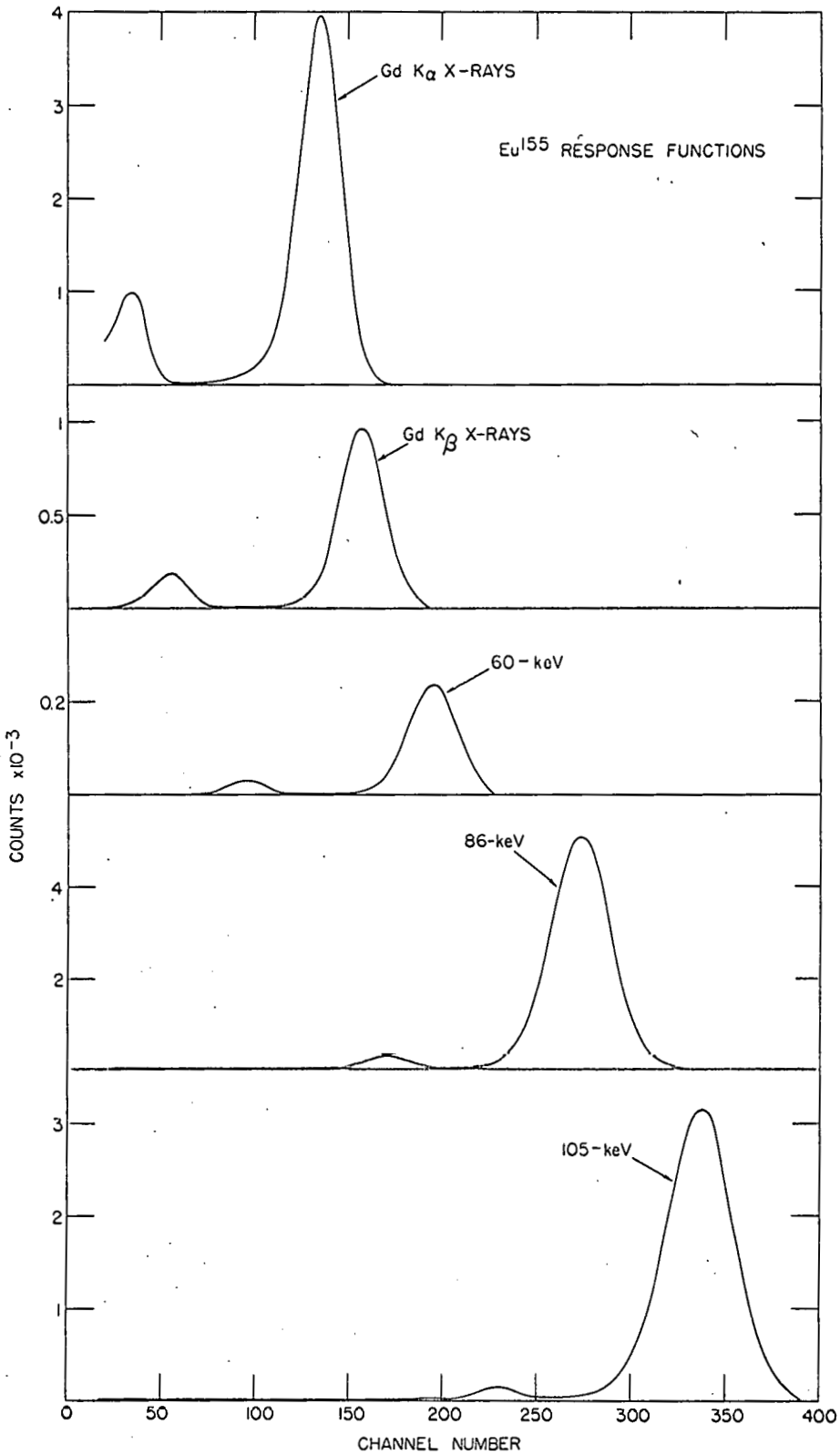

Figure 31. Gd^{155} response functions used in the least-squares fitting procedure.

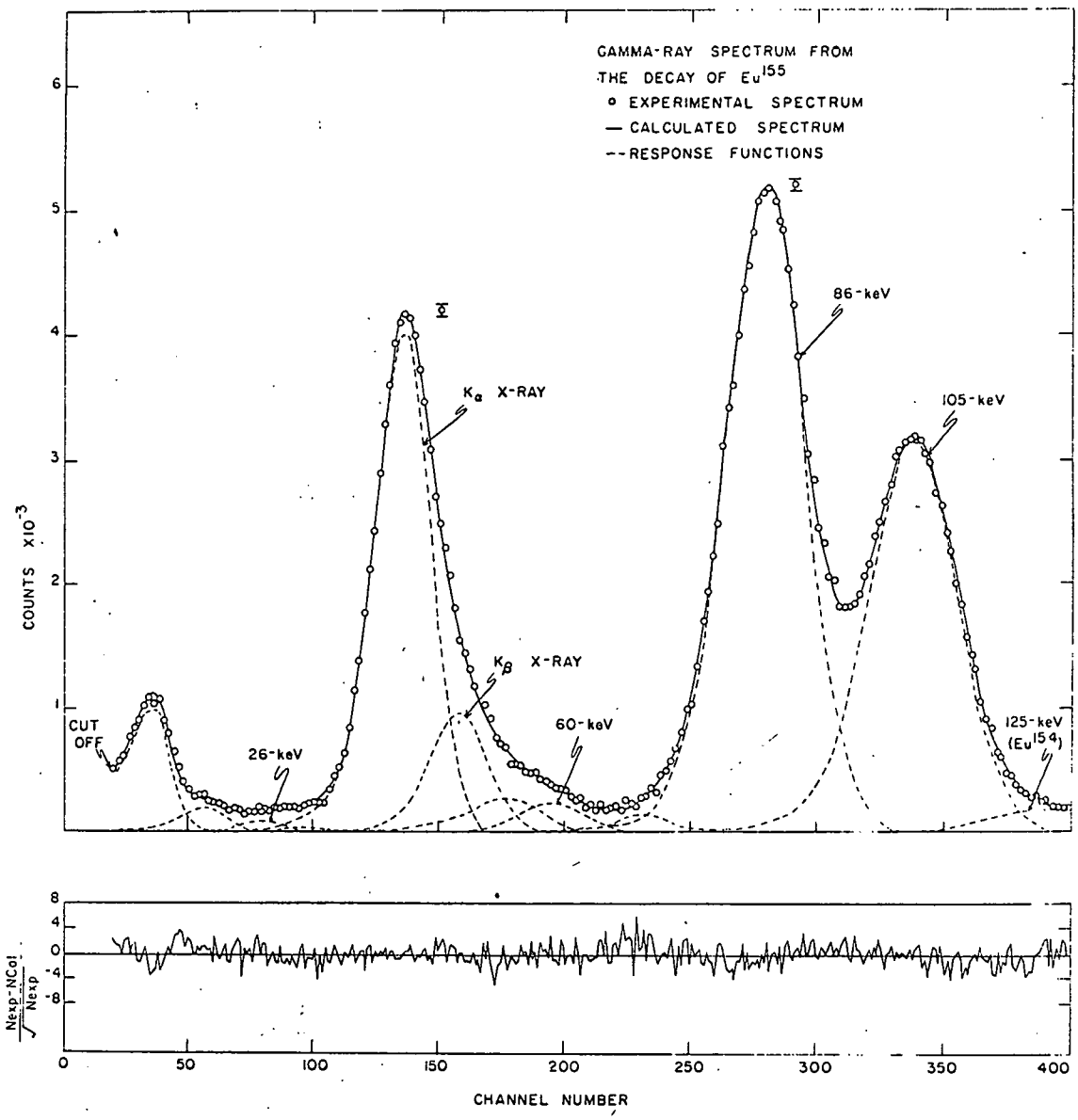

Figure 32. Gd^{155} composite spectrum with computed composite spectrum and monoenergetic components

Table 6. Gd^{155} gamma-ray relative intensities following the decay of Eu^{155}

Energy (keV)	Present results	Subba Rao[a]	Hatch and Boehm[b]	Vergnes[c]
		58.5±6		
105	68.3±2.7	68.5±5	64	65
86	100±3	100	100	100
60	4.3±0.3	5.0±0.6	4	
K_β	15.3±0.6	97.5±0.3		
K_α	65.6±2.2			

[a]Source: (65).

[b]Source: (64).

[c]Source: (66).

2. Results and discussion

The present values for the gamma-ray intensities are in agreement, within the experimental errors, with all of the previously reported values except the lower of the two values reported by Subba Rao. The X-ray relative intensity presented here is 16 percent lower than the value reported by Subba Rao (65). Recently Subba Rao (4) has reanalyzed his data and has reported readjusted values for the conversion coefficients. The magnitude of the change would correspond to a change in his X-ray intensity which would bring it into good agreement with the present value.

The K internal conversion coefficients for the 86-keV and 105-keV transitions were determined in the following way. Since the energies of the

26-keV and 45-keV gamma rays are too low for K conversion, the K X-rays are due predominantly to the 60-, 86- and 105-keV transitions

$$N_X = N_X^{60} + N_X^{86} + N_X^{105} \qquad \text{Equation 11}$$

where N_X is the total number of K X-rays and N_X^{60}, N_X^{86} and N_X^{105} are the number of K X-rays due to 60-, 86- and 105-keV transitions respectively. The number of K X-rays from the 60-keV transition can be determined from

$$N_X^{60} = \alpha_K^{60} \omega_K I_\gamma^{60} \qquad \text{Equation 12}$$

where ω_K is the fluorescent yield, I_γ^{60} is the relative intensity of the 60-keV gamma ray and α_K^{60} is the K internal conversion coefficient for the 60-keV transition. The α_K^{60} can be obtained from the mixing ratio of 5/95 which has been determined from the Tb decay (67) and the theoretical conversion coefficients of Rose (1). Using these values, α_K^{60} is 6.89. Substituting this value into Equation 12 along with the fluorescent yield and the intensity of the 60-keV gamma ray from Table 7, the number of X-rays due to the 60-keV transition was determined to be 27.3±3.3. Using this value in Equation 11, the number of X-rays from the 86- and 105-keV transitions was determined. The number of K conversion electrons for each of these transitions was then determined from

$$e_K^{86} + e_K^{105} = \frac{N_X^{86} + N_X^{105}}{\omega_K}$$

and the ratio of e_K^{86}/e_K^{105} obtained from Subba Rao (65). Using these electron intensities and the gamma-ray relative intensities from Table 6, the K conversion coefficients for the 86- and 105-keV transitions were determined and are presented in Table 7 along with the values of Subba Rao (65) and the

Table 7. Gd^{155}K internal conversion coefficients following the decay of Eu^{155}

Energy (keV)	Present results	Subba Rao[a]	Subba Rao[b]	Theoretical[c] E1	M2
105	0.23±0.03	0.29±0.054	0.23±0.03	0.21	11
86	0.43±0.06	0.49±0.075	0.35±0.04	0.37	26

[a]Source: (65).

[b]Source: (4).

[c]Source: (2).

theoretical values of Sliv and Band (2). The values in column 4 were reported to be from a re-analysis of the data reported in (65). It can be seen that the present value and the revised value of Subba Rao are in good agreement with the theoretical values for pure E1 transitions.

D. Relative Intensities of the 104-, 142- and 246-keV Gamma Rays in Eu^{155}

The relative intensities of the 104-, 142- and 246-keV gamma rays from the decay of 22 minute Sm^{155} have been reported with values differing by 45 percent and with errors of 10 percent or more (68-73). The present investigation was undertaken to determine accurately the relative intensity of these gamma rays so they may be used to obtain the internal conversion coefficients for these transitions.

1. Analysis of the Eu^{155} gamma-ray spectrum

The level structure in the nucleus Eu^{155} following the decay of Sm^{155} is shown in Figure 33 (32, p. 5-5-51, 1963). The Sm^{155} beta decays to Eu^{155} with a half-life of 22 minutes and the Eu^{155} in turn beta decays to Gd^{155} with a half-life of 1.81 years. In Figure 34 is shown a NaI(Tl) pulse-height spectrum from the decay of Sm^{155}.

Because of the short half-life of Sm^{155}, it was not possible to irradiate the Sm^{154} and load it into the source holder manually as had previously been done. The procedure used instead was to use the rabbit system described in section III. The line source for the bent-crystal spectrometer consisted of 22 mg of Sm_2O_3, enriched to 99.2 percent in Sm^{154}, in a quartz capillary 1 inch long and 0.018 inches inside diameter. The quartz capillary was placed in the V groove of the nose cone of the beryllium rabbit which is shown in Figure 7. The rabbit was then inserted into the pneumatic tube and sent into the reactor. The sample was irradiated for 20 minutes in a neutron flux of 9×10^{12} neutrons/cm^2/sec. At the end of the twenty minute irradiation the rabbit was automatically brought down into the transfer system and on into the source position of the spectrometer as described in section III. The time from withdrawal of the rabbit from the reactor to the beginning of the recording of the response functions was approximately 12 seconds. The (400) planes of germanium were used to diffract the gamma rays. Background was recorded before and after the recording of the response function. After the response function for the 246-keV gamma ray was measured, the rabbit was sent back into the reactor for another 20 minutes of irradiation. The 142-keV gamma-ray response function was then recorded in

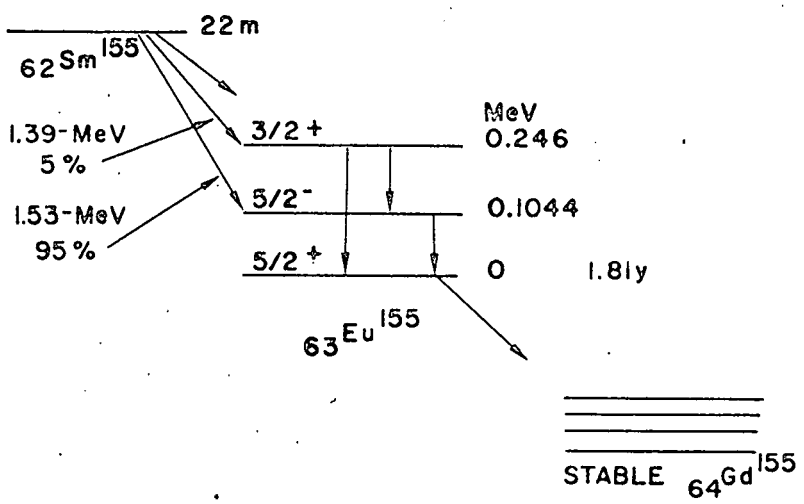

Figure 33. Decay scheme of Sm^{155} (32, p. 5-5-51, 1963)

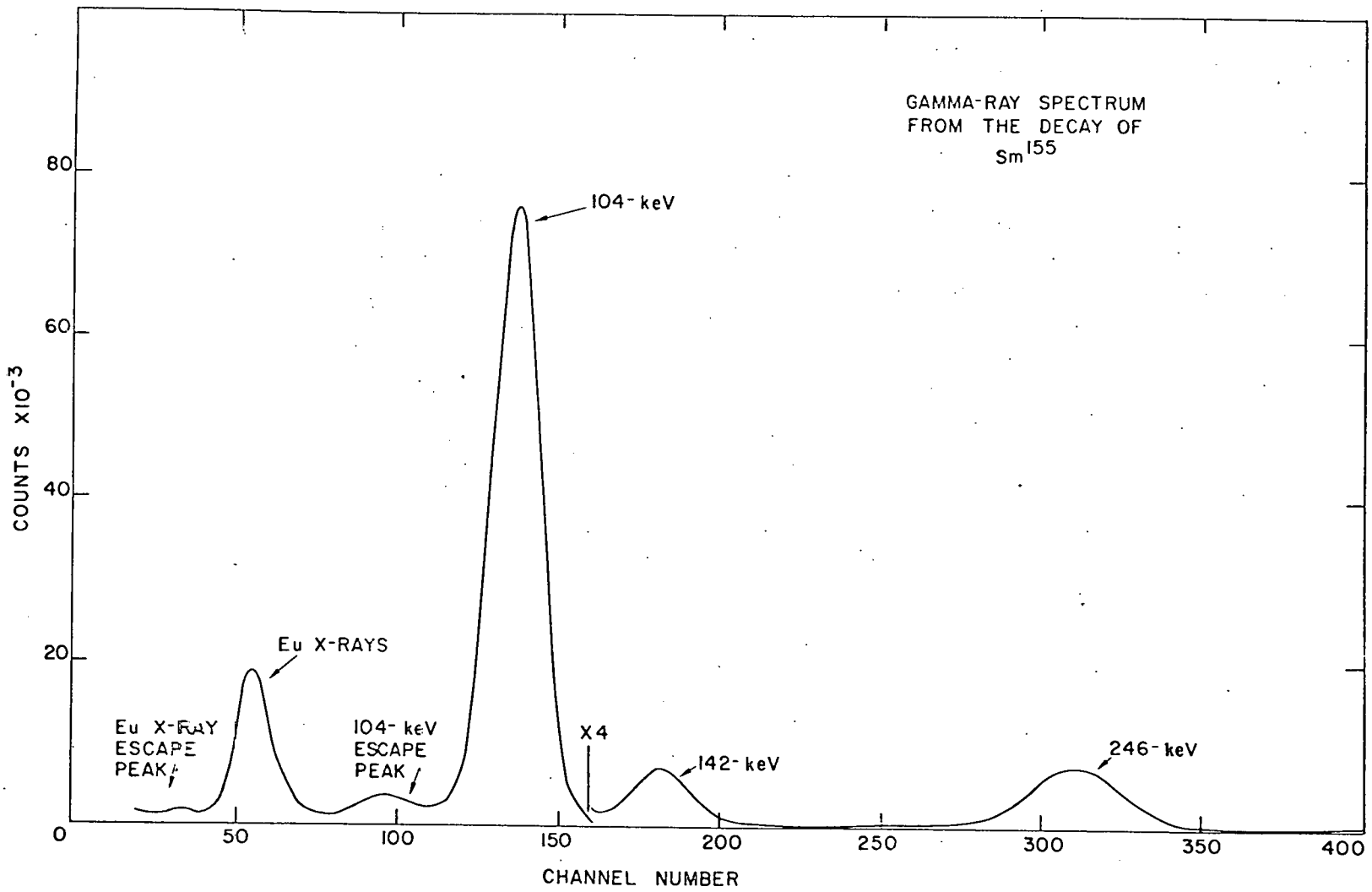

Figure 34. Eu^{155} gamma-ray spectrum

the same manner as the 146-keV gamma ray. Immediately after the 142-keV response function was measured, the 104-keV response function was measured. The thin source for the composite pulse-height spectrum was made by irradiating 0.1 mg enriched Sm in solution for 20 minutes in a neutron flux of 4×10^{13} neutrons/cm^2/sec. This source material was then deposited on a strip of aluminized mylar 0.00025 inches thick and 0.2 cm x 3 cm. Background for this source was recorded before and after the measurement of the composite spectrum. Because of the half-life of the source, no attempt was made to determine the relative intensities of the X-rays. Because of the difference in half lives of the Eu^{155} and Sm^{155} there was an extremely small amount of Eu^{155} in the source. By allowing the 22 minute Sm^{155} to decay away, it was found that there was a small amount of 47 hour Sm^{153} present in the source material. As can be seen in Figure 35 the gamma-ray spectrum from the decay of Sm^{153} mainly consists of a 103-keV transition. This gamma ray required a small correction to the intensity of the 104-keV gamma-ray when the Sm^{155} data was taken immediately after irradiation.

2. Results and discussion

Figure 36 shows the three response functions used in the fitting procedure. Because of the poor statistics of the 142- and 246-keV gamma rays, seven sets of data were analyzed. In Figure 37 is displayed one of the fits obtained. The points are the experimental spectrum, and the smooth curve is the calculated spectrum. The dashed curves are the response functions which add up to the calculated spectrum. In this case only the low energy tails of the response functions can be distinguished from the experimental data and the calculated spectrum. The bottom curve is again the deviation

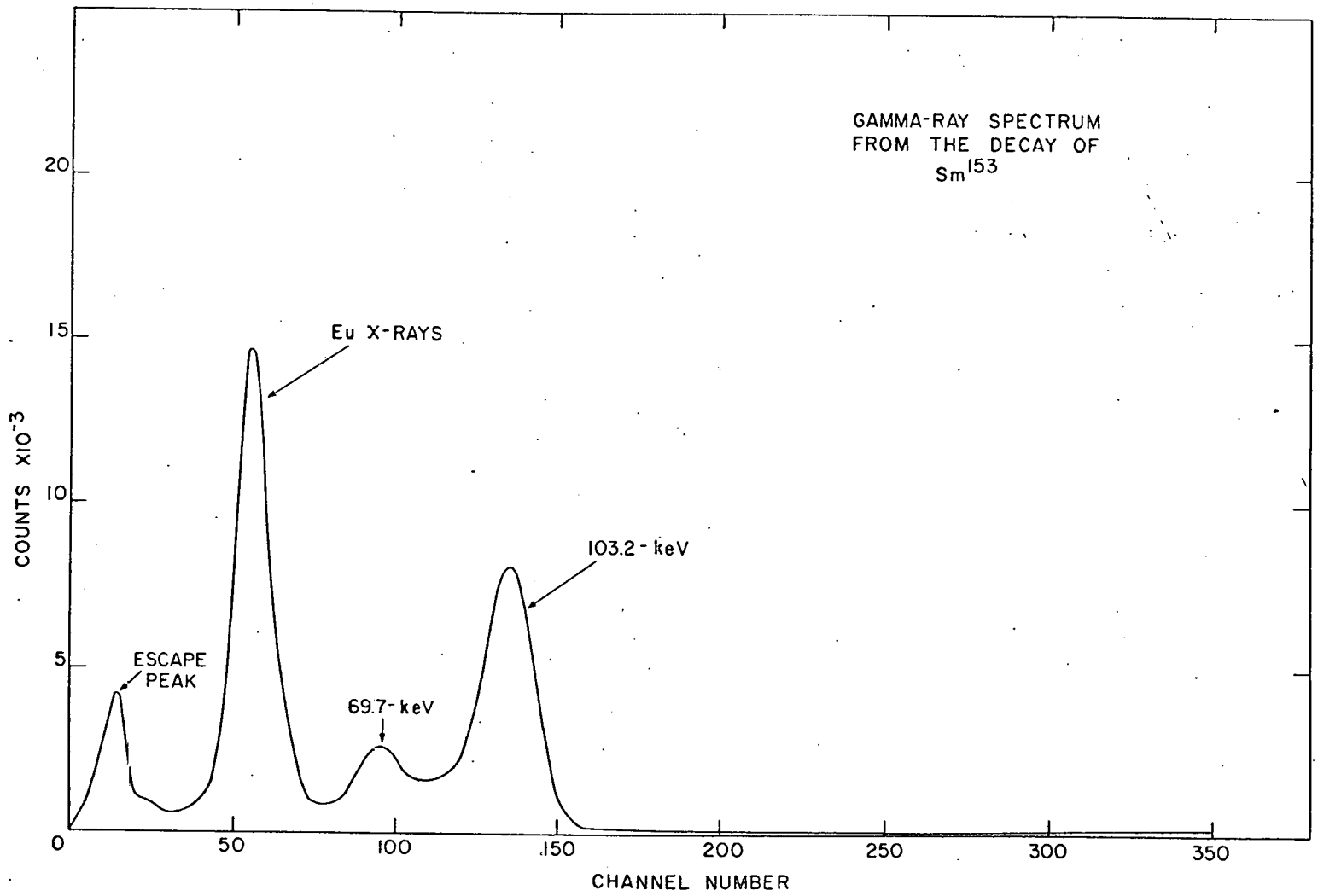

Figure 35. Eu^{153} gamma-ray spectrum

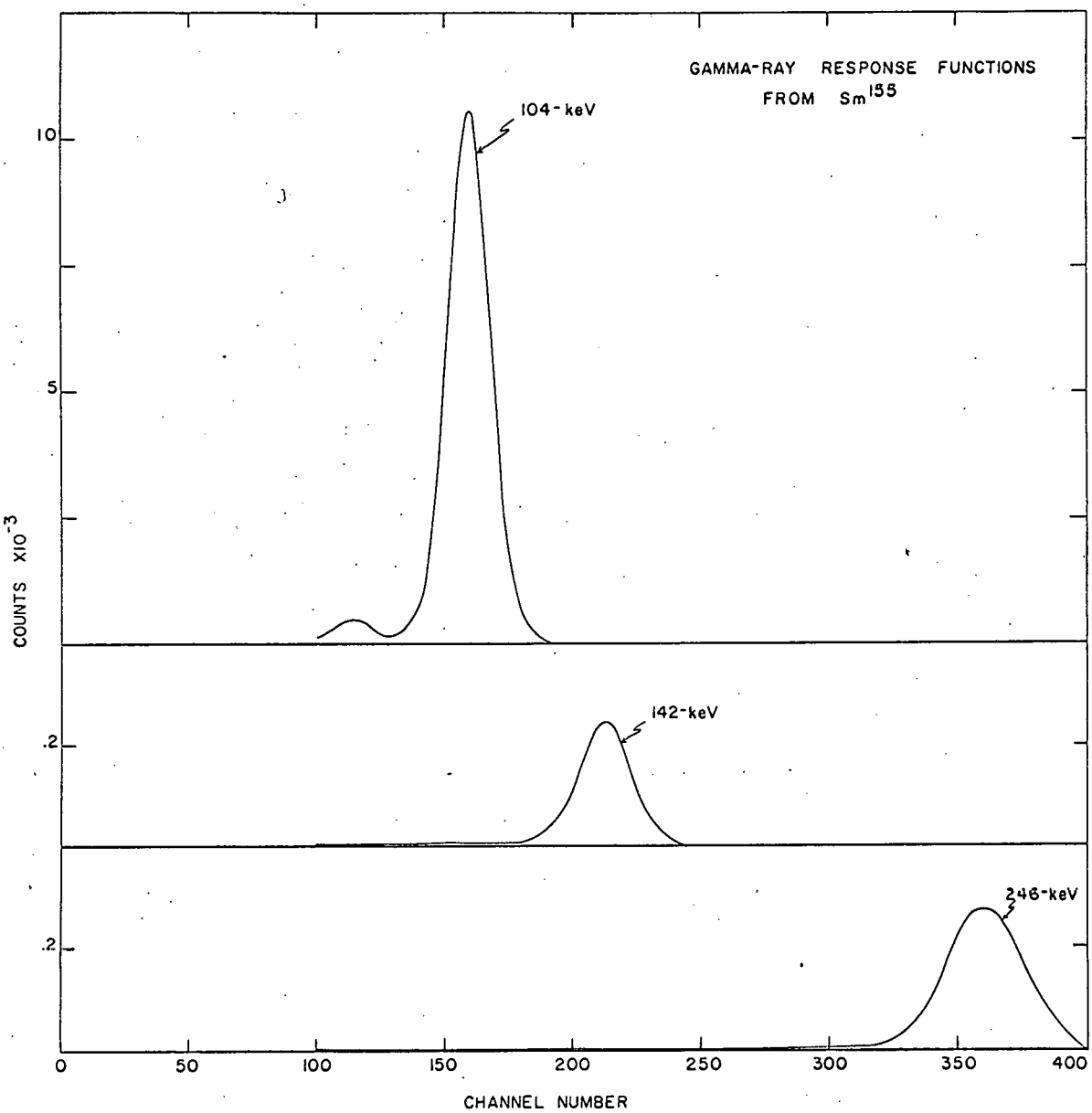

Figure 36. Eu^{155} response functions used in the least-squares fitting procedure

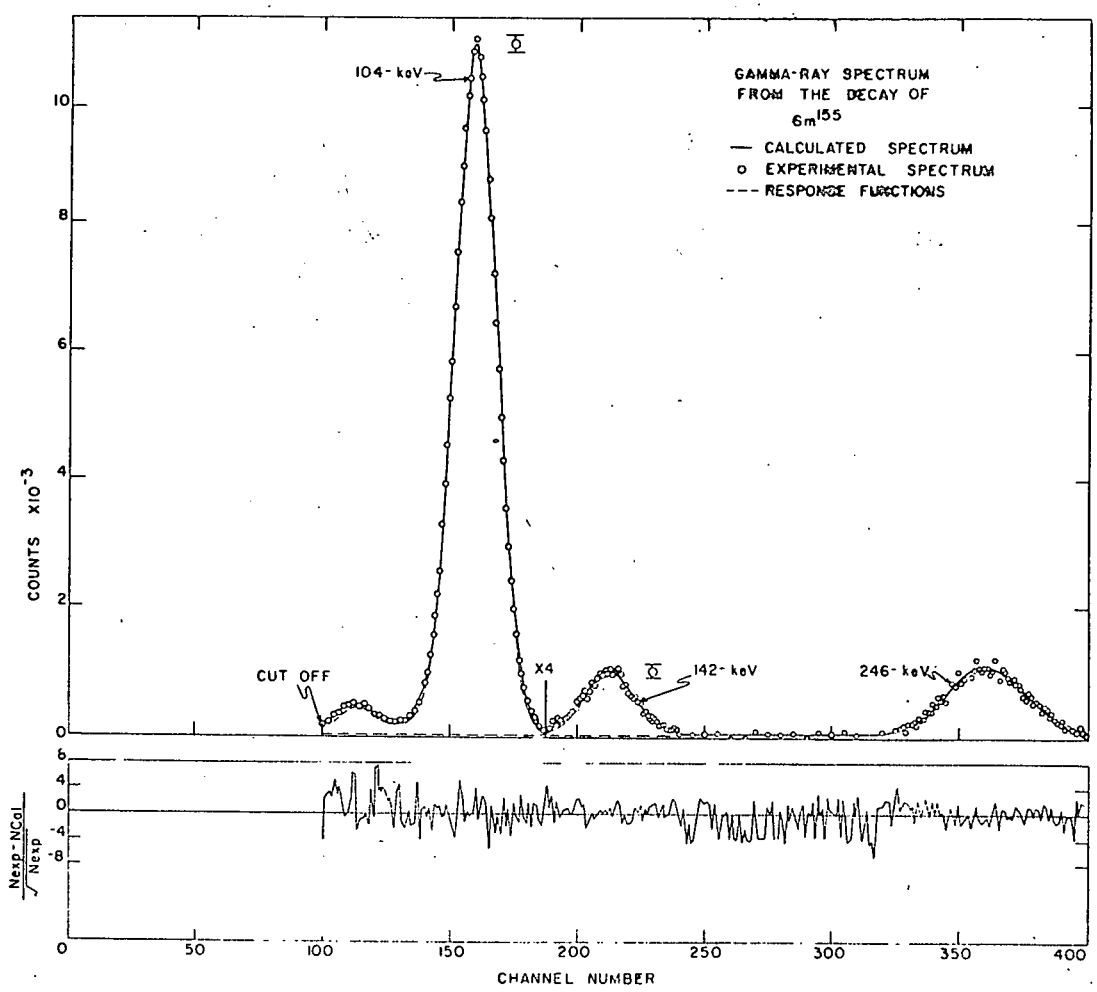

Figure 37. Eu^{155} composite spectrum below 250-keV with composite spectrum and monoenergetic components

of the experimental spectrum from the calculated spectrum. The weighted averages for the gamma-ray intensities from the seven sets of data are presented in Table 8 along with the previously reported values. The present values for the intensity of the 104-keV and 246-keV gamma rays are in agreement with the values of Funke et al. (68) and Kracik et al. (69). The present value for the 142-keV gamma ray is higher than any of the previously reported values. It is interesting to note that the ratio of the 246-keV gamma ray to the 142-keV gamma ray for the present measurement and for the recent measurement of Potnis et al. (70) are in good agreement. The gamma-ray relative intensities of Funke et al. (68) and Potnis et al. (70) were obtained with Ge(Li) detectors. The 104-keV and 142-keV gamma rays are on top of the large Compton distribution from the 246-keV gamma rays. This can add a large uncertainty to the determination of the intensities of these gamma rays, particularly the 142-keV gamma rays.

Schmid and Burson (73) have measured conversion coefficients for the 104-keV and 142-keV transitions from beta-gamma coincidences. Kracik et al. (69) have measured the conversion coefficients for the 104-keV and 246-keV transitions by measuring the percentage of the total decays which are due to conversion electrons from the 104-keV and 246-keV transitions by measuring the conversion line intensities relative to the continuous beta spectrum with a magnetic spectrometer. The gamma-ray intensities can then be normalized by assuming the 104-keV and 246-keV transitions are the only ones which lead to the ground state. This means that the total transition intensity for these transitions must be 100 percent. Because of the half life of the source, this was a very difficult experiment to do. Both of

Table 8. Eu^{155} gamma-ray relative intensities following the decay of Sm^{155}

Reference		Energy (keV) 104	142	246
Present results		2000±90	56±5	100±6
Potnis et al.	(70)	2000	48	88
Funke et al.	(68)	2000±200	45±5	100
Kracik et al.	(69)	2000	49	108
Funke et al.	(71)	2000	49	114
Sund et al.	(72)	2000	26	134
Schmid and Burson	(73)	2000	31	83

the reported values for the 104-keV transition are higher than the theoretical prediction for a pure E1 transition, Schmid and Burson's being 29 percent higher and Kracik et al. being 76 percent higher. Also, Schmid and Burson's value for the 142-keV transition is 69 percent higher than the theoretical prediction for a pure E1 transition. The value of Kracik et al. (69) for the 246-keV transition is in agreement with a pure M1 transition. The errors in the reported values are from 22 percent to 40 percent. It is hoped that by using the present accurately determined gamma-ray intensities along with conversion electron intensities measured with a Si(Li) detector, accurate conversion coefficients can be determined for these transitions. A more meaningful comparison can then be made with the

theoretical predictions. The Si(Li) measurements are presently being carried out.*

E. Concluding Remarks

Gamma-ray and X-ray relative intensities and internal conversion coefficients from five different isotopes were measured and reported in this investigation. The gamma-ray and X-ray relative intensities were measured with uncertainties from 2 percent to 19 percent and the internal conversion coefficients had uncertainties from 3 percent to 14 percent. The K internal conversion coefficients of the E2 transitions in Yb^{170} and Er^{166} were measured in an attempt to clear up the controversy over these values. The present results for the K internal conversion coefficients for these transitions are approximately 5 percent higher than the theoretical values.

The relative intensities of the gamma rays from the decay of Hf^{180m} determined in this investigation are in good agreement with the reported values of Edwards and Boehm (57) except for the 501-keV transition. The present value was a direct measurement while the value of Edwards and Boehm (57) was deduced from their other data. Because of the good agreement of the gamma-ray relative intensities and since the internal conversion electron ratios of Edwards and Boehm (57) were used in the present investigation, the values of the internal conversion coefficients reported here are

---

*These measurements are presently being carried out at the Ames Laboratory by D. F. Boneau.

in agreement with those of Edwards and Boehm (57). The 10 percent deviation in the K-conversion coefficients of the E2 transitions reported by Edwards and Boehm remains.

The gamma-ray relative intensities reported in the present studies of the 105-keV, 86-keV and 60-keV transitions from the decay of Eu^{155} are in agreement with most of the reported values for these transitions. The K internal conversion coefficients for the 105-keV and 86-keV transitions determined in this investigation are in good agreement with the revised values of Subba Rao (4) and with the theoretical predictions for pure E1 transitions.

The gamma-ray relative intensities of the 104-keV and 246-keV transitions from the decay of Sm^{155} reported in the present work are in agreement with the values for these transitions reported by Funke et al. (68) and Kracik et al. (69). The present value for the 142-keV transition is slightly higher than the previously reported values.

V. LITERATURE CITED

1. Rose, M. E. Internal conversion coefficients. New York, N.Y., Interscience Publishers, Inc. 1958.

2. Sliv, L. A. and I. M. Band. Tables of internal conversion coefficients. In Siegbahn, K., ed. Alpha-, beta- and gamma-ray spectroscopy. pp. 1639-1672. Amsterdam, Holland, North-Holland Publishing Co. 1965.

3. Church, E. L. and J. Weneser. Phys. Rev. 104: 1382. 1956.

4. Subba Rao, B. N. Nuclear Instr. and Methods 45: 22. 1966.

5. Hultberg, S. and R. Stockendal. Arkiv Fys. 14: 565. 1959.

6. Jansen, J. F., S. Hultberg, P. F. A. Goudsmit and A. H. Wapstra. Nuclear Phys. 38: 121. 1962.

7. Wapstra, A. H., G. J. Nijgh and R. van Lieshout. Nuclear spectroscopy tables. New York, N.Y., Interscience Publishers, Inc. 1959.

8. Hultberg, S. Arkiv Fys. 15: 307. 1959.

9. Lind, D. A., W. J. West and J. W. M. DuMond. Phys. Rev. 77: 475. 1950.

10. Hatch, E. N. Nuclear energy levels in Tm 169 and Lu 175. Unpublished Ph.D. thesis. Pasadena, California, Library, California Institute of Technology. 1956.

11. Bergvall, P. Arkiv Fys. 17: 125. 1960.

12. Edwards, W. F. and F. Boehm. Phys. Rev. 121: 1499. 1961.

13. Edwards, W. F. Experimental studies of conversion coefficients in some deformed nuclei. Unpublished Ph.D. thesis. Pasadena, California, Library, California Institute of Technology. 1960.

14. Reynolds, J. C. U.S. Atomic Energy Commission Report ANL 5829: 61 Argonne National Lab., Lemont, Ill. . 1958.

15. Trombka, J. I. On the analysis of gamma ray pulse height spectrum. Unpublished Ph.D. thesis. Ann Arbor, Michigan, Library, University of Michigan. 1961.

16. Trombka, J. I. U.S. Atomic Energy Commission Report NAS-NS-3107: 183 (National Academy of Sciences, Nuclear Sciences series). 1962.

17. Heath, R. L. Institute of Radio Engineers Transactions on Nuclear Science NS-9, No. 3: 294. 1962.

18. Ferguson, A. J. U.S. Atomic Energy Commission Report NAS-NS-3107: 157 (National Academy of Sciences, Nuclear Sciences series). 1962.

19. Salmon, L. U.S. Atomic Energy Commission Report NAS-NS-3107: 165 National Academy of Sciences, Nuclear Sciences series). 1962.

20. Parr, R. M. and H. F. Lucas, Jr. Analysis of complex gamma-ray spectra. IEEE Trans. Nucl. Sci. NS-11 (3). 1964.

21. McWilliams, P., W. S. Hall and H. E. Wegner. Rev. Sci. Instr. 33: 70. 1962.

22. Brown, J. E. and E. N. Hatch. U.S. Atomic Energy Commission Report IS-993 Iowa State Univ. of Science and Technology, Ames. Inst. for Atomic Research . 1964.

23. Vegors, S. H., Jr., L. L. Marsden and R. L. Heath. U.S. Atomic Energy Commission Report IDO-16370 (Phillips Petroleum Co. Atomic Energy Div., Idaho Falls, Idaho). 1958.

24. Grodstein, G. W. National Bureau of Standards Circular 583. 1957.

25. McGinnies, R. T. National Bureau of Standards Supplement to Circular 583. 1959.

26. Brown, J. E. and E. N. Hatch. Nuclear Instr. and Methods 47: 185. 1967.

27. Beers, Y. Introduction to the theory of error. Reading, Mass., Addison-Wesley Publishing Company, Inc. 1957.

28. Seppi, E. J., J. Henrikson, F. Boehm and J. W. M. DuMond. Nuclear Instr. and Methods 16: 17. 1962.

29. Boasso, C. J. A precise source positioning system for a bent-crystal spectrometer. Unpublished M.S. thesis. Ames, Iowa, Library, Iowa State University of Science and Technology. 1964.

30. DuMond, J. W. M. and H. A. Kirkpatrick. Rev. Sci. Instr. 1: 88. 1930.

31. Helmer, R. G., R. L. Heath, D. D. Metcalf and G. A. Cazier. U.S. Atomic Energy Commission Report IDO-17015 Phillips Petroleum Co. Atomic Energy Div., Idaho Falls, Idaho . 1964.

32. Nuclear Data Group. Nuclear data sheets. Washington, D.C., National Academy of Science. 1958-1967.

33. Church, E. L. and J. Weneser. Ann. Rev. Nuclear Sci. 10: 193. 1960.

34. Hatch, E. N., G. W. Eakins, G. C. Nelson and R. E. McAdams. Method for measuring internal conversion coefficients using a bent-crystal gamma-ray monochromator and a magnetic electron spectrometer. In Proc. of International Conf. on the Internal Conversion Process, Vanderbilt University, 1965. pp. 183-192. New York, N.Y., Academic Press. 1966.

35. Graham, R. L., J. L. Wolfson and R. E. Bell. Can. J. Phys. 30: 459. 1952.

36. Dingus, R. S., W. L. Talbert, Jr. and M. G. Stewart. Nuclear Phys. 83: 545. 1966.

37. Hooton, B. W. Nuclear Phys. 59: 341. 1964.

38. Liden, K. and N. Starfelt. Arkiv Fys. 7: 109. 1954.

39. Croft, W. L., B. G. Pettersson and J. H. Hamilton. Nuclear Phys. 70: 273. 1965.

40. Bisi, A., E. Germagnoli and L. Zappa. Nuovo Cim. 3: 1007. 1956.

41. McGowan, F. K. and P. H. Stelson. Phys. Rev. 107: 1674. 1957.

42. Bernstein, E. M. Phys. Rev. Letters 8: 100. 1962.

43. Fossan, D. B. and B. Herskind. Phys. Letters 2: 155. 1962.

44. Sunyar, A. W. Phys. Rev. 93: 1345. 1954.

45. Marklund, I., B. Van Nooijen and Z. Grabowski. Nuclear Phys. 15: 533. 1960.

46. Foglio, A. and M. M. Bettoni. Energia Nucl. 9: 677. 1962.

47. Nelson, G. C. and E. N. Hatch. Bull. Am. Phys. Soc. Ser. 2, 11: 459. 1966.

48. Day, P. P. Phys. Rev. 102: 1572. 1956.

49. Bhalla, C. P. Phys. Rev. 157: 1136. 1967.

50. Jansen, J. F. W. and A. H. Wapstra. Determination of the conversion coefficient in Yb 170 with scintillation methods. In Proc. of International Conf. on the Internal Conversion Process, Vanderbilt University, 1965. pp. 237-252. New York, N.Y., Academic Press. 1966.

51. Houtermans, H. Z. Phys. 149: 215. 1957.

52. Jansen, J. F. W., S. Hultberg, P. F. A. Goudsmit and A. H. Wapstra. Nuclear Phys. 38: 121. 1962.

53. Erman, P. and S. Hultberg. On the anomalies of E2 conversion coefficients in the deformed-nucleus region. In Proc. of International Conf. on the Internal Conversion Process, Vanderbilt University, 1965. pp. 249-252. New York, N.Y., Academic Press. 1966.

54. Thosar, B. V., M. C. Joshi, R. P. Sharma and K. G. Prasad. Nuclear Phys. 50: 305. 1964.

55. Helmer, R. G. and S. B. Burson. Phys. Rev. 119: 788. 1960.

56. Gelletly, W., J. S. Geiger and R. L. Graham. Phys. Rev. 157: 1043. 1967.

57. Edwards, W. F. and F. Boehm. Phys. Rev. 121: 1499. 1961.

58. Deutsch, M. and T. W. Bauer. Nuclear Phys. 21: 128. 1960.

59. Nelson, G. C. and E. N. Hatch. Z. Physik 202: 293. 1967.

60. Gvozdev, V. S. and L. I. Rusinov. Akademiia Nauk, SSSR, Doklady 112: 401. 1957.

61. Scharff-Goldhaber, G. and M. McKeown. Phys. Rev. Letters 18, No. 16: A6. 1967.

62. Bodenstedt, E., H. J. Komer, E. Gerdau, J. Radeloff, C. Gunther and G. Strube. Z. Physik 165: 57. 1961.

63. Paul, H., M. McKeown and G. Scharff-Goldhaber. Phys. Rev. Letters 18, No. 16: A6. 1967.

64. Hatch, E. N. and F. Boehm. Z. Physik 155: 609. 1959.

65. Subba Rao, B. N. Nuovo Cim. 16: 283. 1960.

66. Vergnes, M. Compt. rend. 248: 1158. 1959.

67. Harmatz, B., T. H. Handley and J. W. Mihelich. Phys. Rev. 128: 1186. 1962.

68. Funke, L., H. Graber, K. H. Kaun, H. Sodan and J. Frana. Nuclear Phys. 88: 641. 1966.

69. Kracik, B., Z. Miligui, V. Brabec, M. Vejs, A. Mastalka and T. Kucarova. Czech. J. Phys. 13: 79. 1963.

70. Potnis, V. R., G. P. Aginuud and C. E. Mandeville. Bull. Am. Phys. Soc. Ser. 2, 12: 579. 1967.

71. Funke, L., H. Graber, K. H. Kaun, H. Sodan and L. Werner. Nuclear Phys. 70: 335. 1965.

72. Sund, R. E., R. G. Arns and M. L. Wiedenbeck. Phys. Rev. 118: 776. 1960.

73. Schmid, L. C. and S. B. Burson. Phys. Rev. 115: 447. 1959.

74. Stevenson, P. C. U.S. Atomic Energy Commission Report NAS-NS-3109 (National Academy of Sciences, Nuclear Sciences series). 1965.

75. Kenney, J. F. and E. S. Keeping. The mathematics of statistics. 2nd ed. Part 2. Princeton, New Jersey, D. Van Nostrand Co., Inc. 1951.

76. Scheffé, H. The analysis of variance. New York, N.Y., John Wiley and Sons, Inc. 1959.

77. Fry, T. C. Probability and its engineering uses. New York, N.Y., D. Van Nostrand Company, Inc. 1928.

VI. ACKNOWLEDGMENTS

The authors express their appreciation to:

Mr. George Eakins for his assistance with the maintenance of the electronic equipment which prevented equipment failure from causing a major delay.

Dr. W. L. Talbert, Jr., Mr. John McConnell and Mr. Bengt Anderberg for the separation of the Tm^{170} source on the Ames Laboratory isotope separator.

Mr. James Reierson for his assistance with the linear least-squares computer program.

Mr. Michael Yester for writing the NaI efficiency computer program.

Mr. Kenneth L. Malaby and Harold S. Olson for their assistance in preparing and handling the source materials.

Mr. Bruce Link and his staff for their cooperation and assistance during the reactor irradiations of the sources.

Mr. Roland Struss for designing the rabbit and transfer system.

VII. APPENDIX A: EFFECTS DUE TO SOURCE WIDTH AND POSITION

The present method for measuring the gamma-ray relative intensities assumes that the composite spectrum and response functions are measured under identical conditions. Since it was desirable to use a thin composite source that was wider than the line source and since the geometry with respect to the room was slightly different for the thin source and line source, an investigation was made to determine the effects of varying the thin source width and position. The procedure used was to record a "normal" pulse-height spectrum and a pulse-height spectrum under the condition being checked. The "normal" pulse-height spectrum was recorded with the thin source located at the position where the data which are described in this dissertation were recorded. The two spectra were then normalized to a constant area and subtracted. The type of effects looked for were due to scattering and a change in the photopeak to total ratio. For a constant source to crystal distance the effects due to scattering would be much larger than those due to a change in photopeak to total ratio. This is not necessarily true when the source to crystal distance is changed drastically.

If the differences fluctuate statistically around zero it was assumed that there was no observable difference in the spectra and that either source position was equally good. If the difference remains positive or negative over several channels it was assumed that there were effects due to either scattering and/or a change in the photopeak to total ratio. If these cases were used in the least-squares fitting procedure the goodness of fit parameter S^2, would be large and the data would be rejected as

unreliable.

The effect of varying the source width was determined by recording the composite spectra from Yb^{169} sources of 0.5 mm, 3 mm and 5 mm wide and subtracting each of these from a second spectrum obtained from the 0.5 mm wide Yb^{169} source. The spectra were normalized such that the total area was a constant. These differences are shown in Figure 38. The investigation of the scattering due to the slight difference in geometry between the composite source and the source used for the response functions was carried out in the following way. The pulse-height spectrum from a thin Eu^{155} source 2 mm wide was recorded at three different positions on the focal circle. These positions were the normal source position, two inches and six inches to the left of the normal source position. The spectra were again normalized so that the total area was a constant and were subtracted from the spectrum recorded at the normal source position. Figure 39 displays these differences.

Four other effects of source width and position were investigated. These are the effect of the thin source not being perpendicular to the collimator, scattering due to the crystal clamping block, the effect of not being at the transmission maximum and moving the source closer to the detector. This last effect was checked with the hope of being able to use much weaker sources. These effects were again determined by recording spectra from a thin Yb^{169} source and subtracting. Figure 40 shows these differences. The top curve was obtained from spectra from a 5 mm wide disk source recorded at 0° and rotated through 70° with respect to the collimator. The next curve was obtained from a 2 mm wide source without a clamping

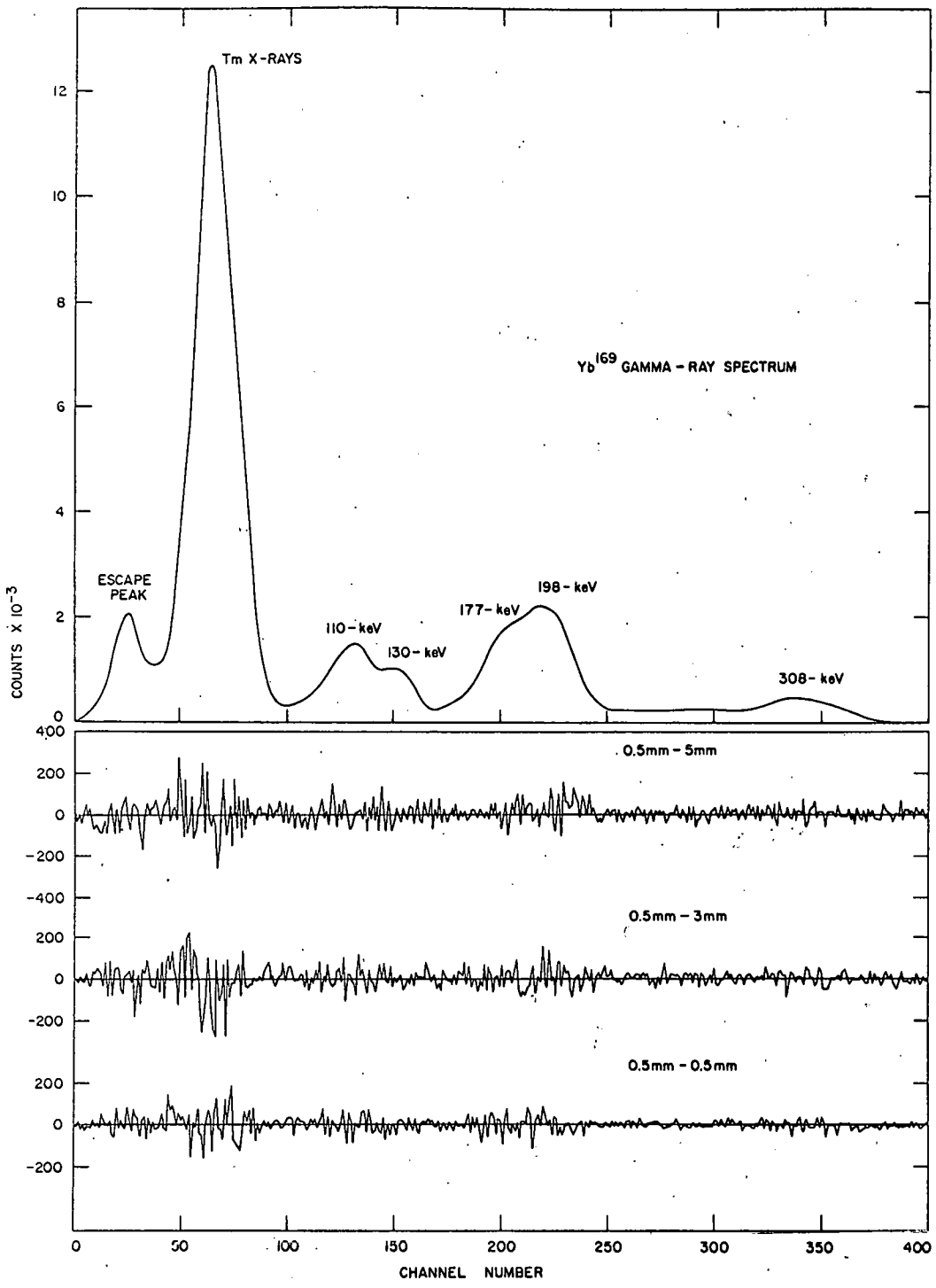

Figure 38. Comparison of the gamma-ray spectra obtained with thin sources of three different widths

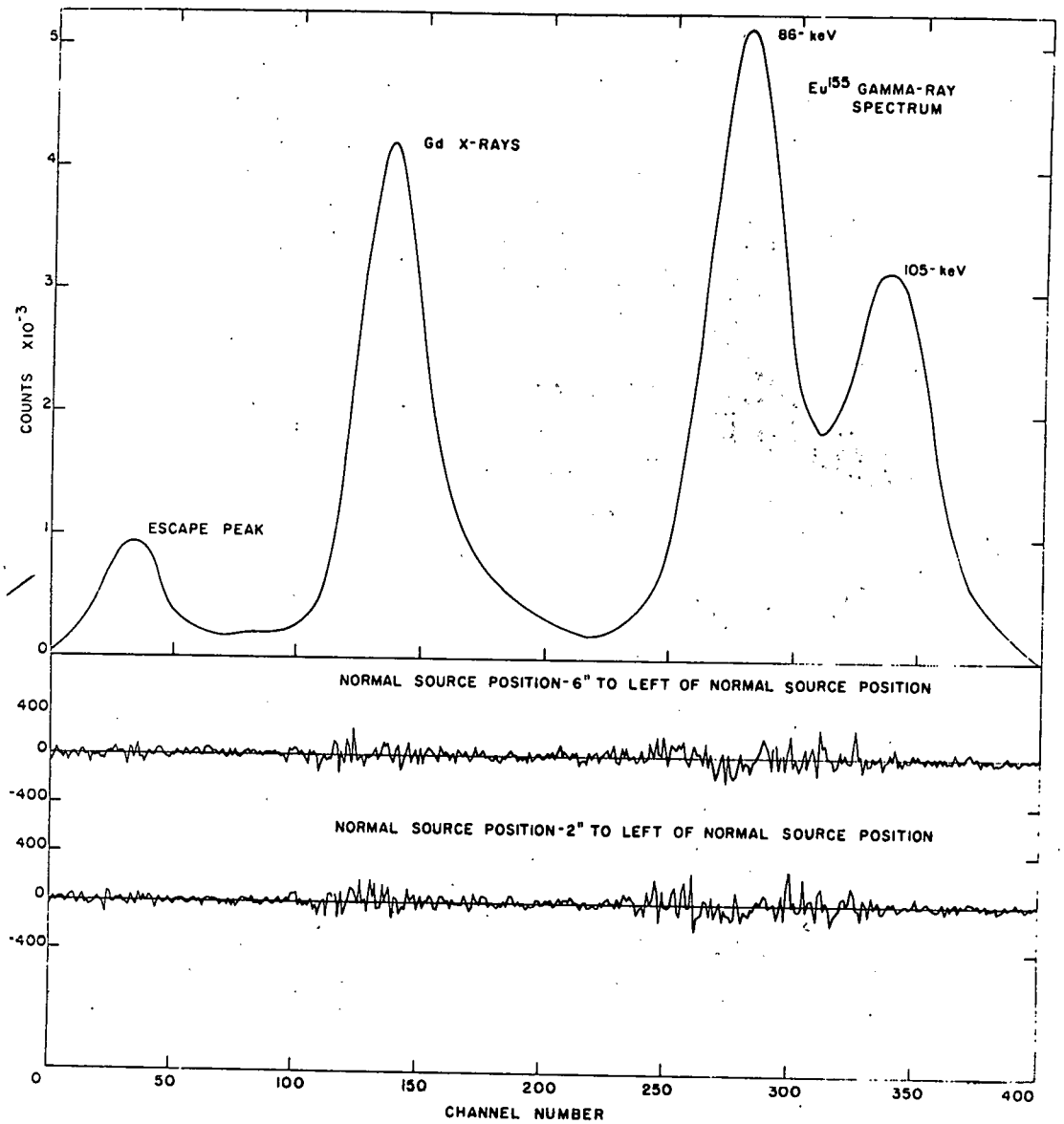

Figure 39. Comparison of the gamma-ray spectra obtained with the thin source in three different positions on the focal circle

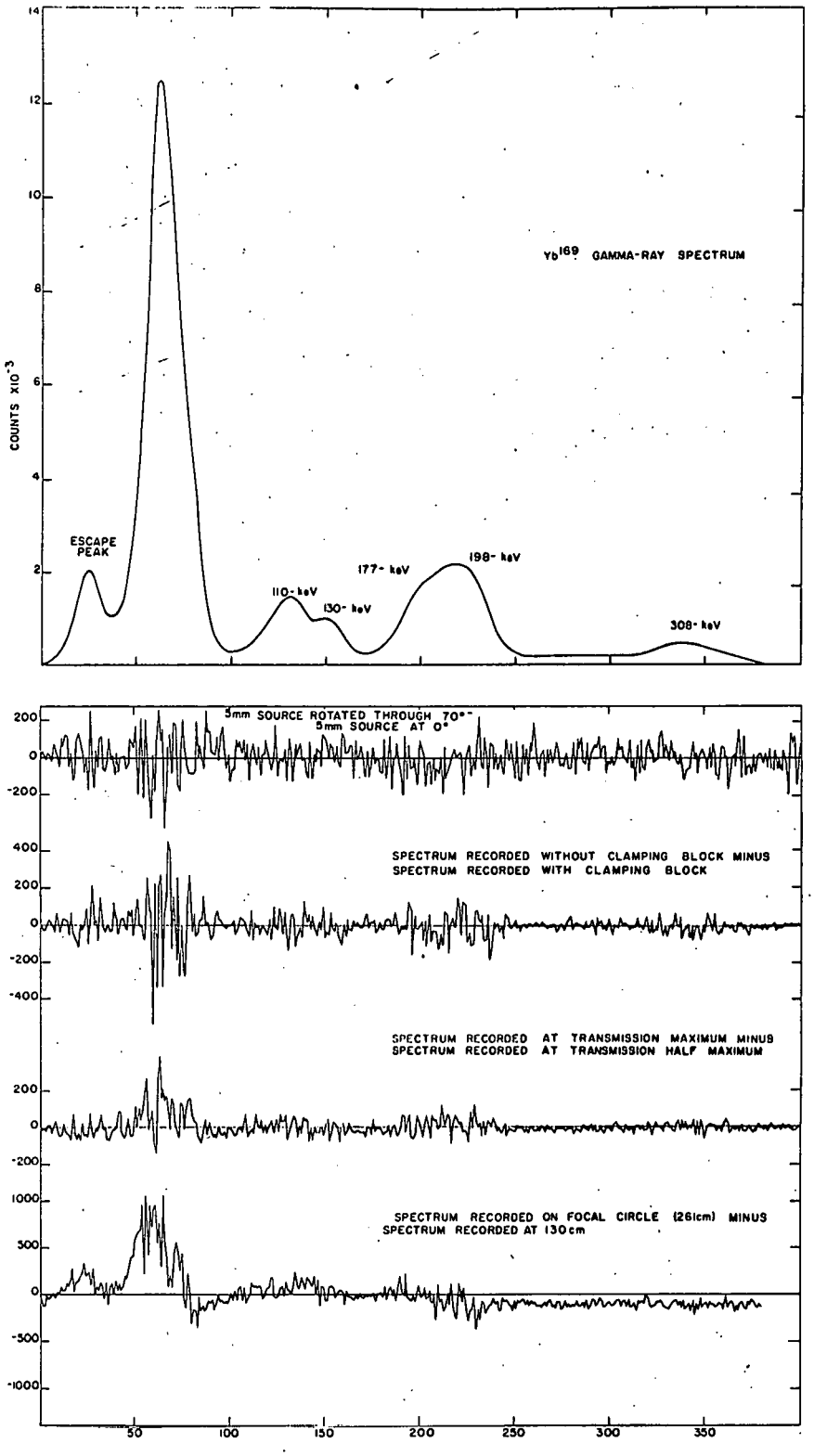

Figure 40. Comparison of the gamma-ray spectra obtained with the thin source located at its normal position on the focal circle and with it rotated through 70°, with a blank clamping block between the source and detector, with the collimator set at the transmission half maximum and with the thin source 130 cm from the detector.

block and with a clamping block which did not have a diffraction crystal. The third curve is the difference of spectra recorded at the transmission maximum and at half maximum. The bottom curve is the difference of spectra recorded from the source at 261 cm from the detector (on the focal circle) and at 130 cm. Because of the focussing properties of the collimator, the collimator plates were removed in the latter case.

As can be seen in Figures 38, 39, and 40 the difference for the various source widths and positions are statistical. Therefore, there is either very little scattering in these cases or the collimator does a very effective job in eliminating the scattering. Because of this, it was possible to keep the thickness of the thin source for the composite spectrum at a minimum by making it wider. The optimum width was approximately 2 mm. Also it seems that the assumption of identical geometries for the line source and the thin source is a good one. As can be seen from the lower two curves in Figure 40 the differences are not statistical in these cases. It appears to be critical that the collimator and detector are set at the transmission maximum. However, this can easily be done by recording the count rate as a function of detector position. Also, it appears that it is not possible to move the source closer to the detector to achieve higher counting rates.

VIII. APPENDIX B: CALCULATION OF THE EFFICIENCY OF THE NAI CRYSTAL

This appendix describes the calculation of the efficiency of a 3 inch x 3 inch NaI(Tl) crystal for a line source 1 inch long and 261 cm from the detector. These calculations were done in collaboration with Michael Yester.

The efficiency is defined as the fraction of the gamma rays which are emitted from a source that are detected by the NaI(Tl) crystal. The fraction of the particles with energy E that strike a crystal of thickness t and absorption coefficient τ that will be absorbed is given by

$$(1 - e^{-\tau(E)t}) \quad .$$

The efficiency for a line source is then given by

$$T(E) = \frac{1}{4\pi L} \int_0^L \int_0^{2\pi} \int_0^{\Theta_{max}} (1-e^{-\tau(E)t}) \sin\Theta d\Theta \, d\phi dx \qquad \text{Equation 13}$$

where $4\pi L$ is the total solid angle. Due to the symmetry, Equation 13 can be rewritten as

$$I(L) = \frac{1}{4\pi L} (2) (2) \int_0^{L/2} \int_{-\pi/2}^{\pi/2} \int_0^{\Theta_{max}} (1-e^{-\tau(E)t}) \sin\Theta d\Theta d\phi dx \quad .$$

Equation 14

As can be seen in Figure 41 the integral over Θ must be divided into two parts corresponding to a gamma ray exiting through the bottom or the side of the crystal. Therefore,

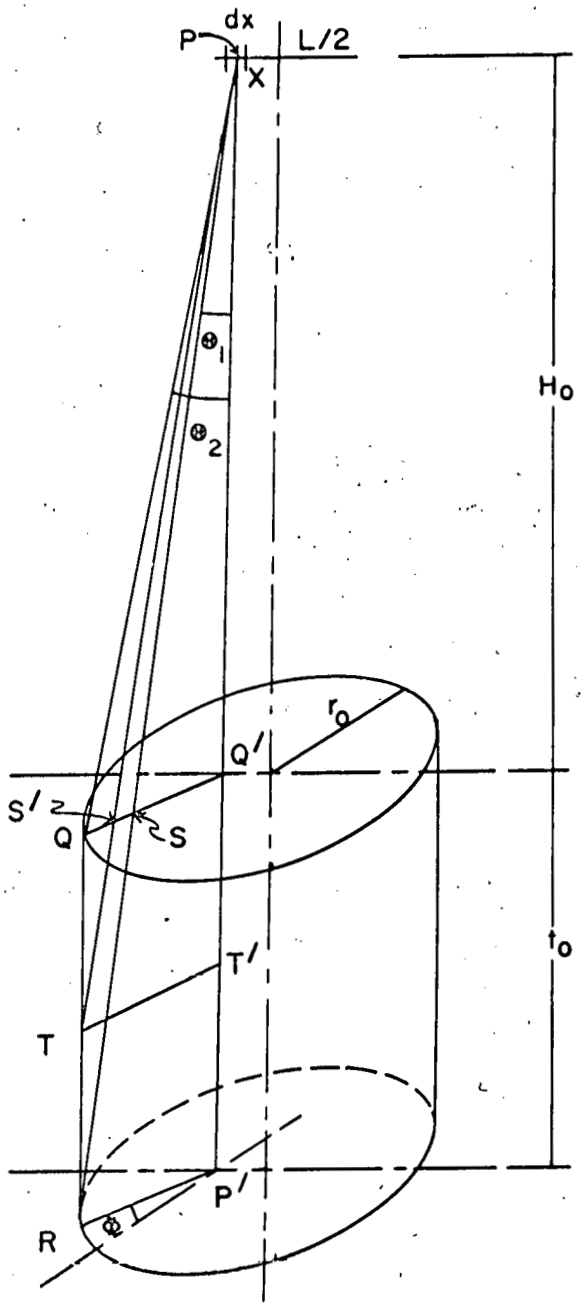

Figure 41. Source-detector geometry for a line source of length L and a distance H_0 from a NaI(Tl) crystal of thickness t_0 and a radius r_0

$$T(E) = \frac{1}{4\pi L} \int_0^{L/2} \int_{\pi/2}^{\pi/2} \left[\int_0^{\Theta_1} (1-e^{-\tau t_1}) \sin\Theta d\Theta \right.$$

$$\left. + \int_{\Theta_1}^{\Theta_2} (1-e^{-\tau t_2}) \sin\Theta d\Theta \right] d\phi dx \ . \qquad \text{Equation 15}$$

First consider only the case in which the gamma ray leaves through the bottom of the crystal. Consider the line source as a series of point sources a distance x from the axis of the crystal, where $0 \leq x \leq L/2$. Θ_1 is the angle between the perpendicular from the point source to the crystal and the line PR in Figure 41. By finding $\overline{P'R}$, Θ_1 can be determined from the relation

$$\Theta_1 = \tan^{-1}\left(\frac{\overline{P'R}}{H_0+t_0} \right) \ . \qquad \text{Equation 16}$$

From triangle ORU in Figure 42 we have

$$\overline{RU}^2 = \overline{OR}^2 - \overline{OU}^2,$$

but $\overline{OR}^2 = r_0^2$,

and $\overline{OU}^2 = (x-\overline{P'U})^2$,

so $\overline{RU}^2 = r_0^2 - (x+\overline{P'U})^2$,

therefore $\overline{RU}^2 = r_0^2 - x^2 - 2x\overline{P'U} - (\overline{P'U})^2$. Equation 17

From the triangle P'RU in Figure 42

$$\overline{RU}^2 = \overline{P'R}^2 - \overline{P'U}^2 \quad . \qquad \text{Equation 18}$$

Combining Equations 17 and 18 we get

$$r_0^2 - x^2 - 2x\overline{P'U} - \overline{P'U}^2 = \overline{P'R}^2 - \overline{P'U}^2 ,$$

or $$r_0^2 - x^2 - 2x\overline{P'U} = \overline{P'R}^2 ,$$

but $\overline{P'U} = \overline{P'R} \sin\phi$,

so $r_0^2 - x^2 - 2x\overline{P'R} \sin\phi = \overline{P'R}^2$. Equation 19

Rearranging Equation 19 and solving for $\overline{P'R}$ we obtain

$$\overline{P'R} = -x \sin\phi + \sqrt{x^2\sin^2\phi - (x^2 - r_0^2)} \quad . \qquad \text{Equation 20}$$

Using Equation 20 in Equation 16 we get

$$\theta_1 = \tan^{-1}\left[\frac{-x \sin\phi + \sqrt{x^2\sin^2\phi - (x^2 - r_0^2)}}{H_0 + t_0}\right] \quad . \qquad \text{Equation 21}$$

The distance t_1 a gamma ray will travel through the crystal can be found from Figure 41

$$t_1 = \overline{SR} ,$$

but $\overline{SR} = t_0/\cos\theta$,

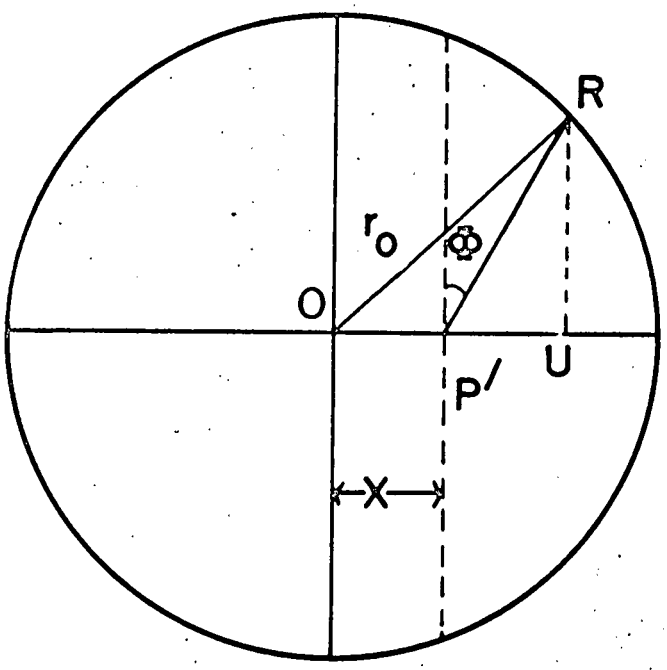

Figure 42. Geometry used in the plane normal to the NaI(Tl) crystal to determine the equations for the efficiency

so $t_1 = t_0/\cos\Theta$. Equation 22

Now consider the case where the gamma ray exits through the side of the crystal. It is evident from Figure 46 that

$$\Theta_2 = \tan^{-1}\left[\left(\frac{\overline{Q'Q}}{H_0}\right)\right] , \qquad \text{Equation 23}$$

but $\overline{Q'Q} = \overline{P'R}$.

Therefore, substituting Equation 20 into Equation 24 we have

$$\Theta_2 = \tan^{-1}\left[\frac{-x\sin\phi + \sqrt{x^2\sin^2\phi-(x^2-r_0^2)}}{H_0}\right] . \qquad \text{Equation 25}$$

From Figure 41 it can be seen that

$$t_2 = \overline{S'T} = \overline{PT}-\overline{PS'} ,$$

$$\text{but } \overline{PT} = \frac{\overline{TT'}}{\sin\Theta} = \frac{\overline{P'R}}{\sin\Theta} = \frac{-x\sin\phi + \sqrt{x^2\sin^2\phi-(x^2-r_0^2)}}{\sin\Theta}$$

$$\text{and } \overline{PS'} = \frac{H_0}{\cos\Theta}$$

$$\text{so } t_2 = \frac{-x\sin\phi + \sqrt{x^2\sin^2\phi-(x^2-r_0^2)}}{\sin\Theta} - \frac{H_0}{\cos\Theta} . \qquad \text{Equation 26}$$

Combining Equations 21, 22, 24 and 26 with Equation 15 we have

$$T(E) = \frac{1}{\pi L} \int_0^{L/2} \int_{-\pi/2}^{\pi/2} \left\{ \int_0^{\tan^{-1}\left(\frac{-x\sin\phi + \sqrt{x^2\sin^2\phi-(x^2-r_0^2)}}{H_0+t_0}\right)} \left[1-e^{-\frac{\tau t_0}{\cos\theta}}\right] \sin\theta d\theta \right.$$

$$\left. + \int_{\tan^{-1}\left(\frac{-x\sin\phi+\sqrt{x^2\sin^2\phi-(x^2-r_0^2)}}{H_0}\right)}^{\tan^{-1}\left(\frac{-x\sin\phi+\sqrt{x^2\sin^2\phi-(x^2-r_0^2)}}{H_0+t_0}\right)} \left[1-e^{-\tau\left(\frac{-x\sin\phi+\sqrt{x^2\sin^2\phi-(x^2-r_0^2)}}{\sin\theta} - \frac{H_0}{\cos\theta}\right)}\right] \sin\theta d\theta \right\} d\phi dx$$

Equation 27

where L = source length

r_0 = radius of the NaI(Tl) detector

$\tau(E)$ = absorption coefficient for energy E

t_0 = thickness of NaI(Tl) crystal.

Equation 27 was numerically integrated using the trapezoidal rule and an IBM 7074 computer. The input parameters for the computer program were r_0, t_0, H_0, L, E, τ and the number of intervals to be used for each integral. The absorption coefficients $\tau(E)$ were taken from the tables of Vegors et al. (23).

As a check on the accuracy of the computer program, a comparison was made with the calculations of Vegors et al. (23) for H_0 = 10 cm and L = 0.75 inches. The difference was less than 1 percent for energies above 50-keV. The differences were probably due to the different methods used in the numerical integration. When H_0 = 261 cm the variables change much more slowly and it is believed that the agreement would be even better at this distance.

The dependence of the efficiency on the source length and the distance between the source and crystal was determined. In Table 9 are given the efficiencies at four energies for source lengths of 0.25, 0.50 and 1.00 inches and a source to crystal distance of 261 cm. As can be seen, the efficiency is independent of the source length in the given ranges. The variation of efficiency as a function of source to crystal distance is given in Figure 43. At 500-keV the efficiency only changes by 0.02 percent for a variation in the source to crystal distance of 2 cm.

Table 9. The efficiency of a 3 inch x 3 inch NaI(Tl) crystal for a source to crystal distance of 261 cm as a function of energy and source length

Energy (keV)	Source length 0.25"	0.50"	1.00"
	Efficiency		
50	1.0000	1.0000	1.0000
150	0.9975	0.9975	0.9974
300	0.9949	0.9949	0.9947
500	0.9041	0.9041	0.9038

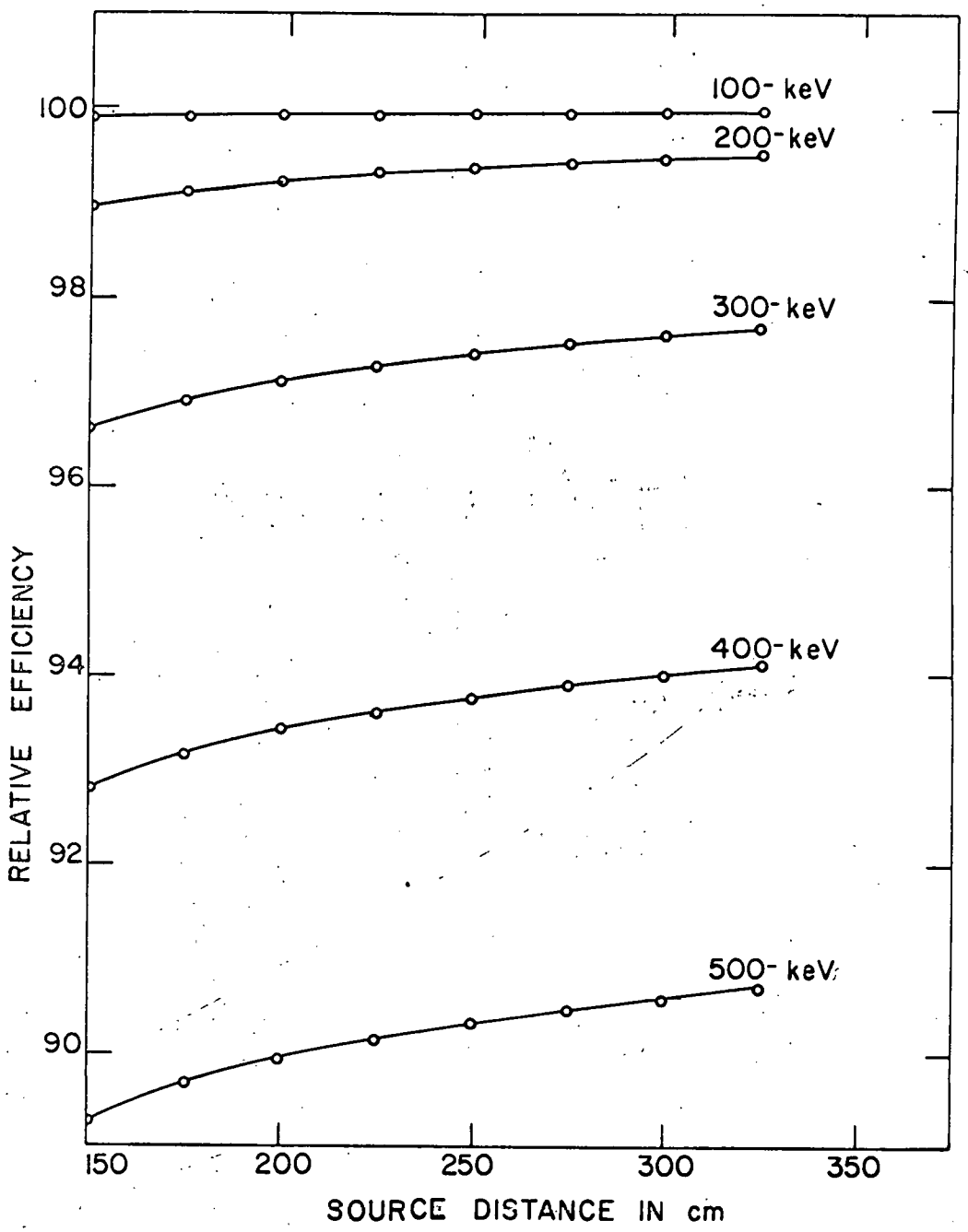

Figure 43. Relative efficiency of a 3" x 3" NaI(Tl) crystal as a function of energy and distance from the source

Figure 44 is the relative efficiency as a function of energy of a 3 inch x 3 inch NaI(Tl) crystal for a line source 1 inch long and 261 cm from the crystal. An error of ±1 percent was assigned to the values read from the graph.

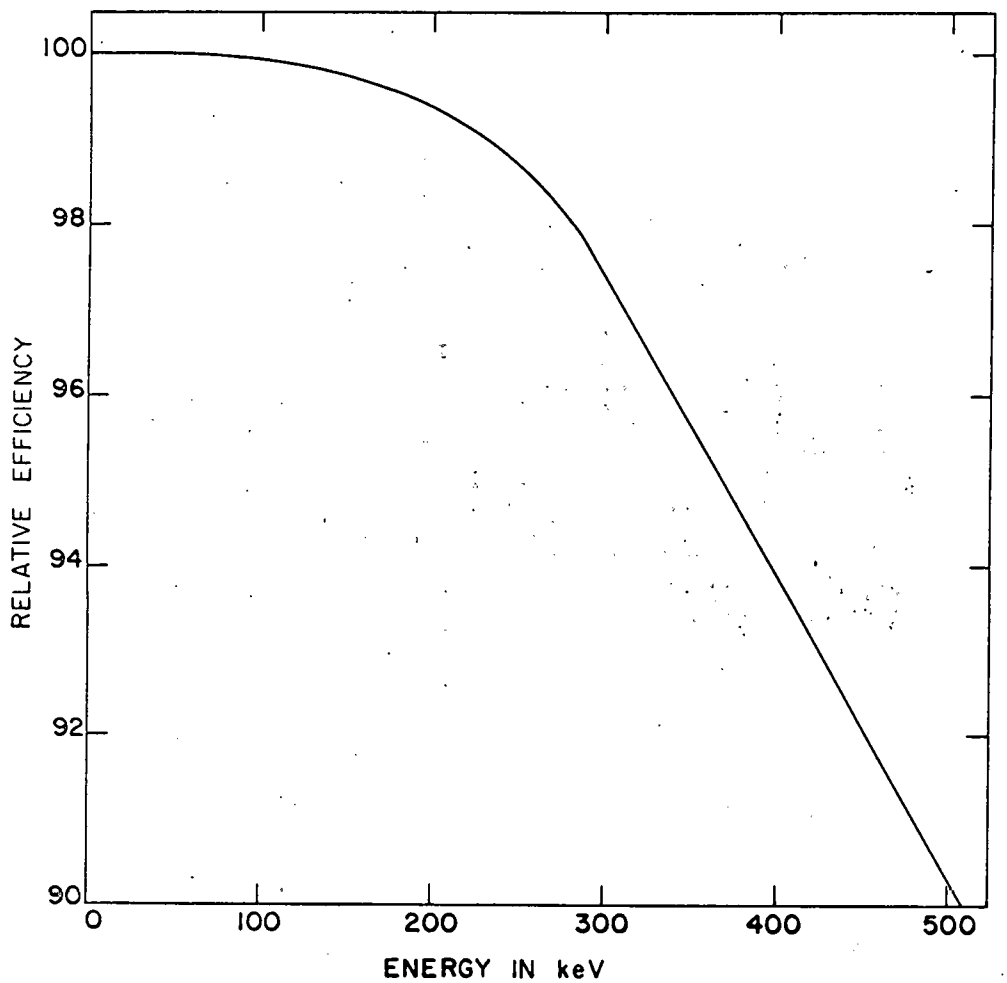

Figure 44. Relative efficiency of a 3" x 3" NaI(Tl) crystal 261 cm from a one inch line source as a function of energy

IX. APPENDIX C: DERIVATION OF THE ERRORS ASSOCIATED WITH THE LINEAR LEAST-SQUARES PROCEDURE

In this appendix the equations used in the determination of the standard deviations of the gamma-ray relative intensities will be derived.

To determine the standard deviations of the B_i, several theorems about expected values will be needed. The proofs below follow those of Stevenson (74). We define the expected value of any function of the variable z as $E\left[f(z)\right]$ by

$$E\left[f(z)\right] = \int_{-\infty}^{\infty} f(u)\ p_z(u)du$$

where $p_z(u)$ is the distribution function of z. The distribution function $p_z(u)$ of the variable z is defined such that $p_z(u)du$ is the probability that a measurement value of z will be between u and u+du. $p_z(u)$ is normalized such that

$$\int_{-\infty}^{\infty} p_z(u)du = 1.$$

Also define the covariance of two variables z and h by

$$\mathrm{cov}(z,h) = E\left[\left[z-E(z)\right]\left[h-E(h)\right]\right].$$

The variance of z is defined by $\mathrm{var}(z) = E\left[\left[z-E(z)\right]^2\right] = \sigma_z^2$, where σ_z is called the standard deviation of z. Then for a constant a, the relationships follow:

$$E(a) = \int_{-\infty}^{\infty} ap_z(x)dx = a\ , \qquad \text{Equation 28}$$

$$E(az) = \int_{-\infty}^{\infty} axp_z(x)dx = aE(z)\ , \qquad \text{Equation 29}$$

$$E(a+z) = \int_{-\infty}^{\infty} (a+x)p_z(x)dx = a+E(z) \ , \qquad \text{Equation 30}$$

$$Var(a) = E\left[\left(a-E(a)\right)^2\right] = E\left[\left(a-a\right)^2\right] = 0 \ , \qquad \text{Equation 31}$$

$$Var(az) = E\left[\left(az-E(az)\right)^2\right] = E\left[\left(az-aE(z)\right)^2\right]$$

$$= E\left[a^2\left(z-E(z)\right)^2\right] = a^2\, var(z) \ , \qquad \text{Equation 32}$$

$$Var(a+z) = E\left[\left(a+z-E(a+z)\right)^2\right] = E\left[\left(a+z-a-E(z)\right)^2\right] = Var(z) \ .$$

Equation 33

Also,

$$E(z+h) = \int_{-\infty}^{\infty} xp_{z+h}(x)dx \ ,$$

but $p_{z+h}(x) = \int_{-\infty}^{\infty} p_h(v)p_z(x-v)dv$,

then $E(z+h) = \int_{-\infty}^{\infty} \int_{-\infty}^{\infty} xp_h(v)p_z(x-v)dvdx$.

Reversing the order of integration and letting x = v-v+h we get

$$E(z+h) = \int_{-\infty}^{\infty} p_h(v)\left[\int_{-\infty}^{\infty} (x-v)p_z(x-v)dx+v\int_{-\infty}^{\infty} p_z(x-v)dx\right] dv \ .$$

dx = d(x-v) for the inner integrals since v is held fixed.

$$E(z+h) = \int_{-\infty}^{\infty} p_h(v)\left[\int_{-\infty}^{\infty} (x-v)p_z(x-v)d(x-v)+v\int_{-\infty}^{\infty} p_z(x-v)d(x-v)\right] dv$$

$$= \int_{-\infty}^{\infty} p_h(v)\left[E(z)+v\right] dv = E(z)\int_{-\infty}^{\infty} p_h(v)dv+\int_{-\infty}^{\infty} vp_h(v)dv$$

$$E(z+h) = E(z)+E(h) \ . \qquad \text{Equation 34}$$

$$cov(z,h) = E\left[\left(z-E(z)\right)\left(h-E(h)\right)\right] = E\left[zh-zE(h)-hE(z)+E(z)E(h)\right]$$

$$= E(zh)-E(h)E(z)-E(z)E(h)+E(z)E(h)$$

$$= E(zh)-E(z)E(h) \ . \qquad \text{Equation 35}$$

$$\text{var}(z+h) = E\left[\left(z+h-E(z+h)\right)^2\right] = E\left[\left(z-E(z)+h-E(h)\right)^2\right]$$

$$= E\left[\left(z-E(z)\right)^2+2\left(z-E(z)\right)\left(h-E(h)\right)+\left(h-E(h)\right)^2\right]$$

$$= E\left[\left(z-E(z)\right)^2\right]+E\left[\left(h-E(h)\right)^2\right]+2E\left[\left(z-E(z)\right)\left(h-E(h)\right)\right]$$

$$\text{var}(z+h) = \text{var}(z)+\text{var}(h)+2\text{cov}(z,h). \qquad \text{Equation 36}$$

We will also need to show that the expected values of B_i determined from the normal equations are the true values. To show this we will follow the method of Kenny and Keeping (75, p. 309 ff.).

Let $A^TWA = D$, and $G = A^TWR$. Equation 37

The normal equations then become $DB = G$ and $B = D^{-1}G$ or $B_j = \sum_{k=1}^{C} (D^{-1})_{jk}G_k$. Equation 38

The expected value of B_j is then determined from Equation 29

$$E(B_j) = \sum_{k=1}^{C} (D^{-1})_{jk}E(G_k) \qquad \text{Equation 39}$$

where $E(G_k) = \sum_{i=1}^{C} a_{ki}^T\omega_i E(R_i)$. If $E(R_i) = \sum_{l=1}^{Q} a_{il}n_l$ where n_l are the true values of the B_l, then

$$E(B_j) = \sum_{k=1}^{C}\sum_{i=1}^{C}\sum_{l=1}^{Q} (D^{-1})_{jk}a_{ki}^T\omega_i a_{il}n_l = \sum_{l=1}^{Q}\left[n_l\sum_{k=1}^{C}\left[(D^{-1})_{jk}\sum_{i=1}^{C}a_{ki}^T\omega_i a_{il}\right]\right],$$

but from Equation 37 $\sum_{i=1}^{C} a_{ki}^{T}\omega_i a_{il} = D_{kl}$ so $E(B_j) = \sum_{l=1}^{Q}\left[n_l \sum_{k=1}^{C}(D^{-1})_{jk}D_{kl}\right]$.

Equation 40

Using $\sum_{k=1}^{C}(D^{-1})_{jk}D_{kl} = \delta_{jl}$ in Equation 40 we get

$$E(B_j) = \sum_{l=1}^{Q} n_l \delta_{jl} = n_j \,. \qquad \text{Equation 41}$$

We can now proceed to calculate the variances of the B_j. To do this we need to calculate the covariance matrix of the vector B. We will follow the approach due to Scheffé (76, pp. 8-12). Define the expected value of a matrix to be the matrix formed from the expected values of its components. For a vector V,

$$E(V) = \begin{pmatrix} E(V_1) \\ E(V_2) \\ \vdots \\ E(V_n) \end{pmatrix}$$

and $\operatorname{cov}(V) = E\left[\left(V-E(V)\right)\left(V-E(V)\right)^T\right]$.

For a constant matrix G and if W = GV then by applying Equation 12 we get

$$\operatorname{cov}(W) = E\left[\left(W-E(W)\right)\left(W-E(W)\right)^T\right] + E\left[G\left(V-E(V)\right)\left(V-E(V)\right)^T G^T\right]$$

$$= GE\left[\left(V-E(V)\right)\left(V-E(V)\right)^T\right]G^T = G\operatorname{cov}(V)G^T. \qquad \text{Equation 42}$$

For simplicity let $\Lambda_{ij} = \frac{a_{ij}}{\left[\text{var}(R_j)\right]^{1/2}}$ and $\Psi_j = \frac{R_j}{\left[\text{var}(R_j)\right]^{1/2}}$

Equation 43

where $\text{var}(R) = \sigma^2(R)$ from the definition of standard deviation.

Then Equation 10 becomes $B = (\Lambda^T\Lambda)^{-1}\Lambda^T\Lambda$. Equation 44

Assume the covariance matrix of Ψ is $\text{cov}(\Psi) = \sigma^2 I$

where I is the identity matrix. Then Equation 42 becomes, with $W = B$, $V = \Psi$ and $G = (\Lambda^T\Lambda)^{-1}\Lambda^T$,

$$\text{cov}(B) = (\Lambda^T\Lambda)^{-1}\Lambda^T\cdot\text{cov}(\Psi)\cdot\left[(\Lambda^T\Lambda)^{-1}\Lambda^T\right]^T$$

$$= \sigma^2(\Lambda^T\Lambda)^{-1}\cdot\Lambda^T\cdot I\cdot\Lambda\cdot\left[(\Lambda^T\Lambda)^{-1}\right]^T.$$

Since $\Lambda^T\Lambda$ is symmetrical, $(\Lambda^T\Lambda)^{-1}$ is symmetrical. Therefore,

$$\text{cov}(B) = \sigma^2(\Lambda^T\Lambda)^{-1}\cdot\Lambda^T\Lambda\cdot(\Lambda^T\Lambda)^{-1} = \sigma^2(\Lambda^T\Lambda)^{-1} .$$

Using Equation 43 one gets

$$\text{cov}(B) = \sigma^2(A^TWA)^{-1} .$$ Equation 45

We must now find an unbiased estimate of σ^2. Following the method of Kenney and Keeping (75, pp. 311-312) we define the residual r_j by

$$r_j = \Psi_j - T_j$$

where Ψ_j is, as before, the weighted observed value, and T_j is the weighted value computed from the least-squares solution. Define the error δ_j by $\delta_j = \Psi_j - \beta_j$ where β_j is the true value of Ψ_j. Then by applying Equation 34 we get

$$E(\Psi_j^2) = E\left[(\beta_j+\delta_j)^2\right] = E\left[(\beta_j^2+2\beta_j\delta_j+\delta_j^2)\right]$$

$$= E(\beta_j^2)+E(2\beta_j\delta_j)+E(\delta_j^2),$$

but from Equation 28 $E(\beta_j^2) = \beta_j^2$, and $E(\delta_j) = E(\Psi_j-\beta_j) = E(\Psi_j)-\beta_j$ from Equation 30, but from Equation 41 $E(\Psi_j) = \beta_j$, therefore, $E(\delta_j) = 0$. Also $E(\delta_j^2) = \sigma^2$ from the definition of variance. Therefore,

$$E(\Psi_j^2) = \beta_j^2+\sigma^2 \quad . \qquad \text{Equation 46}$$

If the true values of the B_i are n_i then

$$\beta_j = \sum_{i=1}^{Q} a_{ji}\, n_i / \left[\text{var}(R_j)\right]^{1/2}.$$

Therefore $E(\psi_j^2) = \sum_{i=1}^{Q}\sum_{k=1}^{Q} n_i n_k\, a_{ji}a_{jk} / \left[\text{var}(R_j)\right]^{1/2}\left[\text{var}(R_j)\right]^{1/2} + \sigma^2$.

Sum over all j and apply Equation 34

$$\sum_{j=1}^{C} E(\Psi_j^2) = E\left(\sum_{j=1}^{C}(\Psi_j^2)\right) = C\sigma^2+\sum_{i=1}^{Q}\sum_{k=1}^{Q} n_i n_k \left(\sum_{j=1}^{C} a_{ji}a_{jk}/\left[\text{var}(R_j)\right]^{1/2}\left[\text{var}(R_j)\right]^{1/2}\right) .$$

But from Equation 37,

$$\sum_{j=1}^{C} a_{ji}a_{jk}/\mathrm{var}(R_j) = D_{ik},$$

$$\text{so } E\left(\sum_{j=1}^{C}(\Psi_j)^2\right) = C\sigma^2 + \sum_{i=1}^{Q}\sum_{k=1}^{Q} n_i n_k D_{ik} . \qquad \text{Equation 47}$$

The normal equations were $DB = A^TWAB = A^TWR = G$,

so $G_i = \sum_{k=1}^{Q} D_{ik}B_k$. Multiply both sides by B_i and sum over i

$$\sum_{i=1}^{Q} B_i G_i = \sum_{i=1}^{Q}\sum_{k=1}^{Q} D_{ik}B_i B_k .$$

Taking expectation values and applying Equations 29, 35 and 28 respectively, we get

$$E\left(\sum_{i=1}^{Q} B_i G_i\right) = \sum_{i=1}^{Q}\sum_{i=1}^{Q} D_{ik}E(B_i B_k) = \sum_{i=1}^{Q}\sum_{i=1}^{Q} D_{ik}\left[n_i n_k + \mathrm{cov}(B_i B_k)\right] .$$

Substituting from Equations 45 and 37 we have

$$E\left(\sum_{i=1}^{Q} B_i G_i\right) = \sum_{i=1}^{Q}\sum_{i=1}^{Q} D_{ik}\left[n_i n_k + \sigma^2 (D^{-1})_{ik}\right]$$

$$\text{or } E\left(\sum_{i=1}^{Q} B_i G_i\right) = \sum_{i=1}^{Q}\sum_{k=1}^{Q} D_{ik} n_i n_k + Q\sigma^2, \quad \text{since } \sum_{k=1}^{Q} D_{ik}(D^{-1})_{ik} = \sum_{k=1}^{Q} \delta_{ik} = 1.$$

Thus,

$$\sum_{i=1}^{Q}\sum_{k=1}^{Q}\eta_i\eta_k D_{ik} = E(\sum_{i=1}^{Q} B_i G_i) - Q\sigma^2 \quad . \qquad \text{Equation 48}$$

Substituting Equation 48 into Equation 47 we get

$$E(\sum_{j=1}^{C}(\Psi_j)^2) - E(\sum_{j=1}^{C} B_j G_j) = (C-Q)\sigma^2 \quad . \qquad \text{Equation 49}$$

Also, since $r = \Psi - T = \Psi - AB/\left[\text{var}(R)\right]^{1/2}$,

$$A^T r/\left[\text{var}(R)\right]^{1/2} = A^T\Psi/\left[\text{var}(R)\right]^{1/2} - A^T AB/\text{var}(R) = G - A^T AB/\text{var}(R) = 0.$$

$$\sum_{j=1}^{C} r_j^2 = r^T r = (\Psi^T - T^T)r = \Psi^T r - T^T r,\ T^T r = B^T A^T/\left[\text{var}(R)\right]^{1/2}\ r = B^T \cdot 0 = 0.$$

Therefore $\sum_{j=1}^{C} r_j^2 = \Psi^T r = \Psi^T(\Psi - AB/\left[\text{var}(r)\right]^{1/2}) = \Psi^T\Psi - G^T B$ from Equation 37,

so $\sum_{j=1}^{C} r_j^2 = \sum_{j=1}^{C}\Psi_j^2 - \sum_{j=1}^{C} B_j G_j$.

Substitute in Equation 49

$$\sigma^2 = E(\sum_{j=1}^{C} r_j^2/(C-Q)) \quad . \qquad \text{Equation 50}$$

Let $S^2 = \sum_{j=1}^{C} r_j^2/(C-Q) = \sum_{j=1}^{C} \omega_j^2 (R_j - \sum_{k=1}^{Q} a_{jk} B_k)^2/(C-Q)$, Equation 51

then $E(S^2) = \sigma^2$, and S^2 is an unbiased estimate of σ^2.

Thus $N_i = B_i \pm \sqrt{S^2 (A^T W A)^{-1}}$. Equation 52

Following the method of Beers (27, pp. 46-48) we will now show that for large N, $var(R_i) = R_i$. Let the probability that N particles are observed in time t be P_N. Then, if t is divided into d equal intervals so small that the probability of emission of two particles in the same interval is negligible, the probability of the emission of one particle in a given interval is $\bar{N}/d$ where $\bar{N}$ is the average number of particles. The probability of emission of N particles in the first N intervals and none in the remaining d-N intervals is given by $(\bar{N}/d)^N (1-\bar{N}/d)^{d-N}$. The number of ways of distributing N particles in d intervals is given by $d(d-1)...(d-N+1)$. The number of ways of interchanging the particles is N!. The probability of obtaining N counts is then given by $P_N = d(d-1)...(d-N+1)/N!(\bar{N}/d)^N (1-\bar{N}/d)^{d-N}$, the binomial distribution law. If $d \to \infty$, then $d(d-1)...(d-N+1) \to d^N$ and $(1-\bar{N}/d)^{d-N} \to e^{-N}$. Thus, $P_N = \bar{N}^N/N!$, the Poisson distribution.

Now use Stirlings approximation in the form $N! = \sqrt{2\pi}\ N^{N+1/2}\ e^{-N}$ (this approximation has an error of less than 1 percent when N>10) then $N! = \sqrt{2\pi\bar{N}}\ \bar{N}^{\bar{N}}\ e^{-\bar{N}}$, and $P_{\bar{N}} = 1/\sqrt{2\pi\bar{N}}$. Let $Y = \ln P_N$ then

$$Y = -\bar{N} + N \ln \bar{N} - \ln \sqrt{2\pi} - (N+1/2) \ln N + N \ .$$

$$\frac{dY}{dN} = \ln\bar{N}-(N+1/2)(1/N)-\ln N+1 \ .$$

When P_N is a maximum $\frac{dY}{dN} = 0$ so $\ln\bar{N}-1-1/2N-\ln N+1 = 0$ and $\ln\bar{N}-\ln e^{1/2N}-\ln N = 0$ yielding $\bar{N}-Ne^{1/2N} = 0$. Since N is postulated to be large, $e^{1/2N}$ is essentially unity, and the maximum occurs close to $N = \bar{N}$. Expand Y about $\bar{N}$ in a Taylor series and retain only the first two nonvanishing terms.

$$Y(N) = Y(\bar{N})+dY/dN(N-\bar{N})+1/2d^2Y/dN^2(N-\bar{N})^2+... \ .$$

Since the maximum occurs close to $\bar{N}$, the first derivative of Y with respect to N is zero.

$$Y(N) = -\ln\sqrt{2\pi\bar{N}} +1/2(N-\bar{N})^2d^2Y/dN^2$$

$$d^2Y/dN^2 = -1/N-1/2(-1/N^2)$$

$$\text{so} \quad Y(N) = -\ln\sqrt{2\pi\bar{N}} +1/2(N-\bar{N})^2\left[-(1/\bar{N}-1/2\bar{N}^2)\right] \ .$$

Since $\bar{N}$ is large, $1/\bar{N} >> 1/2\bar{N}^2$ and we drop the $1/2\bar{N}^2$ term. Taking antilogarithms we get

$$P_N = 1/\sqrt{2\pi\bar{N}}\ e^{-\frac{(N-\bar{N})^2}{2\bar{N}}} \ .$$

Letting $N-\bar{N} = x$, we then have

$$P_N = 1/\sqrt{2\pi\bar{N}}\ e^{-\frac{x^2}{2\bar{N}}} \ ,$$

but from Equation 5 $P(x) = 1/\sqrt{2\pi\sigma^2}\ e^{-\frac{x^2}{2\sigma^2}}$,

so if on the average $\overline{N}$ counts are observed in a time t, the standard deviation in the number of counts is $\sigma = \sqrt{\overline{N}}$. If it is assumed N is near $\overline{N}$, $\sigma = \sqrt{N}$. Thus the weights in Equations 10 and 52 are

$$\omega_i = 1/R_i \ . \qquad \text{Equation 53}$$

In practice, because of background radiation, the weights given in Equation 53 must be modified. If N_i are the true number of counts in the experimental composite spectrum, then $N_i = R_i - MBR_i$, where M is the ratio of the time for which the composite spectrum was recorded to the time for which the background was recorded, and BR_i is the number of counts recorded in the background spectrum. Then, $\Delta N_i = \Delta R_i - M\Delta BR_i$, $(\Delta N_i)^2 = (\Delta R_i)^2 + M^2(\Delta BR_i)^2 - 2M\Delta R_i \Delta BR_i$. Take the average of both sides of the equation

$$\overline{(\Delta N_i)^2} = \overline{(\Delta R_i)^2} + M^2\overline{(BR_i)^2} \ ,$$

since the ΔR_i and ΔBR_i are independent. Therefore, assuming R_i and BR_i are large,

$$(\sigma(N_i))^2 = (\sigma(R_i))^2 + M^2(\sigma(BR_i))^2 = R_i + M^2 BR_i$$

and $\omega_i = 1/(R_i + M^2 BR_i)$.

Following the method of Fry (77, pp. 285-289) we will now show that S^2 has a χ^2 distribution and can be used as a figure of merit. We had

$$P(x_1, x_2, x_3, \ldots)dx_1 dx_2 dx_3 \ldots = K\, e^{-\sum_{i=1}^{C} 1/2\frac{x_i^2}{\sigma_i^2}}\ dx_1\, dx_2 \ldots$$

where $x_i = R_i - \sum_{j=1}^{Q} a_{ij}B_j$.

But $P(x_1, x_2\ldots)dx_1dx_2\ldots = P(x_1(t_1, t_2,\ldots),x_2(t_1, t_2,\ldots)\ldots)$

$$\left|\frac{\partial(x_1, x_2,\ldots)}{\partial(t_1, t_2,\ldots)}\right| dt_1dt_2\ldots$$

$$= P(t_1, t_2,\ldots)dt_1dt_2\ldots \text{ (77, pp. 153-163).}$$

Let $q_i^2 = x_i^2/\sigma_i^2$, then

$$P(q_1, q_2,\ldots)dq_1dq_2\ldots = Ke^{-\sum_{i=1}^{C} 1/2\ q_i^2} dq_1dq_2\ldots .$$

For simplicity let $C = 3$. Also, let $q_1^2+q_2^2+q_3^2 = r^2$.

Suppose we have been given a set of the a's and have computed the sum of the squares of the q's and found it to be S^2. We want to see how reasonable the estimates of the a's are. To do this we compute the chance that another experiment, conducted so that its probabilities were really equal to the ones estimated from the experimental data, would lead to a result that is at least as improbable as the one under discussion. To do this we need to add together the probabilities of all admissible sets of values which are less likely to occur than the experimental ones. Since we have a decreasing exponential, the points which correspond to these sets all lie outside $r = S$. Hence we need only add the probabilities corresponding to all admissible

points for which r>S. In q space $q_1^2+q_2^2+q_3^2 = r^2$ is a sphere centered at the origin and with radius r. All points on it have the same probability. The q's are deviations measured in such units that equal vector deviations are equally likely, no matter what their directions. We integrate over all admissible values which lie outside a sphere of radius S. Before doing this, we must know what regions contain these admissible values. This is determined from the auxiliary equations, which will be of the form

$$\sum_{j=1}^{C} d_j q_j = 0.$$

For example, if C = 3 the auxiliary equation is $d_1q_1+d_2q_2+d_3q_3 = 0$. This is a plane passing through the origin of the coordinate system. All admissible points must lie on such a plane and the integral is no longer a volume integral outside a certain sphere but a surface integral outside a certain circle. For two such equations it will be a line which intersects two such planes. In general, a single condition on the variables reduces the space of C dimensions to one of C-1 and we must integrate over all those portions of this space which are further from the origin than a certain predetermined amount S. Q conditions reduces the space to one of C-Q dimensions. In our case the Q auxiliary equations are

$$\sum_{i=1}^{C} \frac{a_{i1}}{\sigma_i(R_i)} q_i = 0, \quad \sum_{i=1}^{C} \frac{a_{i2}}{\sigma_i(R_i)} q_i = 0, \ \ldots, \quad \sum_{i=1}^{C} \frac{a_{iQ}}{\sigma_i(R_i)} q_i = 0.$$

In one dimension

$$P = 2K \int_S^{\infty} e^{-r^2/2} \, dr.$$

In two dimensions

$$P = 2\pi K \int_S^\infty e^{-r^2/2}\, r dr.$$

In three dimensions

$$P = 4\pi K \int_S^\infty e^{-r^2/2}\, r^2 dr.$$

In c' dimensions, where c' = C-Q,

$$P_{c'}(>S^2) = K' \int_S^\infty e^{-r^2/2}\, r^{c'-1}\, dr,$$

but $1 = K' \int_0^\infty e^{-r^2/2}\, r^{c'-1}\, dr.$

Let $r^2/2 = u$, then

$$1 = K' \int_0^\infty e^{-u}\, (2u)^{\frac{c'-1}{2}} \frac{du}{\sqrt{2u}} = (2)^{\frac{c'-2}{2}} K' \int_0^\infty e^{-u} (u)^{\frac{c'-2}{2}}\, du =$$

$$(2)^{\frac{c'-2}{2}} K' \left[\Gamma\left(\frac{c'}{2}\right)\right] .$$

So $K' = 1/\left[2^{\frac{c'}{2}-1} \left(\frac{c'-2}{2}\right)!\right]$.

Then $P_{c'}(>S^2) = \dfrac{1}{2^{\frac{c'}{2}-1} \left(\frac{c'-2}{2}\right)!} \int_S^\infty e^{-r^2/2}\, r^{c'-1}\, dr$. Equation 54

Therefore, the distribution $P(\vec{r})dr$ is

$$P(r)dr = \frac{1}{\left[\frac{c'-2}{2}\right]! \; 2^{\frac{c'-2}{2}}} e^{-r^2/2} \, r^{c'-1} \, dr.$$

We want the S^2 distribution. Let $r^2 = S^2$, then $\frac{\partial r}{\partial S^2} = \frac{1}{2(S^2)^{1/2}}$

and $$P(S^2)d(S^2) = \frac{1}{\frac{c'-2}{2}! \; 2^{c'/2}} \; e^{-S^2/2} \; (S^2)^{\frac{c'-2}{2}} \; d(S^2) \; .$$

This is identical with the χ^2 distribution

$$P(\chi^2)d(\chi^2) = \frac{1}{\left(\frac{c'-2}{2}\right)! \; 2^{c'/2}} \; (\chi^2)^{\frac{c'-2}{2}} \; \exp(-\chi^2/2)d(\chi^2).$$

so $S^2 = \sum_{i=1}^{C} \left[\frac{R_i - \sum_{j=1}^{Q} a_{ij} B_j}{\sigma_i} \right]^2$ has a χ^2 distribution.

The integral in Equation 54 has been tabulated (77, p. 469). By knowing χ^2 and the number of degrees of freedom, one can determine the "goodness" of the fit. The S^2 in Equation 54 is an estimate which corrects for variances which were not included in the weighting. If the weighting factors for the least-squares solution are chosen to correspond with the true values of the variances of the R_j, then the value of σ^2 is 1 and from Equation 53 we get

$$E(\chi^2) = C-Q \text{ and } E(\chi^2)/(C-Q) = 1.$$

In summary, the squares of the standard deviations of the gamma-ray relative intensities can be determined by multiplying the diagonal elements of $(A^TWA)^{-1}$ by S^2, where S^2 is given by Equation 51. The value of S^2 can be used as a figure of merit and has an expected value of 1.

X. APPENDIX D: FLOW CHART AND REVISED COMPUTER PROGRAM

In this appendix the flow chart and listing of the IBM 360-50 computer program used to determine the gamma-ray relative intensities will be given. The program given here is a revised version of the one given in Reference 22. A maximum of 8 gamma rays recorded with a 400 channel analyzer can be analyzed at one time.

To determine the relative intensities the following equation must be solved

$$B = (A^T W A)^{-1} A^T W R.$$

This is done by reading a parameter card which specifies the number of channels and the number of gamma rays and certain other options. The program then reads the matrices A, R and the background for R. Next the weights are determined. They can be read in, set equal to 1 or calculated. During the present measurements the weights were always calculated. Two sets of background for the response functions are then read in, averaged, and subtracted from the response functions. The program will then either normalize the response functions on the photopeak area or the total area. The total area was always used in these calculations. The curve to total ratio is then determined for each response function. Following the normalization $A^T W A$ is formed, and an Ames Laboratory library subroutine MATINV is called to find $(A^T W A)^{-1}$. This inverse is then multiplied times $A^T W R$. Next, the goodness of fit parameter, S^2, defined by Equation 51 is calculated. The subroutine COMP then computes the relative intensities and standard

deviations in the relative intensities by computing the corrections and the standard deviation of the corrections. The response functions, calculated spectrum, experimental spectrum and deviation of the calculated spectrum from the experimental spectrum are then printed out. The flow chart and listings for the main program, and subroutines COMP, NLLS and SUBRT are given in Figures 45, 46, 47, 48 and 49. Subroutine NLLS is used when normalizing on the photopeak area. NLLS calls subroutine SUBRT.

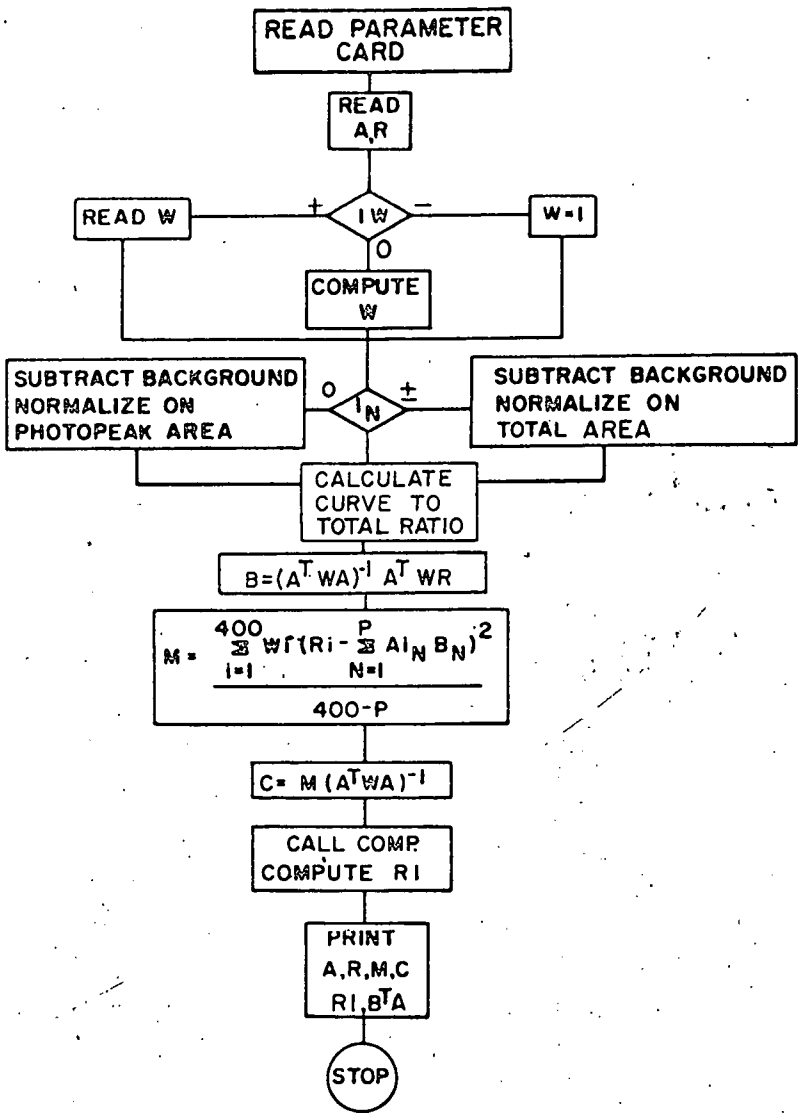

Figure 45. Flow chart of the linear least-squares computer program

```
 ISU DISK RES SPOOLED BPS FORTRAN

/JOB                  A0095 G NEL      2 MIN                                  9*
BEGIN COMPILATION
            C     RELINT                        3/18/64
            C
            C     INPUT -
            C               JA   NUMBER OF COLUMNS          (I3)
            C               IW =0, CALCULATE W (OMEGA)      (I3)
            C                  =+     READ W     (OMEGA)
            C                  =- SET W=IDENTITY MATRIX
            C               IWA=+,- WEIGHTS IN NLLS=1.0
            C                  =0  WEIGHTS IN NLLS COMPUTED
            C               INV=0, CALCULATE A(-1)*A=I AND PRINT     (I3)
            C                  =-,+  SKIP A(-1)*A =I CALCULATION
            C               IBAPR=0  PRINT BA(I), I=1,IA
            C                    =-,+ SKIP PRINT
            C                IN=+,-NORMALIZE ON TOTAL AREA
            C                  =0 NORMALIZE ON PHOTOPEAK AREA
            C               IPA=+ PRINT NORMALIZED A MATRIX
            C                  =- PRINT NORM A MATRIX AND B*NORM A MATRIX
            C                  =0 PRINT  B*NORM A MATRIX
            C
            C               TITLE  IDENTIFICATION OF DATA           (12A6)
            C
            C       CARD2  A(I,J)  A MATRIX,READ BY COLUMNS         (12E6.0)
            C       CARD3  R(I)    RHO ARRAY (DIAGONAL ELEMENTS)    (12E6.0)
            C        CARD4 R(I) BACKGROUND
            C
            C        CARD5 W(I) OMEGA VECTOR ( OPTIONAL MAY BE CALCULATED)
            C        CARD6 2 VECTORS OF BACKGROUND A VECTOR AT A TIME FOR FIRST COL
            C        CARD7 BACKGROUND FOR SECOND COLUMN OF A ETC
            C
S.0001          DIMENSION A1(400,8),A(400,8),R(400),W(400),AWA(20,20),C(20,20),
               1AWR(20),B(20),TITLE(12),AI(20,20),WORK1(20),WORK2(20),
               2WORK3(20),WORK4(20),CHOP(20),SDCHP(20),ERROR(400)
S.0002          DIMENSION BA(400),HP(400)
S.0003          DIMENSION X(250),P(20),STOP(20),B1(400),B2(400),GP2(3,20),PI(20),
               1STDE1(3,20),VARE21(20),NSIGN(8),GP(8),GP1(8),AREA(20),STDE1(20),
               2E(20),STDE(8),F(20),SDF(20)
S.0004          COMMON A1,A,R,W,AWA,C,AI,AWR,B,IA,JA,TITLE,X,P,STOP,B1,B2,GP2,PI
               1,STDE1,VARE21,NSIGN,GP,GP1,AREA,STDPI,E,STDE,IZERO,KE,KC,KN,VAL
               2,KM,ERROR
S.0005          EQUIVALENCE (BA(1),B1(1)),(HP(1),B2(1))
            C                                READ TITLE AND INDICATORS
S.0006        100 READ (1,1100)IA,JA,IW,IWA,INV,IBAPR,IN,IPA,TITLE
S.0007       1100 FORMAT (8I3,12A4)
            C
S.0008          WRITE (3,1101)TITLE
S.0009       1101 FORMAT (1H1, 9X 12A4)
            C                                END OF PROGRAM TEST
S.0010          IF (IA)300,105,601
S.0011        300 STOP 89
S.0012        105 STOP
            C                                READ IN  DATA
S.0013        601 READ (1,602) IZERO
S.0014        602 FORMAT (1I5)
S.0015        110 READ (1,1400)BRC,(AWR(J),J=1,JA)
S.0016       1400 FORMAT (5E15.8)
S.0017          DO 111 J=1,JA
S.0018        111 READ (1,1110)(A(I,J),I=1,IA)
```

Figure 46. Main program

```
S.0019          READ (1,1110)(R(I),I=1,IA)
S.0020       1110 FORMAT (4XF6.0,7XF6.0,7XF6.0,7XF6.0,7XF6.0)
S.0021          READ (1,1110)(B1(I),I=1,IA)
S.0022          IF (IW)121,125,120
S.0023        120 READ (1,1110)(W(I),I=1,IA)
S.0024            GO TO 400
                C                                   OMEGA = IDENTITY MATRIX
S.0025        121 DO 122 I=1,IA
S.0026        122 W(I)=1.
S.0027            GO TO 400
                C                                   CALCULATE OMEGA FROM RHO
S.0028        125 DO 129 I=1,IA
S.0029            ZZ=R(I)+BRC*BRC*B1(I)
S.0030            IF (ZZ)128,126,128
S.0031        126 W(I)=1.
S.0032            GO TO 129
S.0033        128 W(I)=1./ZZ
S.0034        129 CONTINUE
S.0035        400 DO 112 I=1,IA
S.0036        112 R(I)=R(I)-(BRC*B1(I))
S.0037            IF (IN)132,133,132
S.0038        132 DO 134 I=1,JA
S.0039            BZ=0.0
S.0040        604 CUT=0.0
S.0041            READ(1,1110) (B1(J),J=1,IA)
S.0042            READ(1,1110) (B2(J),J=1,IA)
S.0043            DO 137 J=1,IA
S.0044            A(J,I)=A(J,I)-.5*AWR(I)*(B1(J)+B2(J))
S.0045        137 BZ=BZ+A(J,I)
S.0046        605 IF (BZ)606,136,606
S.0047        606 CONTINUE
S.0048        607 IF (IZERO-1)608,608,610
S.0049        608 CHOP(I)=0.0
S.0050        609 SDCHP(I)=0.0
S.0051        618 GO TO 624
S.0052        610 DO 612 J=IZERO,IA
S.0053        611 CUT=CUT+A(J,I)
S.0054        612 CONTINUE
S.0055        613 CHOP(I)=CUT/BZ
S.0056        614 SDCHP(I)=CHOP(I)*SQRT(1.0/CUT+1.0/BZ)
S.0057        615 ICO=IZERO-1
S.0058        616 DO 617 J=1,ICO
S.0059        617 A(J,I)=0.0
S.0060        625 BZ=0.0
S.0061        623 DO 694 J=IZERO,IA
S.0062        694 BZ=BZ+A(J,I)
S.0063        624 CONTINUE
S.0064            IF (BZ)135,136,135
S.0065        135 DO 134 J=1,IA
S.0066            A(J,I)=A(J,I)/BZ
S.0067        134 CONTINUE
S.0068            IF (IZERO-1)130,130,619
S.0069        619 DO 620 J=1,ICO
S.0070        620 R(J)=0.0
S.0071            GO TO 130
S.0072        136 WRITE (3,1122)
S.0073       1122 FORMAT (17H DIVIDING BY BZ=0)
S.0074            STOP 89
S.0075        133 DO 138 IX=1,JA
S.0076            READ (1,1120)IL,IU,NIT,EPS,CM,(NSIGN(I),I=1,3),(GP(I),I=1,3)
S.0077       1120 FORMAT (2I4,I3,F8.5,F3.0,3I2,3F14.8)
```

Figure 46. (Continued)

```
S.0078          NDP=IU-IL+1
S.0079       401 READ (1,1110)(B1(J),J=1,IA)
S.0080          READ (1,1110)(B2(J),J=1,IA)
S.0081          DO 411 I=1,NDP
S.0082          IF (IWA)403,404,403
S.0083       403 NFDP=400+I
S.0084          A(NFDP,IX)=1.
S.0085          GO TO 411
S.0086       404 IJ=IL+I-1
S.0087          ZP=A(IJ,IX)+.25*AWR(IX)*AWR(IX)*(B1(IJ)+B2(IJ))
S.0088          NFDP=400+I
S.0089          IF (ZP)410,408,410
S.0090       408 A(NFDP,IX)=1.
S.0091          GO TO 411
S.0092       410 A(NFDP,IX)=1./ZP
S.0093       411 CONTINUE
S.0094          DO 412 I=1,IA
S.0095       412 A(I,IX)=A(I,IX)-.5*AWR(IX)*(B1(I)+B2(I))
S.0096          NP=3
S.0097          SIGMA=GP(3)/1.177410
S.0098          GP(3)=SIGMA
S.0099          DO 139 I=1,3
S.0100       139 GP1(I)=GP(I)
S.0101          DO 140 I=1,NDP
S.0102       140 X(I)=FLOAT(IL)+FLOAT(I)-1.0
S.0103          CALL NLLS(A(401,IX),X,A(IL,IX),GP1,STDE,NERR,EPS,NIT,NP,NDP,
                1VARF,VARF1,VARF2,CM,NSIGN,ISAVE)
S.0104          GO TO (141,142,143,144,145), NERR
S.0105       141 AREA(IX)=2.506628*GP1(3)*GP1(1)
S.0106          AB=0.
S.0107          DO 146 J=1,IA
S.0108       146 AB=AB+A(J,IX)
S.0109          IF (AB)154,155,154
S.0110       155 WRITE (3,1130)
S.0111      1130 FORMAT (17H DIVIDING BY AB=0)
S.0112          STOP 89
S.0113       154 IF (GP1(1))156,157,156
S.0114       157 WRITE (3,1131)
S.0115      1131 FORMAT (9H GP1(1)=0)
S.0116          STOP 89
S.0117       156 IF (GP1(3))158,159,158
S.0118       159 WRITE (3,1132)
S.0119      1132 FORMAT (9H GP1(3)=0)
S.0120          STOP 89
S.0121       158 P(IX)=AREA(IX)/AB
S.0122          STDP(IX)=(GP1(1)*GP1(3)/AB)*SQRT(6.28318*((STDE(1)/GP1(1))**2+
                1(STDE(3)/GP1(3))**2+1.0/AB))
S.0123          DO 147 J=1,3
S.0124       147 STDE1(J,IX)=STDE(J)
S.0125          IF (AREA(IX))149,150,149
S.0126       150 WRITE (3,1123)IX
S.0127      1123 FORMAT(1H ,I4,19H DIVIDING BY AREA=0)
S.0128          STOP 89
S.0129       149 DO 148 J=1,IA
S.0130       148 A(J,IX)=A(J,IX)/AREA(IX)
S.0131          GP1(3)=1.177410*GP1(3)
S.0132          DO 152 I=1,3
S.0133       152 GP2(I,IX)=GP1(I)
S.0134       138 VARF21(IX)=VARF
S.0135          IF (IPA)153,130,153
S.0136       153 WRITE (3,1124)((A(I,J),I=1,IA),J=1,JA)
```

Figure 46. (Continued)

```
S.0137     1124 FORMAT (19H A ARRAY BY COLUMNS,/(5E24.8))
S.0138          GO TO 130
S.0139      142 WRITE (3,1126)
S.0140     1126 FORMAT (16H SINGULAR MATRIX)
S.0141          STOP 89
S.0142      143 WRITE (3,1127)NIT
S.0143     1127 FORMAT (20H DID NOT CONVERGE IN,I4,11H ITERATIONS)
S.0144          STOP 89
S.0145      144 WRITE (3,1128)
S.0146     1128 FORMAT (20H XTX MATRIX SINGULAR)
S.0147          STOP 89
S.0148      145 WRITE (3,1129)ISAVE
S.0149     1129 FORMAT (19H GUESS ON PARAMETER,I2,4H BAD)
S.0150          STOP 89
                C                                  ZERO      ARRAYS
S.0151      130 DO 200 I=1,JA
S.0152          AWR(I)=0.
S.0153          DO 200 J=1,JA
S.0154      200 AWA(I,J)=0.
                C
S.0155          DO 210 I=1,JA
S.0156          DO 210 J=1,IA
                C                                    A(T)*W    = A(J,I) * W(J)
S.0157          ATW=A(J,I)*W(J)
                C                                   A(T)*W*R(I)= SUM( ATW *R(J)),J=1,IA
S.0158          AWR(I)=ATW*R(J)+AWR(I)
                C                                  A(T)*W*A(I,K)=SUM(ATW*A(J,K)),J=1,IA
S.0159          DO 210 K=1,JA
S.0160      210 AWA(I,K)=AWA(I,K)+ATW*A(J,K)
                C                                  STORE  AWR AND AWA FOR MATINV
S.0161          DO 220 I=1,JA
S.0162          B(I)=AWR(I)
S.0163          DO 220 J=1,JA
S.0164      220 C(I,J)=AWA(I,J)
                C                                  INVERT  AWA   AND  SOLVE FOR  B
S.0165      230 CALL MATINV(C,JA,B,20,1,DET,WORK1,WORK2,WORK3,WORK4)
                C                      TEST FOR  SINGULAR MATRIX
S.0166          IF (DET)240,235,240
                C                               SINGULAR MATRIX MESSAGE
S.0167      235 WRITE (3,1235)(R(I),I=1,IA)
S.0168     1235 FORMAT (45H  A(T)*W*A  IS SINGULAR. CALCULATIONS SKIPPED///12H RHS
               1 VECTOR /(1X F9.0,11F10.0))
S.0169          DO 236 J=1,JA
S.0170      236 WRITE (3,1236)J,(A(I,J),I=1,IA)
S.0171     1236 FORMAT (6H  A(I,I2,2H) ,/(6E24.8))
                C                                  NOT  SINGULAR
S.0172      240 IF (INV)260,245,260
                C                                  A(-1)*A  =I     AND  PRINT
S.0173      245 DO 255 I=1,JA
S.0174          DO 250 J=1,JA
S.0175          AI(I,J)=0.
S.0176          DO 250 K=1,JA
S.0177      250 AI(I,J)=AI(I,J)+AWA(I,K)*C(K,J)
S.0178          WRITE (3,1250)I,(AI(I,J),J=1,JA)
S.0179     1250 FORMAT (13HOIDENTITY ROW I4, 6E17.8/(7E17.8))
S.0180      255 CONTINUE
                C                                  PRINT B ARRAY
S.0181      260 WRITE (3,1260)(B(I),I=1,JA)
S.0182     1260 FORMAT (13H1 BETA VECTOR 7X  5E20.8/(20X 5E20.8))
                C
S.0183          FIAJA=IA-JA
```

Figure 46. (Continued)

```
S.0184       261 IF (FIAJA)262,561,262
S.0185       561 WRITE (3,2652)
S.0186      2652 FORMAT (8H FIAJA=0)
S.0187           STOP 89
S.0188       262 FM=0.
S.0189           DO 502 I=1,JA
S.0190           DO 502 J=1,IA
S.0191       502 A(J,I)=A(J,I)*B(I)
S.0192           IF (IPA)503,503,504
S.0193       503 DO 709 J=1,JA
S.0194       709 WRITE (3,2752)J,(A(I,J),I=1,IA)
S.0195      2752 FORMAT (5H A(1,,I3,2H )/(5E24.8))
S.0196       504 WRITE (3,2651)(R(I),I=1,IA)
S.0197      2651 FORMAT (9H R VECTOR,/(5E24.8))
S.0198           DO 275 I=1,IA
S.0199           BA(I)=0.
S.0200           DO 270 N=1,JA
S.0201       270 BA(I)=BA(I)+A(I,N)
S.0202           RBA=R(I)-BA(I)
S.0203       275 FM=FM+W(I)*RBA*RBA
S.0204           FM=FM/FIAJA
S.0205       280 WRITE (3,1280)FM
S.0206      1280 FORMAT (5H1M = E15.8//13H M*(A(I)*W*A)  10X 36HLOWER TRIANGULAR PO
                1INTED ONLY //)
             C
S.0207           DO 290 I=1,JA
S.0208           DO 285 J=1,I
S.0209       285 AWA(I,J)=FM*C(I,J)
S.0210       290 WRITE (3,1290)I,(AWA(I,J),J=1,I)
S.0211      1290 FORMAT ( 5H ROW  I2,5X 5E20.8/ (12X 5E20.8))
S.0212           IF (IN)505,506,505
S.0213       505 DO 595 J=1,JA
S.0214           P(J)=1.0
S.0215       595 STOP(J)=0.
S.0216       506 CALL COMP(B,AWA,P,STOP,RI,STDRI,E,CHOP,SDCHP)
S.0217       669 IF (IN)507,508,507
S.0218       508 WRITE (3,1135)(E(I),P(I),STOP(I),GP2(1,I),STDE1(1,I),GP2(2,I),
                1STDE1(2,I),GP2(3,I),STDE1(3,I),VARE21(I),AREA(I),I=1,JA)
S.0219      1135 FORMAT (3H E=,F6.0,6H    P=,E16.8,10H      STOP=,E16.8,10H      AMPL
                1=,E16.8,9H    STDA=,E16.8/3H X=,E15.8,5H SDX=,E15.8,5H PWR=,E15.8,
                25H SDS=,E15.8,6H VARE=,E15.8,6H AREA=,E15.8)
S.0220       507 WRITE (3,1134)(E(I),RI(I),STDRI(I),I=1,JA)
S.0221      1134 FORMAT (4H RI(,F6.0,2H)=,E16.8,7H  STRI=,E16.8)
S.0222           IF (IBAPR)630,291,630
S.0223       291 WRITE (3,1291)(BA(I),I=1,IA)
S.0224      1291 FORMAT (13HO B(N)*A(I,N)//(5E24.8))
S.0225       630 CONTINUE
S.0226       631 DO 636 I=1,IA
S.0227       632 IF (R(I))6033,634,633
S.0228      6033 R(I)=-R(I)
S.0229           ERROR(I)=(-R(I)-BA(I))/SQRT(R(I))
S.0230           GO TO 636
S.0231       634 ERROR(I)=0.0
S.0232       635 GO TO 636
S.0233       633 ERROR(I)=(R(I)-BA(I))/SQRT(R(I))
S.0234       636 CONTINUE
S.0235       637 WRITE (3,638)(ERROR(I),I=1,IA)
S.0236       638 FORMAT (26HO NEXP-NCALC OVER SQRTNEXP,/(5E24.8))
S.0237       639 CONTINUE
S.0238       640 GO TO 100
S.0239           END
```

Figure 46. (Continued)

```
 ISU DISK RES SPOOLED BPS FORTRAN

BEGIN COMPILATION
 S.0001           SUBROUTINE COMP(B,AWA,P,STDP,RI,STDRI,E,CHDP,SDCHP)
 S.0002           DIMENSION B(20),AWA(20,20),P(20),STDP(20),E(20),F(20),SDE(20),
                 1U(20,6),SDU(20,6),D(20,6),SDD(20,6),EE(20),SDEY(20),FI(20),
                 2STDRI(20),A(20),SDA(20),CORR(20,6),CHDP(20),SDCHP(20)
 S.0003           READ (1,2000)JA,N
 S.0004      2000 FORMAT (2I4)
 S.0005           READ (1,2001)(E(I),F(I),SDE(I),EE(I),SDEY(I),I=1,JA)
 S.0006      2001 FORMAT (5E15.8)
 S.0007           READ (1,2002)((U(I,J),SDU(I,J),D(I,J),SDD(I,J),I=1,JA),J=1,N)
 S.0008      2002 FORMAT (5X,4E15.8)
 S.0009           DO 401 I=1,JA
 S.0010           IF (B(I))402,500,401
 S.0011       402 WRITE (3,2003)I
 S.0012      2003 FORMAT (3H B(,I3,11H)  NEGATIVE)
 S.0013           STOP 89
 S.0014       500 WRITE (3,2100)I
 S.0015      2100 FORMAT (3H B(,I3,8H) = ZERO)
 S.0016           STOP 89
 S.0017       401 CONTINUE
 S.0018       421 DO 423 I=1,JA
 S.0019       422 F(I)=F(I)+CHDP(I)
 S.0020       423 SDF(I)=SDCHP(I)+SDF(I)
 S.0021           WRITE (3,440)
 S.0022       440 FORMAT (32HK RATIO OF CUTOFF TO TOTAL CURVE//)
 S.0023       424 WRITE (3,425)(E(I),F(I),SDF(I),I=1,JA)
 S.0024       425 FORMAT (3H E(,F6.0,2H)=,F10.8,6H  SDF=,E16.8)
 S.0025           BMAX=B(1)
 S.0026           IMAX=1
 S.0027           DO 403 I=2,JA
 S.0028           IF (BMAX-B(I))404,403,403
 S.0029       404 BMAX=B(I)
 S.0030           IMAX=I
 S.0031       403 CONTINUE
 S.0032           DMAX=0.
 S.0033           DUMAX=0.
 S.0034           DO 407 I=1,N
 S.0035           DUMAX=DUMAX+U(IMAX,I)*D(IMAX,I)
 S.0036       407 DMAX=DMAX+D(IMAX,I)*D(IMAX,I)*SDU(IMAX,I)*SDU(IMAX,I)+U(IMAX,I)*
                 1U(IMAX,I)*SDD(IMAX,I)*SDD(IMAX,I)
 S.0037           AMAX=EXP(-1.*DUMAX)
 S.0038           SDAMAX=AMAX*SQRT(DMAX)
 S.0039           BOMP=AMAX*EE(IMAX)*P(IMAX)*F(IMAX)/B(IMAX)
 S.0040           COM=AWA(IMAX,IMAX)/(B(IMAX)*B(IMAX))+SDAMAX*SDAMAX/
                 1(AMAX*AMAX)+SDEY(IMAX)*SDEY(IMAX)/(EE(IMAX)*EE(IMAX))+STDP(IMAX)*
                 2STDP(IMAX)/(P(IMAX)*P(IMAX))+SDE(IMAX)*SDE(IMAX)/(E(IMAX)*E(IMAX))
 S.0041           DO 405 I=1,JA
 S.0042           DW=0.
 S.0043           DU=0.
 S.0044           DO 406 J=1,N
 S.0045       416 CORR(I,J)=EXP(D(I,J)*U(I,J))
 S.0046           DU=DU+D(I,J)*U(I,J)
 S.0047       406 DW=DW+D(I,J)*D(I,J)*SDU(I,J)*SDU(I,J)+U(I,J)*U(I,J)*SDD(I,J)*SDD(I
                 1,J)
 S.0048           A(I)=EXP(-1.*DU)
 S.0049           SDA(I)=A(I)*SQRT(DW)
 S.0050           RI(I)=B(I)*BOMP*1000./(EE(I)*P(I)*F(I)*A(I))
 S.0051           AID=COM+AWA(I,I)/(B(I)*B(I))+SDA(I)*SDA(I)/(A(I)*A(I))+
                 1SDEY(I)*SDEY(I)/(EE(I)*EE(I))+SDE(I)*SDE(I)/(F(I)*F(I))+STDP(I)*
```

Figure 47. Subroutine COMP

```
                2STOP(I)/(P(I)*P(I))
S.0052            IF (IMAX-I)410,411,411
S.0053          411 AIDC=AID-2.*AWA(IMAX,I)/(B(IMAX)*B(I))
S.0054              GO TO 412
S.0055          410 AIDC=AID-2.*AWA(I,IMAX)/(B(IMAX)*B(I))
S.0056          412 IF (AIDC)413,405,405
S.0057          413 WRITE (3,2004)I
S.0058         2004 FORMAT ( 6H AIDC(,I4,13H) IS NEGATIVE)
S.0059              AIDC=AID
S.0060          405 STORI(I)=RI(I)*SQRT(AIDC)
S.0061              WRITE (3,441)
S.0062          441 FORMAT (1HJ )
S.0063          426 DO 427 J=1,N
S.0064          427 WRITE (3,428)(E(I),J,CORR(I,J),I=1,JA)
S.0065          428 FORMAT (10X5HCORR(F6.0,1H,I1,2H)=E16.8)
S.0066              WRITE (3,441)
S.0067              RETURN
S.0068              END
                    SIZE OF COMMON  00000     PROGRAM  05942
END OF COMPILATION  COMP
        COMPILATION TIME WAS     0002.01  SECONDS
```

Figure 47. (Continued)

```
ISU DISK RES SPOOLED BPS FORTRAN

BEGIN COMPILATION
S.0001          SUBROUTINE NLLS(W,X,Y,GP1,STDE,NERR,EPS,NIT,NP,NDP,VARE,VARE1,
               1VARE2,CM,NSIGN,ISAVE)
S.0002          DIMENSION W(250),X(250),Y(250),GP1(8),STDE(8),
               1A(8,8),B(8,1),XTX(8,8),TB(8),CONV(8),DERIV(8),C(8,8),
               2VMAT(8,8),INDEX1(8),INDEX2(8),IPIVOT(8),PIVOT(8),NSIGN(8),IGO(8)
S.0003          NERR=1
S.0004          DO 1003 I=1,NP
S.0005          IF (GP1(I))1001,1002,1002
S.0006     1001 IGO(I)=1
S.0007          GO TO 1003
S.0008     1002 IGO(I)=2
S.0009     1003 CONTINUE
S.0010          DO 118 N=1,NIT
S.0011          DO 110 L=1,NP
S.0012          B(L,1)=0.0
S.0013          DO 110 M=1,NP
S.0014      110 A(L,M)=0.0
S.0015          DO 111 J=1,NDP
S.0016          CALL SUBRT(J,W,X,Y,GP1,DERIV,YC,F1,WI)
S.0017       50 DO 111 L=1,NP
S.0018          B(L,1)=B(L,1)+DERIV(L)*F1*WI
S.0019          DO 111 M=L,NP
S.0020      111 A(L,M)=A(L,M)+DERIV(L)*DERIV(M)*WI
S.0021          DO 112 M=2,NP
S.0022          K=M-1
S.0023          DO 112 I=1,K
S.0024      112 A(M,I)=A(I,M)
S.0025          DO 212 L=1,NP
S.0026          DO 212 M=1,NP
S.0027      212 XTX(L,M)=A(L,M)
S.0028          CALL MATINV(A,NP,B,8,1,DET,INDEX1,INDEX2,IPIVOT,PIVOT)
S.0029          IF (ABS(DET)-1.0E-30)113,113,114
S.0030      113 NERR=2
S.0031          GO TO 200
S.0032      114 DO 115 I=1,NP
S.0033          KUT=0
S.0034     1008 TB(I)=GP1(I)+CM*B(I,1)
S.0035          IF (NSIGN(I))1004,115,1004
S.0036     1004 ICHG=IGO(I)
S.0037          GO TO (1005,1006), ICHG
S.0038     1005 IF (TB(I))115,1007,1007
S.0039     1006 IF (TB(I))1007,1007,115
S.0040     1007 B(I,1)=B(I,1)/2.0
S.0041          KUT=KUT+1
S.0042          IF (KUT-7)1008,1008,1009
S.0043      115 CONTINUE
S.0044          GO TO 1010
S.0045     1009 ISAVE=I
S.0046          NERR=5
S.0047          GO TO 200
S.0048     1010 DO 116 I=1,NP
S.0049          CONV(I)=ABS(GP1(I)/TB(I)-1.0)
S.0050          IF (CONV(I)-EPS)116,116,117
S.0051      116 CONTINUE
S.0052          GO TO 120
S.0053      117 DO 118 I=1,NP
S.0054      118 GP1(I)=TB(I)
S.0055          NERR=3
```

Figure 48. Subroutine NLLS

```
S.0056            GO TO 200
S.0057         120 DO 121 I=1,NP
S.0058         121 GP1(I)=TB(I)
S.0059            SUMW=0.0
S.0060            VARF2=0.0
S.0061            DO 122 J=1,NDP
S.0062            CALL SUBRT(J,W,X,Y,GP1,DERIV,YC,F1,WI)
S.0063            VARF2=VARF2+WI*F1*F1
S.0064         122 SUMW=SUMW+WI
S.0065            VARF=VARF2/(FLOAT(NDP)-FLOAT(NP))
S.0066            VARF1=VARF/SUMW
S.0067            DO 125 I=1,NP
S.0068            DO 125 J=1,NP
S.0069            IF (I-J)124,123,124
S.0070         123 C(I,J)=1.0
S.0071            GO TO 125
S.0072         124 C(I,J)=0.0
S.0073         125 CONTINUE
S.0074            CALL MATINV(XTX,NP,C,8,NP,DET,INDEX1,INDEX2,IPIVOT,PIVOT)
S.0075            IF (ABS(DET)-1.0E-30)126,126,127
S.0076         126 NERR=4
S.0077            GO TO 200
S.0078         127 DO 128 I=1,NP
S.0079            DO 128 J=1,NP
S.0080         128 VMAT(I,J)=C(I,J)*VARF
S.0081            DO 129 I=1,NP
S.0082         129 STDE(I)=SQRT(VMAT(I,I))
S.0083         200 RETURN
S.0084            END
                    SIZE OF COMMON  00000     PROGRAM  14580
END OF COMPILATION  NLLS
        COMPILATION TIME WAS    0001.81  SECONDS
```

Figure 48. (Continued)

```
 ISU DISK RES SPOOLED BPS FORTRAN

BEGIN COMPILATION
 S.0001           SUBROUTINE SUBRT(J,W,X,Y,GP1,DERIV,YC,F1,WI)
 S.0002           DIMENSION W(250),X(250),Y(250),GP1(8),DERIV(8)
 S.0003           YC=GP1(1)*EXP(-.5*((X(J)-GP1(2))/GP1(3))**2)
 S.0004           F1=Y(J)-YC
 S.0005           DERIV(1)=EXP(-.5*((X(J)-GP1(2))/GP1(3))**2)
 S.0006           DERIV(2)=(GP1(1)*(X(J)-GP1(2))/(GP1(3))**2)*DERIV(1)
 S.0007           DERIV(3)=(X(J)-GP1(2))/GP1(3)*DERIV(2)
 S.0008           WI=W(J)
 S.0009           RETURN
 S.0010           END
                     SIZE OF COMMON  00000     PROGRAM  00682
END OF COMPILATION  SUBRT
        COMPILATION TIME WAS     0000.86  SECONDS
```

Figure 49. Subroutine SUBRT